12-3-2020

Parametric Model Development For Heterogeneous Atmospheric Conditions

Daniel Paul Greenway
Coastal Carolina University

PARAMETRIC MODEL DEVELOPMENT FOR HETEROGENEOUS ATMOSPHERIC CONDITIONS

By

Daniel Paul Greenway

Submitted in Partial Fulfilment of the Requirements for the Degree of Master of Science in Coastal Marine and Wetland Studies in the Department of Marine Science School of the Coastal Environment

Coastal Carolina University

2020

Dr. Erin E. Hackett	Dr. Roi Gurka
Major Professor	Committee Member
Dr. Shaowu Bao	
Committee Member	
Dr. Richard Viso	Dr. Michael Roberts
CMWS Coordinator	Dean

Dedication

This work is dedicated to my family, without whom I wouldn't have patience;

To my teachers, who taught me how to think analytically and critically;

To my fellow students who struggle beside me.

And also to my music instructors who taught me how to create and improvise even in the face of adversity.

This work could not have been completed without you.

Thank you.

Acknowledgements

First and foremost, I want to thank my major advisor Dr. Erin Hackett for spending countless hours supporting me and pushing me to become a better scientist. Without your help and guidance, it is likely I would have wandered off-trail and lost my path. I'm forever grateful for all the energy you have put into helping me succeed and look forward continuing to make scientific discoveries with you. I would also like to thank my committee members Dr. Roi Gurka and Dr. Shaowu Bao, for giving me different perspectives and advice through the scientific process. I would like to thank Tracy Haack from the Naval Research Laboratory for her continued collaboration and providing the COAMPS®-NAVSLaM blended data used for this study. I would also like to thank Dr. Qing Wang from the Naval Postgraduate School for the *in-situ* data supplied for this study from the CASPER-East field campaign. This project would not have been possible without funding through the Office of Naval Research (grants: N00014-16-1-2075, N00014-19-1-2350), and Coastal Carolina University.

I would like to acknowledge all of the members of the Environmental Fluids Lab for their continuous support, discussion, and advice. More specifically, I would like to thank Douglas Pastore, Matt Stanek, and Sarah Wessinger for listening to me when I needed to ramble, and for helping me clarify my thoughts when they were cloudy. Other than the EFL, I have received help from many other graduate students and peers. Thank you to Christina Boyce, James Foster, Charlotte Kollman, Matthew Rodriguez, Elana Ames, Madison Fink, Todd Rhodes, and all of the other students and staff who have helped me progress my education through discussion and, more importantly, friendship. I will always be grateful.

Abstract

This study investigates range variations of refractive environments to develop a parametric model for heterogeneous refractive conditions for use in inversion methods. A blended data source that combines numerical weather prediction data (COAMPS®) and a semi-empirical model based on boundary layer similarity theory (NAVSLaM) that contains hourly forecasts over a 1-month period from October to November is used. A novel 11-parameter heterogeneous refractive gradient model (HRGM) is developed that can be integrated to produce estimations of modified refractivity with respect to range from which propagation pattern predictions can be simulated. Both modified refractivity and propagation loss (PL) patterns based-on the HRGM are evaluated and compared to that of the blended data set. On average, the HRGM is able to accurately estimate refractivity and PL in horizontally heterogeneous refractive environments. Although biases are small, the HRGM exhibits typical underestimation of modified refractivity beneath the duct height, and overestimation above the duct height. PL discrepancies due to the HRGM occur in the multipath nulls and above typical duct heights in the long range region, but often the latter are relatively small discrepancies. The leading cause of error in the propagation predictions associated with the HRGM over the entire domain are related to inaccuracies in the model's prediction of duct heights with respect to range, but these PL errors are mostly constrained to regions near the multipath nulls. The PL discrepancies in the long range (<45 km) are related to inaccuracies of the model's prediction of refractive gradients above the surface. Although containing few discrepancies, the HRGM presented in this study provides a novel parametric model that can be used to solve radar inversion problems in horizontally heterogeneous refractive environments.

Table of Contents

List of Figures

List of Tables

List of Symbols and Abbreviations

a:	Amplitude of $\frac{dM}{dz}$ variation from the mean
a_1:	Amplitude of surface $\frac{dM}{dz}$ at wavenumber of 0.0158 km^{-1}
a_2:	Amplitude of surface $\frac{dM}{dz}$ at wavenumber of 0.0316 km^{-1}
a_3:	Amplitude of surface $\frac{dM}{dz}$ with wavenumber of 0.0474 km^{-1}
C_{xy}:	Correlation coefficient between generic variable *x* and generic variable *y* with respect to range
C_{Ri}:	Correlation coefficient between gradient Richardson number ($\overline{Ri}(r)$) and duct heights as a function of range
CASPER:	Coupled Air-Sea Processes and Electromagnetic Ducting Research
COAMPS®:	Coupled Ocean-Atmosphere Mesoscale Prediction System
COARE:	Coupled Ocean-Atmosphere Response Experiment
c_0:	Potential refractivity gradient or duct curvature
c:	Velocity of an EM wave in a vacuum
D:	Percent difference
$\frac{dM}{dz}\Big\vert_{z=0}$:	$\frac{dM}{dz}$ between z = 0 m and z = 0.1 m
$\frac{dM}{dz}$:	Modified refractivity gradient

$\left.\frac{dM}{dz}\right|_{z = z_d - dz}$: $\frac{dM}{dz}$ at z-Δz

$\frac{dN}{dz}$: Atmospheric refractive gradient

$\overline{\frac{dM}{dz}}$: Mean $\frac{dM}{dz}$ over range at z_{max}

E: Percent error (in decimal)

$\boldsymbol{E}$: Electric field in non-vacuum environment

$\boldsymbol{E_0}$: Electric field in free space

EM: Electromagnetic

FFT: Fast-Fourier Transform

g: Gravitational acceleration

HRGM: Heterogeneous refractive gradient model

k_o: Wavenumber of an electromagnetic wave

$k_{\overline{\frac{dM}{dz}}}$: Wavenumber of $\frac{dM}{dz}$ variations

e_p: Partial pressure of water vapor

GPS: Global positioning system

i: Index variable for range

j: Index variable for altitude

M: Modified refractivity

$\widehat{M}$: Modified refractivity estimated using the parametric model

M_0: Surface modified refractivity

M_1: Continuity term

M_t: Modified refractivity at the top of the trapping layer

MABL: Marine atmospheric boundary layer

MO: Monin-Obhukov

MCMC: Markov chain Monte Carlo

MURI: Multi-university research initiative

m_1: Mixed layer slope

N: Atmospheric refractivity

NAVSLaM: Navy Atmospheric Vertical Surface Layer Model

NC: North Carolina

NRL: Naval Research Laboratory

NOGAPS: Naval Operational Global Atmospheric Prediction System

NWP: Numerical weather prediction

n: Index of refraction

n_M: Number of modified refractivity measurements in height and range

n_{x_r}: Number of data points in range

n_{x_z}: Number of data points in altitude

n_{PL}: Number of propagation loss data points in height and range

ONR: Office of Naval Research

P_f: Propagation factor

P_L: Propagation loss

$\widehat{P_L}$: Propagation loss estimated using modified refractivity estimated using the parametric model

PL: Propagation loss

PSD: Power spectral density

p: Atmospheric pressure

R_e: Radius of the earth

R/V: Research vessel

RMSE: Root mean square error

Ri: Gradient Richardson number

$\overline{Ri}$: Altitude and range-averaged gradient Richardson number

$\overline{Ri}(r)$: Altitude-averaged gradient Richardson number

r: Range

r_{max}: Range at which z_{max} occurs

S: Power spectral density

SST: Sea surface temperature

T: Temperature

T_v: Average virtual temperature

U: Eastern wind component

V: Northern wind component

VTRPE: Variable Terrain Radiowave Parabolic Equation simulation

v: Velocity of an EM wave through a medium

w: Mixing ratio

x: General variable analyzed with respect to range

$\bar{x}$: Mean of general variable analyzed with respect to range

$\hat{x}$: Estimated general variable using least squares regression

x_f: Fourier coefficient

z: Altitude

z_d: Evaporation duct height

z_{d_0}: Duct height at r = 0 km

z_l: Evaporation layer

z_{max}: Altitude of maximum difference between $\frac{dM}{dz}$ and $\overline{\frac{dM}{dz}}$

1D: One-dimensional

$\alpha_{\frac{dM}{dZ}\big|_{z=0}}$: RMSE of surface refractivity gradient with respect to range

$\alpha_{\frac{dM}{dz}\big|_{z<z_d}}$: RMSE of refractive gradient with respect to range below the duct height

$\alpha_{\frac{dM}{dz}\big|_{z>z_d}}$: RMSE of refractivity gradient with respect to range above duct height

α_x: RMSE of a general variable

α_{z_d}: RMSE of duct height with respect to range

α_M: RMSE of M

α_{PL}: RMSE of P_L

β_M: Residual of M

β_{PL}: Residual of P_L

Δr: Range sampling interval

Δz: Altitude sampling interval

μ_x: Mean of a generic variable over range and/or altitude

$\mu_{\frac{dM}{dZ}}$: Mean of surface $\frac{dM}{dz}$

θ_v: Virtual potential temperature

κ_1: Decay rate of $\frac{dM}{dz}$ with respect to height below z_d

κ_2: Decay rate of $\frac{dM}{dz}$ with respect to height above z_d

σ_{Ri}: Standard deviation of $\overline{Ri}(r)$

σ_x: Standard deviation of general variable

φ: Initial phase of $\frac{dM}{dz}$

ξ: Rate of duct height change in range

1.0 Introduction

Many communication systems and remote sensing technologies rely on the transmittance and retrieval of electromagnetic (EM) waves to detect and send information through the earth's environment. Common devices that utilize EM waves to operate include radios, cell phones, wireless internet, Bluetooth devices, televisions, and weather radar. The EM waves emitted from devices such as these are affected by the medium in which they propagate. Thus, the performance of these systems is affected by the environment in which they operate. This study investigates the influence of the environment on the behavior of EM waves used by radar detection systems.

Radio detection and ranging, or radar, is a detection system that emits EM waves to sense a wide variety of targets over large distances. Radar is used in remote sensing capacities in fields of atmospheric and oceanic science to detect and track atmospheric aerosols such as clouds and smoke, rain, or sea surface features such as waves. This tracking enables improved weather and other environmental predictions. Radar is also used in engineering applications such as by air-traffic control stations to detect aircraft, and aboard military aircraft and vessels to surveil the air and sea.

Radar aboard ships, or from other offshore vehicles and platforms, operate in the marine-atmosphere boundary layer (MABL), which is a complex environment that involves significant transport of mass and momentum including air-sea exchange. The

MABL and sea surface affect radar system performance due to processes such as forward scattering, reflection, attenuation, and refraction. This study focuses on the effects of refraction, more specifically ducting, which is a special case of refraction. Ducting causes EM waves traveling through the MABL to bend towards the surface, often trapping the waves near the surface (Skolnik, 1990). The trapping of EM waves can result in holes in radar detection as well as extending detection ranges – both of which can contribute to positioning uncertainties.

Direct atmospheric measurements of ducting environments are difficult because it requires instantaneous, fine-scale measurements of atmospheric properties over large spatial areas in both height and range. Routine direct measurements are both impractical and expensive; requiring radiosondes, ships, aircraft, and many personnel to produce an accurate representation of the atmosphere, if ever possible. As such, numerical methods exist to predict atmospheric environments using numerical weather prediction models (NWP) or theoretical models such as Monin-Obukhov similarity theory (MO theory). However, these methods are often too low resolution to resolve ducting environments, make too many assumptions, and require direct atmospheric measurements for initial conditions (Karimian et al. 2013).

Another approach to evaluate the environment is to inversely determine the atmospheric conditions using radar measurements (Karimian et al. 2011). Unlike atmospheric measurements, radar measurements are more practical to be made *in-situ* because they are a remote sensor. Many studies have investigated inverse approaches of predicting atmospheric ducting conditions using radar wave propagation (Karimian et al. 2011; Yardim et. al., 2009; Yardim et. al., 2006; Gerstoft et. al. 2006; Penton and Hackett,

2018; Matsko and Hackett, 2019). However, many of these studies have assumed a horizontally homogeneous atmosphere. The validity of this homogeneity assumption is questionable, especially in areas with rapidly changing temperature, moisture, or pressure such as those seen in coastal zones. This study aims to improve these inversion methods by exploring how heterogeneous environments can be taken into account. In particular, this study examines NWP forecasts, theoretical estimates, and atmospheric measurements to assess the importance and significance of horizontal inhomogeneity. This information is used to develop a parametric model that may incorporate inhomogeneity into these inversion approaches.

In the next section, background information on electromagnetic wave propagation in marine environments, atmospheric refractivity, types of ducts and their meteorological causes, heterogeneous environments, along with previous and current modeling of evaporation ducts for inversion studies are discussed. The third section discusses the research objective. The fourth section discusses the methods that are applied in this study including data sources, EM propagation modeling, methods for characterizing variations of refractive attributes (modified refractivity, duct height, and refractivity gradients) over range, and methods for evaluating the range-dependent parametric model developed in this study. The fifth section contains the results including the characterization of range dependent variations of modified refractivity, duct height, and refractive gradients; a proposed parametric model; and evaluation of the proposed parametric model. The final section contains a summary and the conclusions of this study.

2.0 Background

2.1 Electromagnetic Wave Propagation in Marine Environments

Communication systems and remote sensing technologies rely on the propagation of EM waves in Earth's environment. EM waves are a result of oscillations between an electric field and a magnetic field, and propagate at the speed of light through a vacuum. Characterized by their frequency of oscillation as they propagate, or by their wavelength, EM waves are divided into distinct categories as shown in Table 1 (Knight, 2013). Radar systems are one of the remote sensing technologies that rely on EM waves, more specifically microwaves (Table 1), to perform measurements.

Radar systems are either monostatic or bistatic. Monostatic radar systems use an antenna to transmit microwaves, which propagate in the environment until they reach a target (water droplets, planes, trees, etc.). Some microwaves reflect and scatter back towards the antenna, which receives these reflected/scattered EM waves from the target, forcing the antenna to switch between transmitting and receiving EM waves on the scales of microseconds. Many studies have investigated propagation effects using monostatic radar and use the measurements to invert for the refractive environment (Karimian et. al., 2011; Yardim et. al., 2009; Yardim et. al., 2006; Gerstoft et al., 2003; Rogers et al., 2000). These studies have primarily examined sea clutter, which are EM waves that are reflected and scattered from the sea surface, to estimate the environment. In contrast, a bi-static system has separate transmitting and receiving sites, allowing large distances between the

transmitting and receiving units; an object/target to reflect or scatter EM waves is not needed. Bi-static systems have also been used to estimate the environment (Gerstoft et al., 2000; Zhao, 2012; Wagner et al., 2016; Penton and Hackett, 2018; Matsko and Hackett, 2019) with the advantage of not needing an accurate means of estimating the reflection and scattering off of an object.

Earth's environment affects microwave propagation through processes such as forward scattering, reflection, attenuation, and refraction. Forward scattering occurs when microwaves propagate into particles or surfaces, and primarily occur in interaction with the rough ocean surface. Reflection resulting in multipath occurs when microwaves are reflected from Earth's surface and cause interference patterns between EM waves on reflected and direct paths. Attenuation, which is caused by absorption of energy by gas molecules in the air, also occurs and leads to a reduction in intensity of the microwaves as they traverse the atmosphere. Lastly, refraction, which is caused by variation in the composition of the atmosphere's medium, causes changes in microwaves' direction of propagation. Refraction can affect radar systems by altering the maximum range of the radar or by creating "holes" in the coverage (Skolnik, 1990).

Bi-static radar systems often operate in the MABL. Garrat (1992) defines an atmospheric boundary layer as "the layer of air directly above the earth's surface in which the effects of a surface are felt directly on time scales less than a day." In the MABL, the surface is the unsteady ocean surface, at which significant turbulent transport and exchange of heat, mass, and momentum between the air and the sea occur. The aforementioned interactions are complex and make studying this environment difficult; however, knowing how this environment affects the propagation of microwaves is important for understanding

radar system performance. For X-band microwave propagation, the largest environmental effects are refraction and multipath (Skolnik, 1990).

2.2 Atmospheric Refractivity

Refraction is the deviation of the direction of wave propagation caused by variations in the medium where the wave propagates. The refractive properties of a medium are characterized by the index of refraction, which is the ratio between the velocity of an EM wave in a vacuum (c) and the velocity in the medium (v) in question:

$$n = \frac{c}{v} \quad \textbf{(1)}$$

Free space (or a vacuum) has $n = 1$, while all other materials have $n > 1$. For air, atmospheric refractivity (N) is used instead of the index of refraction because n of air is only slightly greater than one. A relationship, derived by Bean and Dutton (1968), relates N to temperature in Kelvin (T), barometric pressure in millibars (p), and partial pressure of water vapor in millibars (e_p):

$$N = (n - 1) \times 10^6 = \frac{77.6}{T} p + \frac{373256 e_p}{T^2} \quad \textbf{(2)}$$

refractivity is unitless, but will be referred to as N-units for clarity.

Normal refractive environments occur when the refractive gradient with respect to height ($\frac{dN}{dz}$) is between 0 and -79 N-units/km. Subrefractive environments occur when $\frac{dN}{dz} > 0$. An increasing gradient can cause the maximum detection range of a radar system to be reduced because the propagation path bends away from Earth's surface. Lastly, super refractive environments occur when $\frac{dN}{dz} <$ -79 N-units/km. Super-refraction causes the

propagation path to potentially follow the curvature of the earth which, in turn, can increase the detection range beyond the radar horizon (Skolnik, 1990).

Ducting, a sub-category of super refraction, causes the propagation path of microwaves to bend toward the earth's surface. More specifically, ducting occurs when $\frac{dN}{dz}$ < -157 N-units/m. If $\frac{dN}{dz}$ = -157 N-units/m, then the propagation follows the curvature of the earth, while lower values cause EM waves to bend directly towards the surface. In order to account for the curvature of the earth and easily identify ducting conditions, modified refractivity is defined:

$$M = N + \left(\frac{z}{R_e}\right) \times 10^6 \quad \textbf{(3)}$$

where R_e is the radius of the earth and z is altitude. Ducting conditions are identified as $\frac{dM}{dz}$ < 0 and the duct height is the altitude where $\frac{dM}{dz}$ = 0. Similar to *N*, modified refractivity is unitless, but will be referred to as M-units for clarity. Being a subcategory of super refraction, ducting increases the range of detection beyond the radar horizon. However, in many situations ducting scenarios cause the microwaves to be trapped near the earth leaving "holes" in the radar coverage at higher altitudes (Skolnik, 1990). A lack of awareness of these enhanced/reduced detection ranges can lead to positioning errors.

2.3 Types of Ducts

Three distinct types of ducts affect microwave propagation: surface ducts, elevated ducts, and combination ducts. Each type of duct can be classified based on modified refractivity (*M*) at the surface (M_0), and *M* at the top of the trapping layer (M_t). The trapping layer is a range of altitudes identified by decreasing modified refractivity with height ($\frac{dM}{dz}$

< 0). Surface ducts are classified by $M_0 > M_t$, elevated ducts are classified by $M_0 < M_t$, and combination ducts are those in which both elevated and surface ducts exist simultaneously. All types of ducts are exemplified in Figure 1. Ducts are typically formed by temperature inversions and evaporative processes that take place within the trapping regions of each type of duct illustrated in Figure 1 (Skolnik, 1990; see section 2.4).

Three types of surface ducts are known to exist: surface-based, elevated, and evaporation ducts. Surface based ducts, are surface ducts whose trapping layer begins at the surface, whereas elevated surface ducts are surface ducts whose trapping layer begins above the surface. Both elevated and surface based surface ducts are temperature driven. Evaporation ducts, however, are surface based ducts that are humidity driven, and categorized by a rapid decrease in humidity with height (Skolnik, 1990). Examples of each type of surface duct are shown in Figure 2.

2.4 Meteorological Causes of Ducting

Temperature inversions and evaporative processes create ducting scenarios. A temperature inversion is an increase in temperature with altitude, as opposed to the typical atmospheric conditions where temperature decreases with altitude. Common causes of temperature inversions include radiative effects, flow advective conditions, diverging downdrafts of air, and large-scale subsidence (Markowski and Richardson, 2010).

An example of a temperature inversion caused by radiative effects is observed on clear nights. During nighttime hours the ground is cooled as earth releases more longwave radiation into the atmosphere than shortwave solar radiation is received. The cool air just above the ground results in the air above the surface being warmer than the air close to the surface, thus producing a temperature inversion.

Temperature inversions also occur due to flow advection. Advection of temperature refers to a change in temperature caused by movement of air, or wind. Sea/land breezes and fronts are examples of processes caused by flow advection that can lead to temperature inversions. Sea/land breezes are caused by temperature contrasts, which develop due to the differences of heat capacity between land and water, and are frequently present in coastal environments. During the day, more heating takes place on land due to its lower heat capacity. The heating generated over the land creates a thermal circulation cell that advects the cooler air from the water onto land. The product of this circulation is known as a sea breeze. The sea breeze's counterpart, the land breeze, is caused by a nighttime cooling of the land, which generates a similar thermal circulation that advects the cooler air from the land under the warmer, less dense air over the water. Land breezes generate temperature inversions in areas over the water, while sea breezes generate temperature inversions in areas over the land. Synoptic fronts such as cold fronts, warm fronts, and occluded fronts also bring in conditions where temperature inversions are favorable. Fronts are boundaries, which separate two masses of air of different densities. Cold fronts are boundaries where cold air is approaching warm air, and warm fronts are boundaries where warm air is approaching cold air. As either of these frontal systems move through, temperature inversions are likely to ensue as warm air aloft quickly advances over the cold dense air at the surface. Also, diverging downdrafts of air underneath thunderstorms produce temperature inversions because of the cold air that spreads out from the thunderstorm's base (Skolnik 1990).

Another frequent cause of temperature inversions is large-scale subsidence that meets low-level maritime air. The general sinking of air causes compression, which results

in adiabatic heating and a decrease in moisture content. This process leads to warmer, drier air lying above cooler, moist air and produces a temperature inversion. More often than not, large-scale subsidence occurs in the trade wind regions, and while these effects can produce surface ducts, they typically also cause elevated ducts along the marine boundary layer (Skolnik, 1990).

Evaporation over bodies of water can also lead to surface duct formation. Evaporation is a process of vaporization where liquid water is transformed to a gaseous state. As evaporation takes place at the surface of a body of water, the air in contact with the sea surface is saturated with water vapor but as height above the surface increases the amount of water content decreases. The decrease in partial vapor pressure, e_p (Equation 2), causes a steep decrease in the modified refractivity near the surface. Evaporation ducts are the most common type of surface duct in marine environments (Babin, 1996; Babin et al., 1997) and are a nearly permanent worldwide feature in oceanic regions (Skolnik, 1990).

2.5 Horizontally Heterogeneous Refractivity Environments

Although variations in refractivity with height are known to be much more significant than variations in horizontal directions, prior research has shown that horizontal variations can also cause significant effects on propagation (Bean and Cahoon, 1959; Goldhirsh and Dockery, 1998; Brooks et. al., 1999). Currently, most studies assume a horizontally homogeneous refractivity environment, where a single profile of refractivity with respect to height is assumed to be consistent throughout an entire horizontal domain. However, refractive environments and duct heights can change in the horizontal directions due to horizontal variations of T, e_p, and p, which commonly occur at air/mass boundaries associated with cyclones, land/ocean interfaces, coastal zones, sea surface temperature

gradients, clouds, thunderstorm anvil shadows, and heavy rainfall (Markowski and Richardson, 2010). Figure 3 illustrates examples of a homogeneous refractivity environment (Figure 3a) and a heterogeneous refractive environment (Figure 3b).

A study by Bean and Cahoon (1959) suggests that 1km above the surface, horizontal changes appear to have little effect on the propagation; however, they show that microwaves emitted at low elevation angles are sensitive to extreme horizontal variations of atmospheric conditions near the surface. Goldhirsh and Dockery (1998) demonstrate that while the homogeneity assumption gives miniscule errors at small scales and ranges, errors at long ranges (>30 km) are significantly larger. Brooks et al. (1999) shows that large differences in radar wave propagation behavior are found when comparing environments which assume homogeneous refractivity with *in-situ* measured propagation, indicating that a heterogeneous environment may be necessary to accurately assess these environments. Also, variations associated with the physical processes previously described have also been shown to affect radar wave propagation such as sea breeze/land breeze circulations (Atkinson and Li, 2000), as well as land/ocean interfaces (Brooks, 2001).

2.6 Modeling Evaporation Ducts

Currently, three primary methods are used for estimating an evaporative ducting environment. First, similarity functions, i.e., MO boundary layer similarity theory, can be used to predict evaporation ducts using bulk environmental methods (Foken, 2006). MO theory has several shortcomings, and can result in inaccurate predictions in unstable environments such as those with high ocean surface wave energy, or heterogeneous environments of T, e_p, or p (Hill, 1989). Second, numerical weather prediction models such as COAMPS® can be used to estimate evaporative ducting conditions (Hodur, 1997).

NWP models simulate environmental conditions by using atmospheric or oceanic measurements as initial boundary conditions, and applying these conditions to solve the unsteady Navier-Stokes partial differential equations. While NWP models produce consistent, easy to work with output for analysis, a shortcoming of NWP models is that the spatial resolution is coarse especially in the vertical direction, with the finer resolution models approaching 4 kilometer horizontal resolution, and ~15 m vertical resolution, making small scale processes difficult to replicate (Yano, 2018). Last, to overcome the limitations of the above approaches and provide a secondary option when direct measurements of the atmosphere are not feasible, inversion methods of estimating the environment are continuously evolving (Karimian et. al., 2011). Inversion methods use *in-situ* radar measurements along with radar wave propagation models, and machine learning techniques to inversely predict refractivity. Inversion methods are particularly attractive because *in-situ* acquisition of radar data is relatively simple and radar waves cover large areas but are affected by processes down to the wavelength of the radar wave (order centimeters for X-band). However, in order to ensure the existence of unique repeatable accurate solutions from inversion methods, the refractivity must be described using a limited set of parameters and the inversion must use an appropriate amount of radar data (Saeger et al., 2015; Matsko and Hackett, 2019). Inversion methods typically estimate parameters of parametric refractivity models that are then used to generate refractivity vertical profiles. Thus, inversion methods are limited by the parametric refractivity model used to characterize refractivity in evaporative ducting environments.

Many parametric models have been developed to parameterize modified refractivity profiles in evaporative ducting conditions, namely the Paulus-Jeske

evaporation duct model (Paulus 1985, 1990) and the Stacked model (Gerstoft et al. 2003). Saeger et al. (2015) compares the performance of these models, and shows that the best log linear model formulation for an inversion problem is a two-layer stacked model that contains at least three parameters: duct height, duct curvature, and a mixed layer slope. Penton and Hackett (2018) use such a model:

$$M(z) = M_0 + \begin{cases} c_0\left(z - z_d \ln\left(\frac{z + 0.00015}{0.00015}\right)\right), & z \le z_l \\ m_1 z - M_1 \quad , & z > z_l \end{cases} \qquad \textbf{(4)}$$

where z_d is evaporation duct height, m_1 is mixed layer slope, c_0 is the potential refractivity gradient (or duct curvature), z_l is the evaporation layer which is defined as $2z_d$, and M_1 ensures continuity between the two layers (i.e., this is not a free parameter but a function of the other parameters). Figure 4 illustrates an example modified refractivity profile described by Equation 4. In most inversion approaches, a single refractivity profile is assumed to be homogeneous in range. However, many studies have also shown that true environments are rarely homogeneous (Bean and Cahoon, 1959; Goldhirsh and Dockery, 1998; Brooks et. al., 1999; Atkinson and Li, 2000; Brooks, 2001) implying that parametric models used to solve inversion problems should parameterize heterogeneous environments. Gerstoft et. al. (2003) attempts to model a heterogeneous refractivity environment using five parameters for the vertical structure, and six parameters for the horizontal structure, and found that the parameters were able to model the environment well within the trapping layer of the duct, but not above the trapping layer. Other approaches to inversely determine heterogeneous refractivity environments have included using Markov chain Monte Carlo (MCMC) sampling approaches (Yardim et al. 2006) and,

more recently, the use of adjoint methods (Zhao et. al. 2011; Zhao and Huang, 2012, 2014; Zhao et al., 2017).

Table 1. Different categories of electromagnetic waves and their associated frequency range and wavelengths.

Name	Frequency (Hz)	Wavelength (m)
AM Radio	$10^6 – 10^8$	3-300
FM Radio/ TV	$10^8 – 10^{10}$	0.03-3
Microwaves	$10^{10} – 10^{12}$	$3 \times 10^{-4} – 0.03$
Infrared	$10^{12} – 10^{14}$	$3 \times 10^{-6} – 3 \times 10^{-4}$
Visible Light	$10^{14} – 10^{15}$	$7 \times 10^{-7} – 4 \times 10^{-7}$
Ultraviolet	$10^{15} – 10^{17}$	$3 \times 10^{-10} – 3 \times 10^{-8}$
X-Rays	$10^{18} – 10^{20}$	$3 \times 10^{-12} – 3 \times 10^{-10}$
Gamma Rays	$\geq 10^{20}$	$\leq 3 \times 10^{-12}$

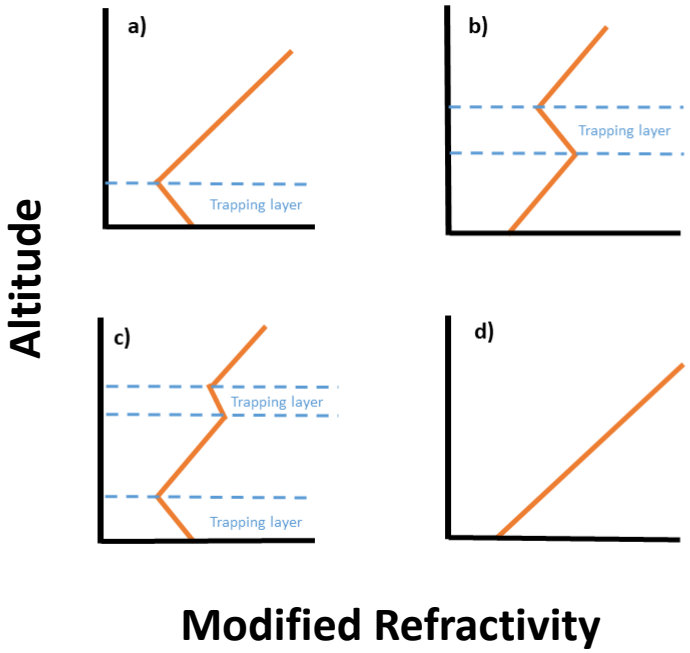

Figure 1. Modified refractivity profiles in surface ducting conditions (a), elevated ducting conditions (b), combination duct conditions (c), and normal atmospheric (non-ducting) conditions (d).

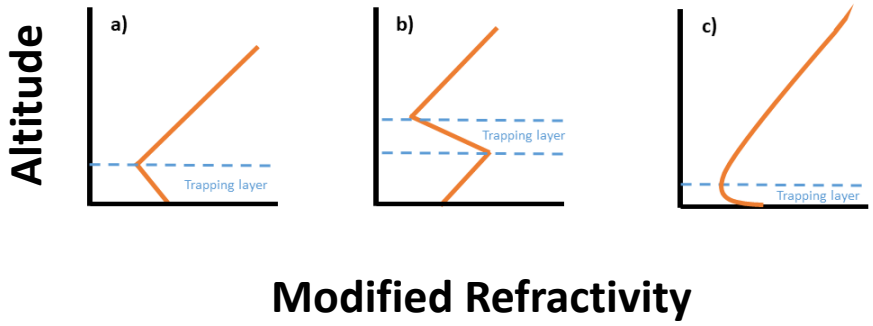

Figure 2. Modified refractivity profiles of a surface-based duct with a surface trapping layer (a), an elevated surface duct with a trapping layer beginning above the surface (b), and a humidity-driven evaporation duct (c).

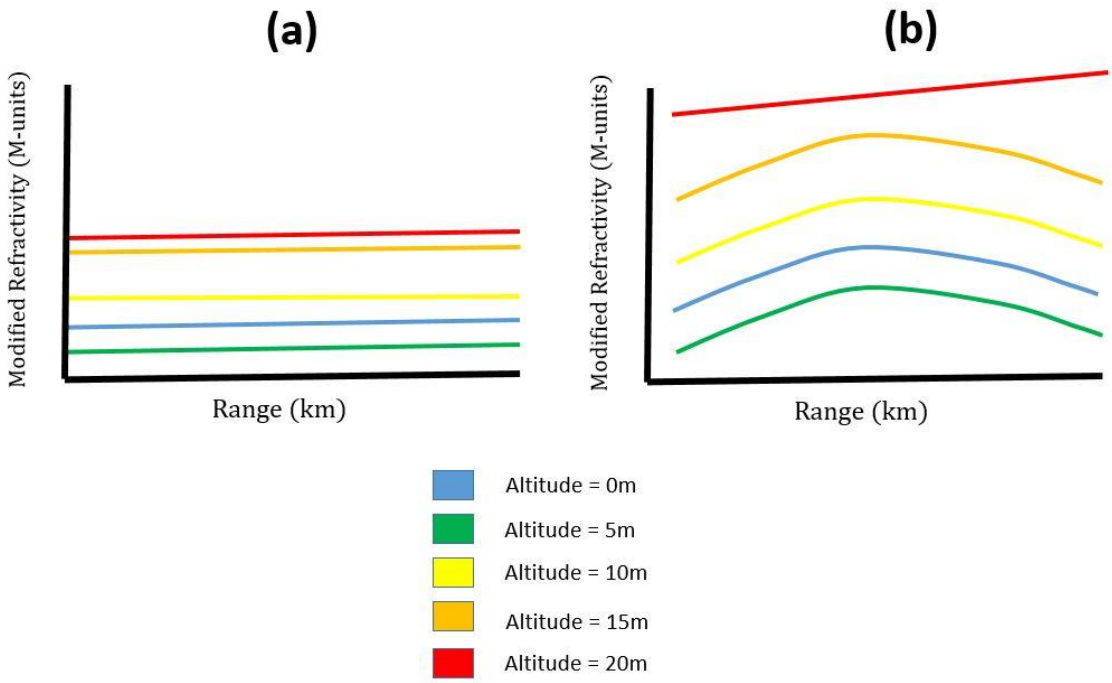

Figure 3. Examples of a horizontally homogeneous refractivity environment (a) and horizontally heterogeneous refractivity environment (b).

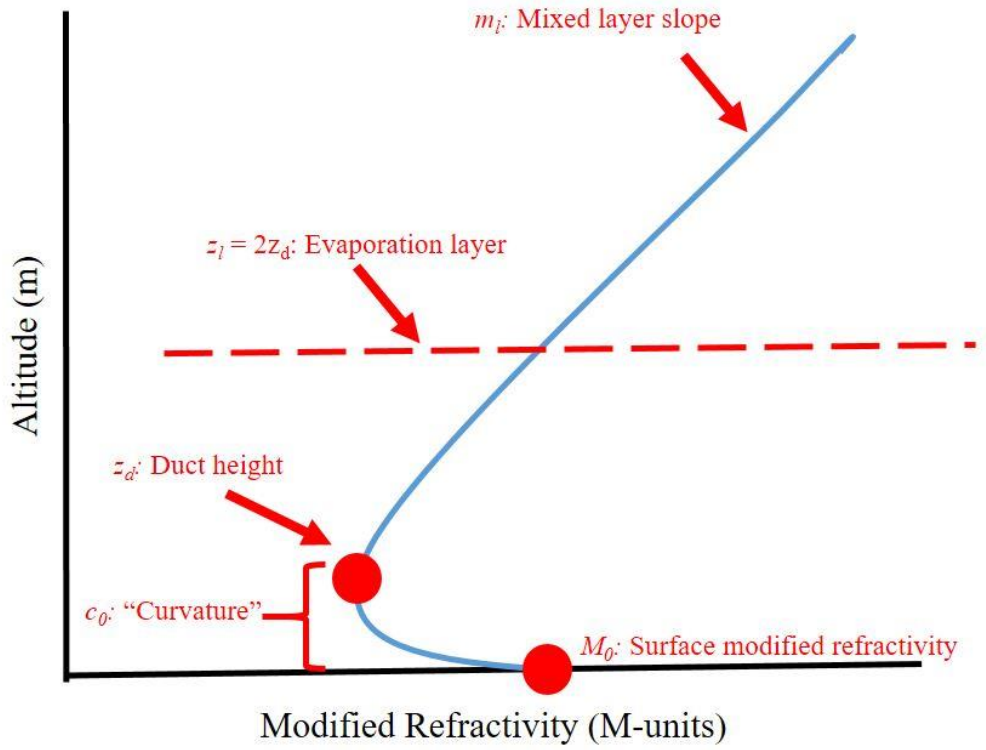

Figure 4. A modified refractivity profile illustrated via parametric refractivity model used by Penton and Hackett (2018).

3.0 Research Objective

The objective of the current study is to investigate range-dependent variations of modified refractivity, duct heights, and refractivity gradients in order to develop a range-dependent parametric model to enhance refractivity predictions utilizing inversion techniques. Range variations of modified refractivity and associated parameters are explored using numerical data to develop the range-dependent parametric model. The developed range-dependent parametric model is evaluated by comparing its estimates of modified refractivity and associated PL to those from numerical data. These comparisons allow assessment of the accuracy of the parametric model and evaluation of whether a single parametric model can accurately represent horizontally heterogeneous vertical refractivity distributions. The parametric model's parameters can be approximated using inversion methods enabling estimation of heterogeneous refractivity environments utilizing *in-situ* radar propagation measurements without information from NWP models or atmospheric measurements.

4.0 Methods

To address the research objective, a blend of numerical weather prediction data and surface layer models which utilize MO theory, are considered to investigate changes in refractive attributes over range. The data sources are described in section 4.1. Refractive environments from the data sources are used to simulate radar wave propagation, which is used to evaluate which range variations of refractive attributes impact propagation most. The application of refractive environments to the propagation model is described in section 4.2. Changes in refractive attributes over range are examined for all data sources to identify potential functional forms that accurately describe variations of each variable in range that affect propagation. The methods for characterization of variations are described in section 4.3. Typical functional forms are used to develop a range-dependent parametric model. Refractive environments produced by the proposed parametric model are evaluated using methods outlined in section 4.4.

4.1 Data Sources

A plethora of data from the Coupled Air-Sea Processes and Electromagnetic Ducting Research (CASPER) project, sponsored by the Office of Naval Research (ONR) Multi-University Research Initiative (MURI) is utilized in this study. The CASPER project aimed to better quantify atmospheric and oceanic effects on the propagation of radar and communication signals in the marine environment (Wang et al., 2018). Two major field campaigns were included in the CASPER project: CASPER-East and CASPER-West. Data

gathered from the former campaign (CASPER-East) is investigated since its focus was to assess the effects of heterogeneous marine environments on EM propagation and quantifying uncertainties in evaporation duct modeling. CASPER-East measurements were taken offshore of Duck, North Carolina (NC) between October 12 and November 6, 2015. Duck was the premier choice of location for CASPER-East due to the Gulf Stream's influence on sea surface temperature (SST) and salinity variabilities that drive heterogeneous refractivity environments (Wang et al., 2018). The CASPER-East data includes repeated tethered balloon measurements, time-averaged meteorological data taken aboard research vessels (R/V), and NWP forecasts.

Repeated tethered balloon measurements made from small crafts outside the areal effects of the larger vessels throughout the CASPER-East campaign measure evaporation ducts. These evaporation ducting refractivity profiles are generated from a "cloud" of data captured by the balloons to generate mean refractivity profiles (Kang and Wang, 2016). These mean profiles are exemplified in Figure 5.

Time-averaged meteorological data – referred to as bulk data – from the CASPER-East field campaign can also be used to estimate evaporation ducts. More specifically, bulk measurements are used in the COARE 3.0 boundary layer model (Fairall et al., 1996; Fairall et al., 2003). In order to estimate temperature, humidity, and wind profiles, COARE requires reference height estimations of wind speed, specific humidity, and temperature along with sea-surface measurements of temperature, specific humidity, and wave characteristics (significant wave height and peak wavenumber). These parameters are obtained from instruments located on the R/V *Sharp* and Duck pier. Temperature, wind speed, and specific humidity at a reference height of 12 meters is used for R/V *Sharp*

COARE predictions, and at the measurement closest to 10 meters for the pier-based COARE predictions. Specific humidity at the surface is estimated assuming 98% relative humidity and using a saturation value based on the SST (Buck, 1981). R/V *Sharp* COARE predictions use an estimated SST taken aboard the R/V *Sharp*, while pier-based COARE predictions use a measured SST from a second ship (R/V *Atlantic Explorer*). Sea surface significant wave height and peak wavenumber are obtained from one of five mini wave buoys in the vicinity of the other measurements (Kammerer and Hackett, 2017; Wang et al., 2018). 1D wave spectra every 30 minutes are measured by the buoy and the spectra closest in time by the buoy located nearest to the respective measurements is used to estimate significant wave height and peak wavenumber. Sample time series of the average quantities used as input for the COARE 3.0 algorithm are shown in Figure 6, and sample refractivity profiles based-on the COARE 3.0 algorithm are illustrated in Figure 7. The GPS position of the ship over time is used to convert the time series of refractivity profiles to range distributions.

Numerical weather prediction data throughout the CASPER-East campaign also estimates evaporation ducts and is the primary dataset utilized in this study. CASPER-East NWP data blends a coupled ocean-atmosphere model with a surface layer model. Coupled model data is integral for this study because evaporation ducts are a coupled atmospheric-oceanic phenomenon (Skolnik, 1990). This data is particularly useful for this study because it allows an instantaneous assessment of an environment, has broad spatial coverage, the finest (~2.04 km) horizontal resolution of any data set investigated in CASPER-East, and fine (~0.1 m) vertical resolution which is needed to identify evaporation ducts.

The Coupled Ocean/Atmosphere Mesoscale Prediction System (COAMPS®) is the coupled ocean-atmosphere NWP model (Hodur, 1997) developed by the Naval Research Laboratory (NRL) and utilized during CASPER-East. COAMPS® predicts mesoscale atmospheric phenomena, and includes an atmospheric data assimilation system comprised of data quality control, analysis, and initialization. COAMPS® contains a nonhydrostatic atmospheric model as well as a hydrostatic ocean model (Hodur, 1997). The initial boundary conditions are estimated from the Naval Operational Global Atmospheric Prediction System (NOGAPS; Hogan and Rosmond, 1991; Peng et al., 2004). COAMPS® forecasts for this study use a 3rd level nested grid having horizontal resolution of approximately 2 km and are cross shore transects from Duck Pier (North Carolina; 36.18°N, 284.27°E) to 60 km offshore. Seventy-one levels are distributed vertically between 4m and 4000 m, and 6 levels reside in the lowest 100 meters. Since this vertical resolution is insufficient for resolving evaporation ducts, the COAMPS® forecasts are blended with the Navy Atmospheric Vertical Surface Layer Model (NAVSLaM; Frederickson, 2016), to increase accuracy and resolution in the lowest 100 m (Karimian et al., 2013).

NAVSLaM characterizes near surface radio-frequency refractivity over the ocean using algorithms based on MO-theory (section 2.5) to simulate air-sea fluxes and near-surface profiles of temperature and humidity (Frederickson, 2016). The COAMPS®-NAVSLaM blended forecasts have decimeter vertical resolution in the lowest 100 m of altitude above the sea surface. Examples of horizontally heterogeneous refractivity vertical profiles from blended COAMPS®-NAVSLaM forecasts are shown in Figure 8.

COAMPS®-NAVSLaM blended forecasts used in this study estimate conditions off the coast of Duck, NC during the CASPER-East field campaign. These data include 648 forecasts which span a period of time and space where frontal boundaries, coastal zones, horizontal changes in sea surface temperatures caused by the Gulf Stream, clouds, thunderstorms, and heavy rainfall lead to heterogeneous refractive environments. Events such as these that took place during the campaign were recorded by Wang et al. (2018). Furthermore, these data contain a wide range of atmospheric stability environments, as illustrated by gradient Richardson number in Figure 9 (see Section 4.3 for gradient Richardson number definition and stability categorization).

Since COAMPS®-NAVSLaM blended data inherently contains assumptions, other CASPER-East data sources are used to verify variations of COAMPS®-NAVSLaM blended data. Mean refractivity profiles from tethered balloon data along with refractivity profiles from the COARE algorithm throughout the entire CASPER-East experiment are examined in conjunction with closest time-stamped COAMPS®-NAVSLaM blended forecasts to investigate discrepancies between the data sources. Figure 10 shows three respective environments which contain modified refractivity estimates using COAMPS®-NAVSLaM blended data, mean profiles from tethered balloon data, and environments generated using the COARE algorithm and bulk atmospheric measurements. This figure illustrates both consistencies and inconsistencies between the various modified refractivity estimates. Figure 10a is an example of how modified refractivity with respect to height over all ranges and all data sources are consistent, while Figure 10b shows inconsistencies between the blended data and tethered balloon measurements, and Figure 10c shows inconsistencies between the blended data and COARE estimations. 368 COARE-based

modified refractivity profiles from both the pier and research vessel coincide with COAMPS®-NAVSLaM blended modified refractivity forecasts. Although magnitudes of modified refractivity are typically quite different, a majority of modified refractivity profiles show similar refractivity gradients with respect to height (*dM/dz*). 319 of 368 (97%) COARE-estimated modified refractivity profiles from R/V data show similar refractivity gradients, and 303 of 368 (92%) COARE-estimated modified refractivity profiles from the pier show similar refractivity gradients with height. Mean refractivity profiles calculated using tethered balloon data coincide with 36 of the 648 COAMPS®-NAVSLaM blended forecasts. Of these 36 mean refractivity profiles, 29 (80%) show similar refractivity gradients with height to the COAMPS®-NAVSLaM blended forecasts. Thus, measured data from CASPER-East largely verifies the accuracy of the COAMPS®-NAVSLaM blended data used to analyze refractive characteristics in range for this study. Further discussion of the differences between these estimates of refractivity during the Casper-East experiment is included in Pastore et al. (2020).

4.2 EM Propagation Modeling

While the data described in the previous section is used to describe the atmospheric conditions, the developed parametric model will ultimately be of best utility if it accurately predicts propagation. EM propagation is simulated using the Variable Terrain Radiowave Parabolic Equation model (VTRPE; Ryan, 1991). VTRPE computes EM wave propagation in complicated environments, including the MABL (Ryan, 1991) using the parabolic equation approximation to predict electromagnetic fields (Sirkova, 2012). VTRPE uses a cylindrical earth-based coordinate system to solve the parabolic wave equation

implemented using a split-step Fourier method. VTRPE is used in this study to simulate the propagation factor:

$$P_f = 20 \log \left| \frac{\boldsymbol{E}}{\boldsymbol{E_0}} \right| \quad \textbf{(5)}$$

where $\boldsymbol{E}$ is the electric field in the modeled environment, and $\boldsymbol{E_0}$ is the electric field in free space propagation conditions, and the propagation loss is:

$$P_L = 20 \log(2k_o r) - P_f \quad \textbf{(6)}$$

where k_o is the wavenumber of the electromagnetic wave and r is range (Ryan, 1991). The VTRPE model requires specification of the antenna properties, domain, sea state parameters, and atmospheric refractivity. For this study, propagation patterns generated utilizing a developed range-dependent parametric model are compared to those generated using COAMPS®-NAVSLaM blended data to evaluate the accuracy of the modeled refractive environment (i.e., the developed parametric model) in terms of propagation prediction. This study investigates propagation over a smooth sea surface, and an antenna transmitting at an altitude of 15.6 m at 9GHz with a beam width of 15° and horizontal polarization. Figure 11 shows an example of a horizontally heterogeneous refractivity environment through the use of vertical profiles as well as a range-averaged vertical profile. Figure 12 shows the resulting propagation patterns for the mean profile illustrated in Figure 11, the range-dependent refractivity environment from Figure 11, and a single profile at a range (r) of 0 km (Figure 11), which is assumed homogenous over range. Clearly, the different refractivity environments (i.e., homogenous vs. heterogeneous) have a substantial impact on the propagation with propagation losses being significantly lower at long range in the range-dependent refractive environment (Figure 12b).

4.3 Methods for Characterizing Variations of Refractive Attributes Over Range

In order to ascertain which variables should be considered for a range-dependent parametric model, methods of visual inspection, standard deviation, and fast-Fourier transforms are performed on the variations of refractive attributes over range. Typical variations in range and their effects on radar wave propagation are investigated to determine which variations cause more dramatic impacts on radar wave propagation. Furthermore, variations are examined with respect to the stability of the environment, which is evaluated using gradient Richardson number, and correlation coefficients between stability and refractive attributes in range to ascertain if certain variations are more likely associated with stable, unstable, or free convective stability regimes.

Standard deviations for a variety of variables with respect to range are calculated using the following equation:

$$\sigma_x = \sqrt{\frac{\sum_{i=1}^{n_{x_r}} (x_i - \bar{x})^2}{n_{x_r} - 1}} \qquad \textbf{(7)}$$

where n_{x_r} is the number of data points in range, x_r is a refractive attribute analyzed with respect to range (e.g., modified refractivity, duct height, etc.), and $\bar{x}$ is the mean of that respective variable over range. Since standard deviations vary with altitude they are calculated for each altitude. The standard deviations along with visual inspection are used to determine simplistic functional forms which may accurately model these range-dependent variations.

In cases where variations are oscillatory, signals of the variable over range are investigated using fast-Fourier transforms (FFTs) to determine the length scales which

attribute the most variance to the signal. The variables are de-trended in range by removing the best (least squares) straight-line or linear trend in order to remove any large scale variations that aren't resolved by the data. Then, an FFT is used to calculate the power spectral density (PSD) on the de-trended data:

$$S = \frac{2|x_f|^2}{n_{x_r}\Delta r} \quad \textbf{(8)}$$

where Δr is the sampling interval (2.04 km) and x_f are (one-sided) Fourier coefficients. These data allow for length scales between 4.08 km and 63 km to be resolved. For variations which are also altitude dependent, PSDs are calculated for each altitude. The PSDs are also investigated with respect to atmospheric stability to determine whether certain length scales dominate in stable, unstable, or free convective stability scenarios.

The atmospheric stability is examined via the gradient Richardson number:

$$Ri(z,r) = \frac{\frac{g}{T_v}\frac{\partial \theta_v(z,r)}{\partial z}}{\left(\frac{\partial U(z,r)}{\partial z}\right)^2 + \left(\frac{\partial V(z,r)}{\partial z}\right)^2} \quad \textbf{(9)}$$

where g is gravitational acceleration, θ_v is virtual potential temperature, T_v is the average virtual temperature over all altitudes between the surface and 5 meters above the surface, and *U* and *V* are the wind components towards the east and north, respectively. Ri is calculated at each altitude from the surface (z = 0 m) to a reference height of z = 5 m and at each range. The reference height of 5 meters is chosen based-on Hansen (1967) which states that a reference height between 3-6 meters above the surface provides the best estimate of Richardson number in respect to the energy balance of the air-earth interface. $Ri(z,r)$ is utilized to investigate how stability relates to frequently seen functional forms

with respect to range, and to discern relationships between stability and other range-varying variables. To investigate how stability relates to functional forms, sometimes an average gradient Richardson number is used by either averaging $Ri(z,r)$ over both range and altitude ($\overline{Ri}$), or averaging only over altitude ($\overline{Ri}(r)$). Stability environments are defined as stable if $Ri > 0$, unstable if $0 > Ri > -2$, and free convective if $Ri \leq -2$.

In order to determine relationships between many variables in this study correlation coefficients are computed:

$$C_{xy} = \frac{\sum_{i=1}^{n_{x_r}}(x_i - \bar{x})(y_i - \bar{y})}{(n_{x_r} - 1)(\sigma_x \sigma_y)} \quad \textbf{(10)}$$

where y is another variable which varies in range, σ_y is the standard deviation of y, and $\bar{y}$ is the average of y over range. Correlation coefficients are used to find direct or indirect relationships between atmospheric stability and various range-dependent variables as well as evaluate discrepancies between the developed parametric model and the COAMPS®-NAVSLaM blended data.

4.4 Range-Dependent Parametric Model Evaluation Methods

The functional forms investigated to model range-dependent refractive environments are evaluated using either linear or non-linear least squares regression. Regressions fit a variety of different equations based on functional behaviors of duct height and refractive gradients with respect to range, as well as refractive gradients with respect to altitude. RMSEs between a data variable from COAMPS®-NAVSLaM blended profiles and the fit of the same variable are calculated:

$$\alpha_x = \sqrt{\frac{1}{n_{x_r}} \sum_{i=1}^{n_{x_r}} (x_i - \hat{x_i})^2} \quad \textbf{(11)}$$

where $\hat{x_i}$ represents the fit of the estimated variable at each range using linear or nonlinear least squares regression.

In some cases, it is difficult to determine the accuracy based on α_x alone because values of the respective variable may vary up to 2 orders of magnitude. This large variance makes it difficult to compare α_x to typical values of the respective variable. Thus, a percent error in decimal form is calculated using α_x and the mean of the respective variable over range and/or altitude (μ_x):

$$E = \frac{\alpha_x}{|\mu_x|} \quad \textbf{(12)}$$

The range-dependent parametric model developed in this study is evaluated through comparisons of range-dependent *M* profiles and associated simulated propagation loss. Range-dependent *M* profiles generated through the use of the parametric model are compared to range-dependent COAMPS®-NAVSLaM blended *M* profiles by calculating residuals and RMSEs between the two *M* profiles. Residual of the modified refractivity is calculated:

$$\beta_M(r,z) = M(r,z) - \widehat{M}(r,z) \quad \textbf{(13)}$$

where $M(r,z)$ represents modified refractivity from a data source, and $\widehat{M}(r,z)$ represents modified refractivity calculated using the developed parametric model. The RMSE is calculated:

$$\alpha_M = \sqrt{\frac{1}{n_M}\sum_{i=1}^{n_M}(\beta_M(r,z))^2} \quad \textbf{(14)}$$

where n_M is the number of modified refractivity measurements over range and height. Histograms of the residuals and RMSEs are generated for range-dependent refractivity profiles for all COAMPS®-NAVSLaM blended data sets, which contain only evaporation ducts, to determine how optimally the proposed parametric model reproduces refractivity. $\beta_M(r,z)$ spatial distributions are used to identify the location of errors, which determine where, in space, the range-dependent parametric model performs well and where it performs poorly. Furthermore, correlation coefficients are calculated between α_M and each α_x.

Simulated propagation loss patterns generated from refractivity based on the parametric model and those generated using the data sources are compared by analyzing the residuals and RMSEs of the propagation loss. These propagation loss metrics identify which regions of the propagation pattern differ between PL produced by the refractivity data relative to PL based on refractivity via the parametric model. Residuals of propagation loss patterns are calculated similarly as the modified refractivity residuals:

$$\beta_{PL}(r,z) = P_L(r,z) - \widehat{P_L}(r,z) \quad \textbf{(15)}$$

where $P_L(r,z)$ is the propagation loss simulated using the data source refractivity profiles and $\widehat{P_L}(r,z)$ is propagation loss simulated using the developed parametric refractivity model. RMSE for propagation loss patterns is calculated:

$$\alpha_{PL} = \sqrt{\frac{1}{n_{PL}} \sum_{i=1}^{n_{PL}} (\beta_{PL}(r,z))^2} \quad \textbf{(16)}$$

where n_{PL} is the number of propagation loss data points over range and height. Histograms of the residuals and RMSEs are generated for propagation loss environments for all COAMPS®-NAVSLaM blended profiles to evaluate the accuracy of the parametric model. The histograms are used to identify how frequently the parametric model accurately reproduces the propagation. $\beta_{PL}(r,z)$ spatial distributions are used to identify the location of errors, which can determine where, in space, propagation predictions differ most.

Thus, performance of the parametric model is assessed based on errors of functional forms used to model refractivity environments using α_x, E, β_M and α_M, as well as the associated propagation loss predictions from VTRPE using β_{PL} and α_{PL}. These metrics allow discussion on the developed parametric model's strengths and weaknesses.

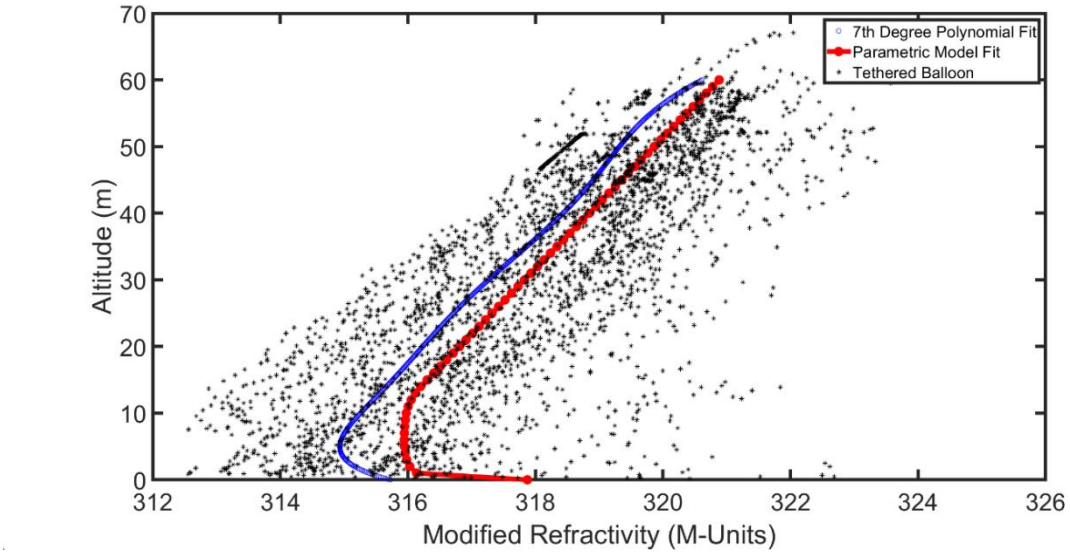

Figure 5. Modified refractivity from tethered balloon temperature and humidity measurements collected on October 20, 2015 at 13:41:52 UTC. Two mean refractivity profiles are shown. The blue line shows a mean profile based-on a least squares fit to a seventh degree polynomial performed by Kang and Wang (2016), and the red line shows a mean profile based-on a least squares fit to the parametric model described by Equation 4.

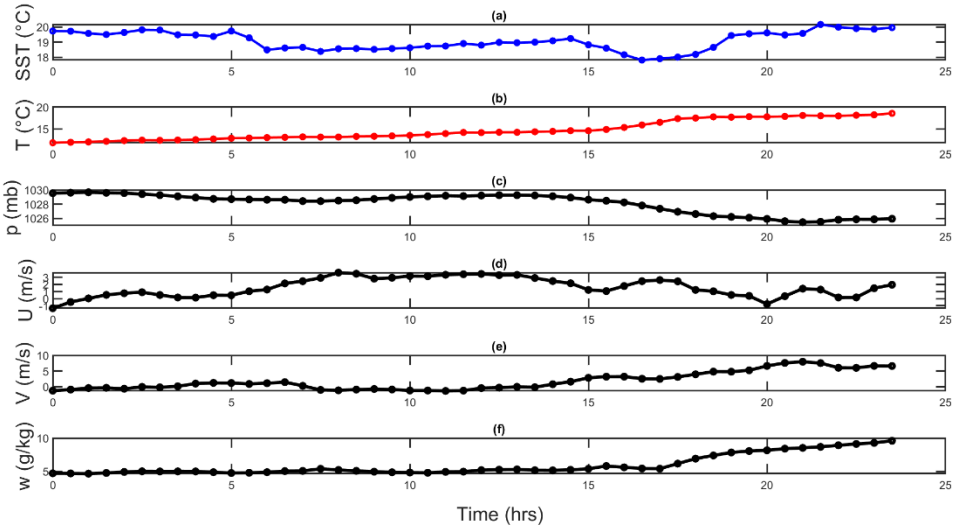

Figure 6. Example of bulk measurements used to estimate range-dependent modified refractivity environments using the COARE 3.0 algorithm for October 20, 2015 starting at 13:41:52 UTC during the CASPER-East campaign. Times series are shown for a) sea surface temperature (SST), b) air temperature 10 meters above the ocean surface (*T*), c) atmospheric pressure at 12 meters above the ocean surface (*p*), d) and e) show the horizontal components of wind speed (*U*, *V*), and f) shows the mixing ratio at 12 meters above the ocean surface (*w*).

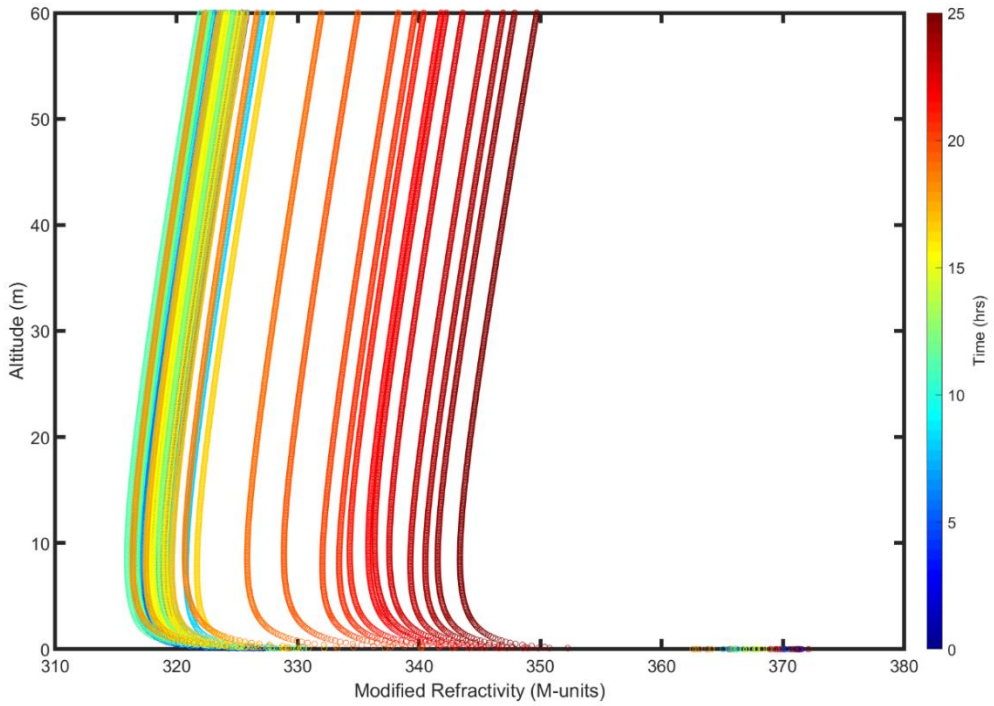

Figure 7. Modified refractivity profiles based-on the COARE 3.0 algorithm using the bulk measurements shown in Figure 6.

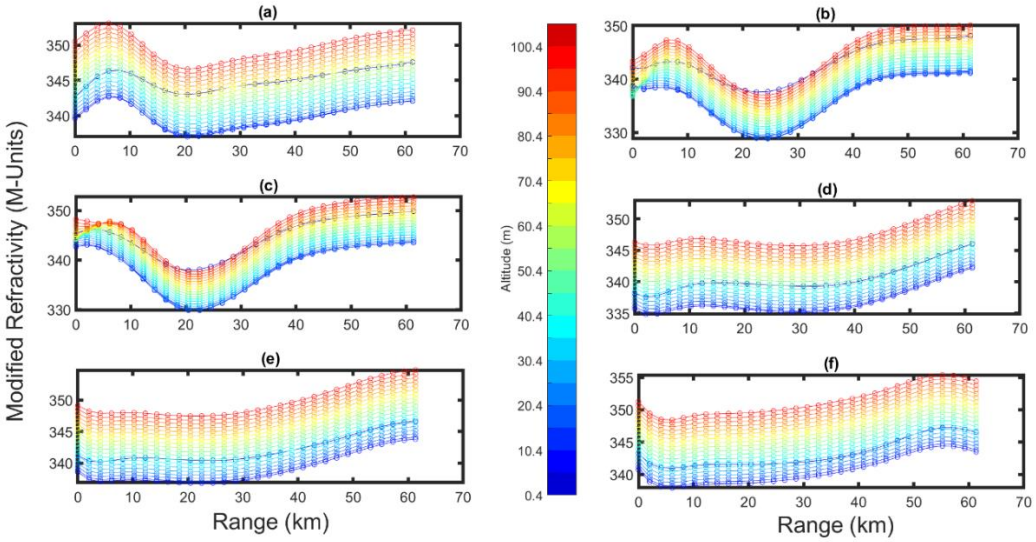

Figure 8. Examples of range-dependent refractivity using blended COAMPS®-NAVSLaM forecasts. Refractivity versus range are shown for every 5m of altitude. Forecasts are arbitrarily chosen examples for a) October 20, 2015 12:00Z forecast hour 12, b) October 21, 2015 00:00Z forecast hour 1, c) October 21, 2015 00:00Z forecast hour 2, d) October 21, 2015 12:00Z Forecast hour 5, e) October 21, 2015 12:00Z forecast hour 6, and f) October 21, 2015 12:00Z forecast hour 7.

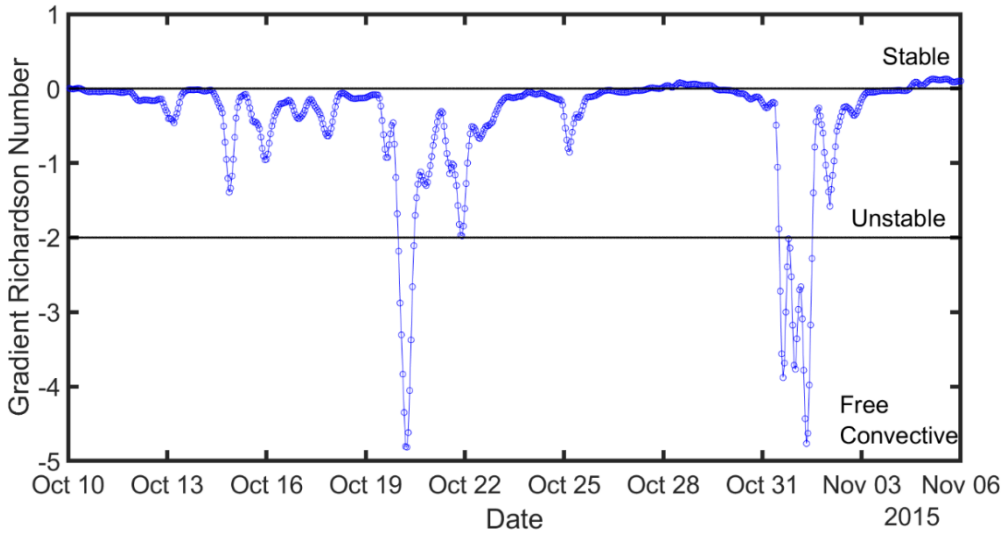

Figure 9. Gradient Richardson number calculated for each COAMPS®-NAVSLaM blended forecast during the CASPER-East experiment. All three types of stability regimes are contained in the time series with unstable conditions being the most common.

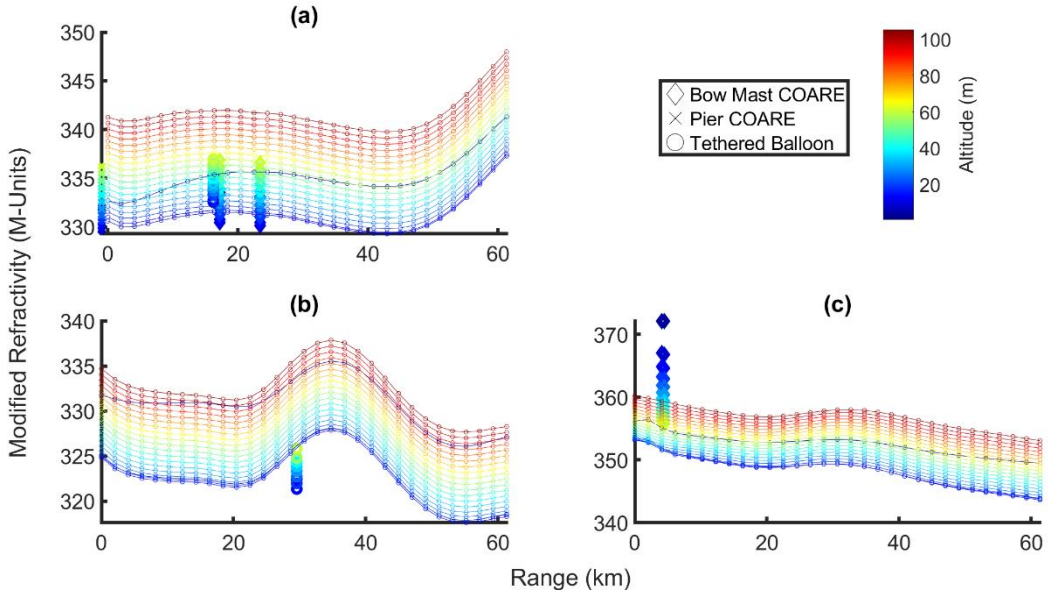

Figure 10. Modified refractivity with respect to range and altitude from multiple data sources. (a) shows COAMPS®-NAVSLaM blended modified refractivity data from October 21st, 2015 model run 12:00Z forecast hour 2 shown by small open dots with connected lines, along with COARE 3.0 using both time-averaged bow-mast measurements from the R/V Sharp on October 21st, 2015 at 13:42Z and 14:12Z, as well as time averaged measurements from Duck pier on October 21st, 2015 at 13:40Z, 14:00Z, and 14:20Z. (a) also shows 7th order polynomial fitted tethered balloon modified refractivity data taken on October 21st, 2015 at 14:29Z. (b) shows COAMPS®-NAVSLaM blended data from October 17th, 2015 model run 12:00Z forecast hour 6, along with a tethered balloon measurement taken on October 17th, 2015 at 18:06Z. (c) shows COAMPS®-NAVSLaM blended data from October 25th, 2015 model run 12:00Z forecast hour 8 along with data from COARE using measurements from the bow mast of the R/V Sharp on October 25th, 2015 at 19:42Z and 20:12Z.

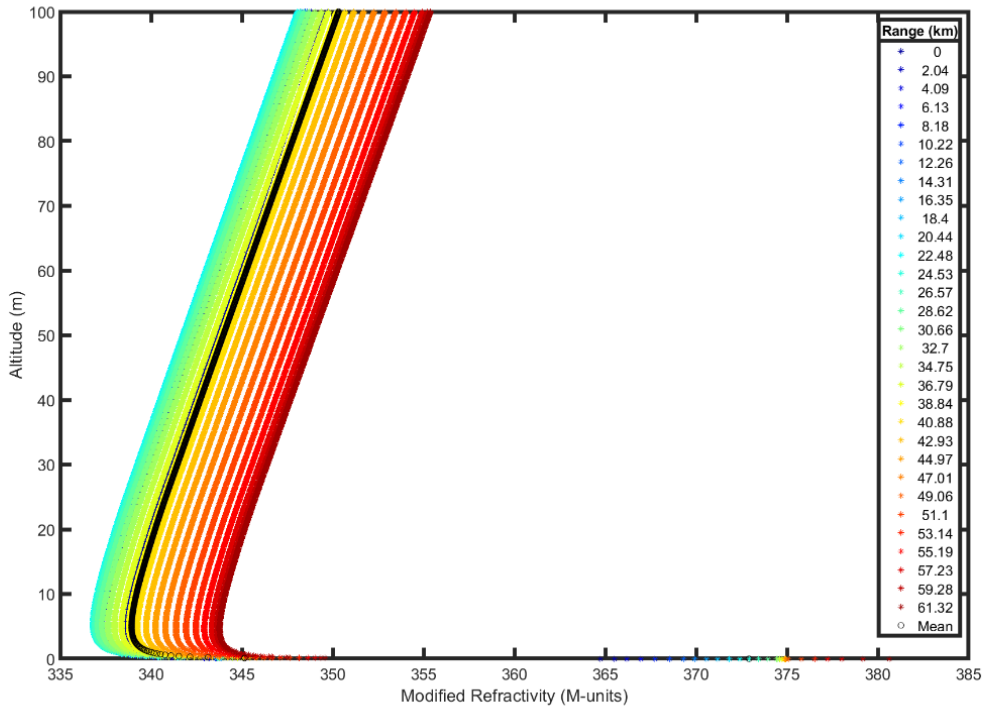

Figure 11. Modified refractivity with respect to height at various ranges along with a range-averaged (mean) profile (black) used for VTRPE propagation predictions in Figure 12. All profiles are from COAMPS®-NAVSLaM blended profiles for October 21st, 2015 model run 12:00Z forecast hour 6.

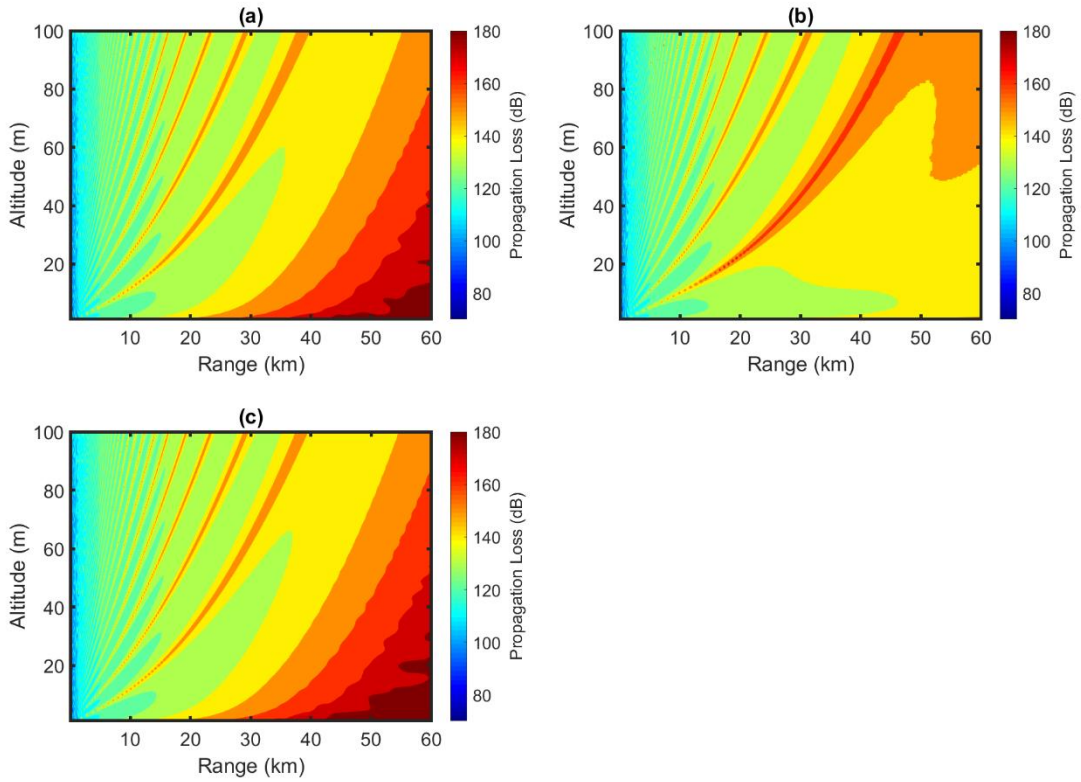

Figure 12. Figures a-c show VTRPE propagation loss predictions using different modified refractivity profiles from Figure 11. (a) uses the mean modified refractivity profile and assumes horizontal homogeneity, (b) uses a range-dependent refractivity environment from Figure 11 (except the mean profile), and (c) uses the modified refractivity profile at r = 0 km and assumes horizontal homogeneity.

5.0 Results

5.1 Characterization of Range-Dependent Variations

Development of a range-dependent refractivity parametric model for use in inversion problems requires understanding which horizontally heterogeneous environmental variables cause the greatest impact on radar wave propagation. Previous studies have investigated which environmental parameters have impact on radar wave propagation in homogeneous refractive environments (Dogget, 1997; Gerstoft et al., 2003; Haack et al., 2010; Lentini and Hackett, 2015). Some parameters investigated in these studies come from previously developed parametric refractivity models by Gerstoft et al. (2003) or Paulus (1985, 1990), which include parameters such as duct height, duct curvature, and mixed layer slope (Saeger et al., 2015). Although much is known about how these parameters effect propagation in homogeneous environments, few have investigated what effects these parameters have on propagation if the parameters are horizontally heterogeneous (Brooks, 2001; Atkinson and Li, 2001). In this study, the impact of horizontally heterogeneous modified refractivity and associated refractivity characteristics: duct height and refractive gradients are investigated to determine their influence on propagation, as well as their relationship to atmospheric stability.

5.1.1 Modified Refractivity Variations over Range

The standard deviation of modified refractivity is calculated over range for each altitude for each COAMPS®-NAVSLaM blended modified refractivity forecast during the CASPER-East field experiment. The mean standard deviation of modified refractivity with respect to range over all altitudes and all forecasts is 2.35 M-units, while the median is 1.13 M-units. This result indicates that in most forecasts, modified refractivity typically varies 1 - 2 M-units from the average over range at each altitude. However, the maximum standard deviation of modified refractivity with respect to range over all altitudes and all forecasts is 13 M-units while the minimum is approximately 0 M-units, indicating modified refractivity can vary dramatically over range. Upon visual inspection, these variations of modified refractivity in range are mostly distributed in oscillatory patterns. Figure 13 shows a few examples illustrating oscillatory distributions, and Figure 14 illustrates respective spectrograms of the power spectral density of modified refractivity over range for each altitude. In all cases, the spectra show that the lowest resolved wavenumber (0.0158 km^{-1}) generally contributes the most variance to modified refractivity in range. However, Figures 14c and 14d show large variance associated with slightly higher wavenumbers (0.0316 km^{-1}, and 0.0474 km^{-1}) as well. The variations of modified refractivity at these scales (~62 km, ~31 km, ~21 km) could be caused by many meteorological processes that can affect environments over these same scales such as land/sea interactions, synoptic weather fronts, or thunderstorms. For example, land/sea interactions include differential heating resulting in land/sea breezes, which change the temperature and humidity structure over the ocean surface over these scales (~62 km, ~31 km, ~21 km). Synoptic fronts change temperature, pressure, and humidity over the largest

of these scales (~62 km), which in-turn influences refractivity. Lastly, thunderstorms, which typically are around the size of 24 km (~15 miles), can cause changes of temperature and humidity at scales similar to their size. Thus, thunderstorms taking place within the range of a measurement could contribute to the smaller scale oscillatory modified refractivity variations (~21 km). The refractivity variations in range of a single forecast at all altitudes are similar indicating that the atmospheric phenomena influencing them are relatively similar within the surface layer (lowest 100 m of altitude).

To investigate the environmental effects which cause differences between separate forecasts in the variations of modified refractivity in range, peak wavenumbers from the spectrograms (e.g., Figure 14) are classified by the stability of the environment. The peak wavenumber is the wavenumber which contains the highest PSD for each altitude, and stability is evaluated using $\overline{Ri}$ with categorized stability regimes as outlined in Section 4.3. Figure 15 illustrates histograms of peak wavenumber for all altitudes for all COAMPS®-NAVSLaM blended profiles. Unstable environments show six wavenumbers that frequently appear as the peak wavenumber (0.0158 km^{-1}, 0.0316 km^{-1}, 0.0474 km^{-1}, 0.0633 km^{-1}, 0.0791 km^{-1}, and 0.0949 km^{-1}), while stable environments show four wavenumbers (0.0158 km^{-1}, 0.0316 km^{-1}, 0.0474 km^{-1}, and 0.0633 km^{-1}), and free convective environments only show 3 wavenumbers (0.0158 km^{-1}, 0.0316 km^{-1}, and 0.0474 km^{-1}). Thus, range-dependent parametric models which include unstable environments should consider functions that can model higher wavenumber variations of modified refractivity with range.

To determine whether the observed typical variations in modified refractivity with range (1-2 M-units) are meaningful to propagation when introduced as a bias (or offset),

radar wave propagation predictions are investigated using the VTRPE simulation (see Section 4.2). Range-dependent modified refractivity environments where only surface modified refractivity is varied over range is considered. This analysis provides insight about the importance of changes in the magnitude of modified refractivity on propagation as compared to variations in the vertical refractive gradients (*dM/dz*) (discussed in a subsequent subsection). Figure 16 illustrates refractivity profiles that result from shifting surface modified refractivity in range by 2 M-units per 10 kilometers over a range of 60 kilometers (Figure 16a), 5 M-units per 10 kilometers over a range of 60 kilometers (Figure 16c), and 10 M-units per 10 kilometers over a range of 60 kilometers (Figure 16e). No refractive gradients (*dM/dz*) nor duct heights are changed, both of which have been reported to effect radar wave propagation (Turton et al, 1988; Skolnik, 1990). Propagation from environments whose modified refractivity are shifted over range (Figures 16a, 16c, 16e) are compared to propagation in a homogeneous environment. The difference in propagation between these range-dependent and range independent refractivity environments are illustrated in Figure 16 (b, d, and f). These results show that shifting surface modified refractivity over range relative to an assumed homogeneous environment changes propagation loss by less than 1 dB, indicating minimal effects on propagation. This result is expected because the refractive gradient with respect to height (*dM/dz*) affects Maxwell's equations for EM wave propagation not the refractivity itself (Craig and Levy, 1991). Thus, other parameters such as duct height and refractive gradients (*dM/dz*) and their variations over range are considered for a range-dependent parametric model rather than the refractivity itself. Although such a parametric model wouldn't directly parameterize modified refractivity with respect to range as most refractivity parametric

models of its kind do (Penton and Hackett, 2018; Gerstoft et al., 2003; Paulus, 1985; Paulus, 1990), it would still need to enable estimation of modified refractivity profiles, which is necessary for propagation simulations and inversion studies.

5.1.2 Duct Height Variations Over Range

Duct heights are determined by the altitude where the modified refractivity gradient (*dM/dz*) is closest to zero. The highest altitude below 40 m which has a positive refractivity gradient and is preceded by two altitudes which have negative refractivity gradients is considered to be the duct height. These duct heights are calculated at each range for each investigated modified refractivity environment and are used to investigate typical duct height variations over range.

The standard deviation of duct heights over range for all COAMPS®-NAVSLaM blended forecasts which contain evaporation ducts, but do not contain elevated ducts are investigated. The mean standard deviation of duct height over range for all of the examined forecasts is 0.94 m, while the median standard deviation is 0.44 m. This result indicates that in most forecasts, the duct height varied by at most 1 meter from the average duct height over range. However, the maximum standard deviation is approximately 5 meters, signifying that duct height can vary significantly over range, while the minimum is approximately 0 meters. These results align with previous studies including Brooks et al. (1999), Yang et al. (2015), and Brooks (2001) which reported evaporation duct heights varying by just a few meters over ~200 kilometers. The similarities amongst results may be attributed to the coastal environments explored in each of these studies, suggesting that duct height variations of only a few meters over range are typical in coastal environments.

The small mean and median standard deviations of duct height could suggest that the homogeneity assumption would be a reasonable approximation of duct height for ~80% of these forecasts. However, Figure 17 investigates the effects on propagation of an environment whose duct height varies linearly by 1 meter over 60 kilometers (the average variation of this data set) and an environment whose duct height varies by 5 meters over 60 kilometers (the maximum variation of this data set) relative to an assumed homogenous duct height in range. These results illustrate that although more drastic differences in propagation loss are evident when the duct height linearly varies by 5 meters (Figure 17c and 17d), there are locations of more than 10 dB propagation loss discrepancies at long range when the duct height varies linearly by only 1 meter (Figure 17a and 17b), suggesting that duct height variances of 1 meter can cause non-negligible effects on radar wave propagation in some locations relative to assuming a homogenous duct height in range. Furthermore, since 83 of the 460 forecasts produce standard deviations greater than 1, 20% of the forecasts show significant changes in duct height over range.

A majority (77% of all forecasts) of duct heights vary linearly over range, matching the assumption by Zhao et al. (2017), while some illustrate sinusoidal distributions (11% of all forecasts), step-like distributions (9% of all forecasts), or constant distributions (2% of all forecasts). Examples of these distributions are illustrated in Figure 18. Because linear distributions occur in a majority of the COAMPS®-NAVSLaM blended forecasts and linear distributions may be modeled using an oscillating function with low frequency, the effects of both distributions on propagation are investigated to determine which might have a larger influence on propagation. The maximum standard deviation of duct height over range examined in the COAMPS®-NAVSLaM blended data for both linear and sinusoidal

distributions is used to examine the most extreme propagation effects. Figure 19 shows a linear duct height variation of 15 meters over 50 kilometers, and a sinusoidal duct height variation, which oscillates with 3 m amplitude around a 10 meter duct height, where the standard deviations of duct height in range are ~5 m and 2 m, respectively. Figure 20 illustrates corresponding differences in propagation relative to an assumed homogenous environment. The linear variations of duct height in range show more drastic effects on propagation, especially at low altitudes and long ranges, consistent with the previously mentioned finding (Figure 17).

In order to understand the meteorological effects that relate to duct height variations in range, stability is examined using gradient Richardson number. $\overline{Ri}$ for each forecast is classified with respect to the type of duct height range variation and shown in Figure 21. These results illustrate that duct height variations in range which are flat or show step-like distributions occur mostly during near-neutral or stable environments, while sinusoidal and linear distributions occur during mostly unstable and, in some cases, free convective environments. In order to determine a relationship between duct height and stability, $\overline{Ri}(r)$ is correlated to duct height with respect to range for each forecast. A histogram of the correlation coefficients between these variables is shown in Figure 22. The histogram shows that the highest number of forecasts have correlation coefficients between the range of 0.8 and 1, indicating that ~20% of the cases contain a direct relationship between $\overline{Ri}(r)$ and duct height. However, there are also cases that indicate an inverse relationship, and many with approximately no correlation. Thus, although 20% of the cases show a direct relationship, there seem to be additional factors affecting the duct height variations in range that requires further investigation.

In summary, duct heights which vary by amounts as small as 1 m over 60 km can cause non-negligible effects on propagation relative to a homogenous environment and a majority (77%) of the duct heights investigated in this study are found to be linearly distributed in range. Also, linearly distributed duct heights with respect to range exhibit stronger effects on propagation than sinusoidal variations which was the next-most-frequently occurring duct height distribution in this study. Furthermore, duct height variations in range seem to display some dependence on atmospheric stability.

5.1.3 Variations of Refractivity Gradients over Range

Since refractive gradients play an integral role in propagation of radar waves (Craig and Levy, 1991), range variations of vertical refractive gradients (*dM/dz*) are investigated. Variations of refractive gradients over range are examined for all COAMPS®-NAVSLaM blended environments which contain evaporation ducts without elevated ducts. Figure 23 shows an example of refractive gradient distributions in range where it is apparent that the variations are oscillatory, and the amplitude of the refractive gradient variations change with altitude. At low altitudes (below the duct height), gradients are negative and vary in range. At high altitudes (above the duct height), gradients are positive and relatively constant. Figure 24 shows examples of refractivity gradients with respect to height above and below the duct height. In all COAMPS®-NAVSLaM blended data refractivity gradients below the duct height are large and negative, and approach zero as *z* approaches the duct height (Figure 24a), and refractivity gradients above the duct height are positive and asymptote to similar values at all ranges (Figure 24b). These observations are expected because low altitudes contain the duct where refractive gradients are negative. Due to proximity to the surface, complex air-sea interactions can cause refractivity gradients near

the surface to vary rapidly in altitude. The altitudes above the duct height are consistent with a well-mixed layer with positive and nearly uniform refractive gradients. All forecasts of refractive gradient range variations below the duct height are classified into 3 categories: linear distributions (18% of all profiles), oscillatory distributions (79% of all profiles), and a combination of oscillatory and linear distributions (3% of all profiles). Examples of each type of distribution are shown in Figure 25. Because oscillatory and linear distributions are most common, refractivity gradients are varied in both distributions over range similarly at all altitudes and the resulting effects on propagation loss are investigated to determine if oscillatory or linear distributions show greater effects on propagation. Furthermore, environments that illustrate higher frequency oscillations (Figure 26a), lower frequency oscillations (Figure 26c), and linear distributions (Figure 26e) of refractive gradients with respect to range are considered to compare their differing effects on propagation. It should be noted that refractive gradients at the surface are much greater than refractive gradients at higher altitudes, where in some cases, they are different by up to 2 orders of magnitude. Nevertheless, resulting propagation loss difference between each environment exemplified in Figure 26 and their respective homogenous environment is shown in Figure 27. The magnitude of dM/dz variations in each of these cases are relatively similar; thus, propagation differences are assumed to be related to the distributions in range and not the magnitude of the variations. Figure 27 shows that environments with refractive gradients that are sinusoidal over range such as those shown in Figure 27a and 27b, have larger variations in propagation over a larger area than those that have a linear distribution. This result suggests that variations of refractivity gradients that are oscillatory have a greater

impact on propagation than linear variations relative to an assumed homogenous environment.

Environmental effects which cause differences in the sinusoidal variations of surface refractivity gradients in range are investigated via peak wavenumbers classified by atmospheric stability (similar to Section 5.1.1). Peak wavenumbers are identified as the wavenumber, which contains the highest PSD of the surface refractive gradient over range for each forecast. Stability is defined using $\overline{Ri}$ and stability regimes outlined in Section 4.3. Figure 28 illustrates histograms of these peak wavenumbers. Free convective environments frequently have one dominant peak wavenumber (0.0158 km^{-1}), while stable environments commonly have two peak wavenumbers (0.0158 km^{-1}, 0.0316 km^{-1}), and unstable environments frequently have three dominant wavenumbers (0.0158 km^{-1}, 0.0316 km^{-1}, 0.0474 km^{-1}). Similar to modified refractivity peak wavenumbers, unstable environments can contain surface layer refractivity gradient variations in range that involve shorter length scales, while stable and free convective conditions more often contain lower wavenumber (longer length scale) variations. Thus, sinusoidal models parameterizing surface refractive gradients in unstable environments need to consider including higher wavenumber representations to make an accurate estimation than those which are intended for stable or free convective conditions.

The amplitudes of oscillatory variations of refractive gradients over range are investigated to determine if the magnitudes of the amplitudes have an effect on propagation. Differences between the refractive gradient at each range and the mean refractive gradient over range at each altitude are calculated, and the maximum and minimum differences over all ranges and altitudes for each forecast are shown in Figure

29; these maximum and minimum differences are considered to be the (maximum and minimum) amplitude of the refractivity gradient sinusoidal range variations. The amplitudes based on maxima are larger than the minima, suggesting that the variations of *dM/dz* from the mean are asymmetrical with those above the mean value being larger on average. In order to investigate the effects of the sinusoidal amplitude of refractive gradients on propagation, a percent difference for each forecast used in this study is calculated:

$$D = \frac{\left.\frac{dM}{dz}\right|_{\substack{z = z_{max} \\ r = r_{max}}} - \left.\overline{\frac{dM}{dz}}\right|_{z = z_{max}}}{\left(\frac{\left.\frac{dM}{dz}\right|_{\substack{z = z_{max} \\ r = r_{max}}} + \left.\overline{\frac{dM}{dz}}\right|_{z = z_{max}}}{2}\right)} \times 100\% \qquad \textbf{(17)}$$

where z_{max} is the altitude of the maximum difference between refractive gradient and the range-mean refractive gradient of a forecast and r_{max} is the range at which the max difference occurs for $z = z_{max}$, and $\left.\overline{\frac{dM}{dz}}\right|_{z = z_{max}}$ is the mean *dM/dz* over range at $z = z_{max}$. The percent difference is used because there is no "reference" or "exact" value measured, which is required for percentage change or percentage error calculations, respectively. Thus, percent difference allows estimation of the magnitude of the amplitude of sinusoidal refractivity gradient variations in range for this set of data. The mean percent difference throughout all profiles is 25.3%, while the maximum and minimum percent differences are 85.59% and 1.23% respectively. This result indicates that the amplitudes are 25.3% larger or smaller than the average refractivity gradient for most forecasts examined. These percent differences are used to generate refractive gradient environments

which are sinusoidal in range that resemble behaviors seen in the data. Figure 30 shows refractivity gradients with respect to range and associated range-dependent modified refractivity profiles, which are used to examine the effects of these variations on propagation. The refractive gradient varies from the mean *dM/dz* over range for each altitude by 1.23%, 25.3%, and 85.59%. Figure 31 shows the propagation loss differences between simulated propagation using heterogeneous refractive environments illustrated in Figure 30, and coinciding homogeneous refractive environments using the refractive profile at r = 0 km. These results suggest that the amplitude of the sinusoidal variance of refractive gradients over range has non-negligible effects on the location of the multipath nulls in propagation patterns. The larger the amplitude, the larger the difference in the location of multipath nulls relative to a homogeneous environment. Other regions of the propagation domain vary less than 5 dB as a result of the amplitude changes. These results contrast those in Figure 27 (a, b) that show regions of localized propagation loss differences of ~-40 dB at low altitudes and long ranges associated with oscillatory variations in refractive gradients. Further examination of refractive environments (Figure 26 (a-d) and Figure 30 (a-f)) used to generate these propagation loss differences (Figure 27 (a, b) and Figure 31) reveals contrasting mean refractivity gradients over range and different initial phases of the oscillatory range-dependent refractive gradient variations. This comparison suggests that the mean and initial phase of the refractivity gradients over range likely produces effects on propagation loss in heterogeneous environments. These results are logical because the mean refractive gradients over range, along with the initial phase, change how the shape of the duct evolves through range. Many studies have shown that the shape of the modified refractivity profile is of importance to radar wave propagation

(Pastore et al., 2020; Lentini and Hackett, 2015; Babin and Dockery, 2002; Paulus, 1985), which suggests that any effects that vary the shape of the duct over range are likely to cause effects on radar wave propagation. Thus, even though variations in propagation loss are isolated to multipath null locations in Figure 31, variations at low altitude and long range are possible (consistent with that shown in Figure 27).

In order to investigate the typical initial phase of refractivity gradient oscillations, the range at which (maxima) amplitude of the oscillatory surface refractive gradient variations occurs is shown in Figure 32. For most profiles the peak *dM/dz* occurs nearest to shore (r = 0 km) or farther out at sea (r = 55-60 km). Large *dM/dz* near the shore could be due to the land-sea interface, while the large *dM/dz* offshore is likely associated with changes in sea surface temperatures caused by the Gulf Stream. However, because maximum amplitudes were observed at numerous ranges, the phase of the sinusoidal variation of refractive gradients over range should be considered variable.

In summary, refractivity gradients which are sinusoidal over range result in larger variations in propagation over larger areas than linear variations in range. Also, amplitudes of refractivity gradient oscillatory variations in range have non-negligible effects on propagation especially at the location of multipath nulls. Additionally, the mean refractivity gradients over range or the initial phase of refractivity gradient oscillatory variations in range could have non-negligible effects on propagation at low altitudes and long ranges. Furthermore, a majority (79%) of the refractive gradients investigated in this study are found to follow sinusoidal distributions in range although the phase of the sinusoidal distribution differs. Using this information, a sinusoidal function which considers

frequency, amplitude, and phase could accurately estimate the range distributions of refractivity gradients.

5.2 Range-Dependent Parametric Model

The previous section outlined refractivity characteristics that cause the greatest impact on propagation: (i) linear variations in duct height with respect to range as little as 1 m can cause non-negligible effects on propagation (Figure 17), (ii) sinusoidal variations of refractivity gradients in range cause greater effects on propagation than linear variations (Figure 27), (iii) all refractivity gradients below the duct height are negative and approach zero near the duct height (Figure 24a), and (iv) refractivity gradients above the duct height are positive and asymptote to similar values (Figure 24b). These results are used to develop a range-dependent parametric model for refractivity gradients, which can be integrated to produce modified refractivity using a range-dependent surface measurement of modified refractivity. Lastly, each function composed within the parametric model is evaluated using methods outlined in Section 4.4.

A one-way coupled set of equations is used to parameterize a heterogeneous refractivity gradient environment. This one-way coupled set of equations is henceforth referred to as the heterogeneous refractivity gradient model (HRGM) and is described below. Applying characterization result (i), a linear function is chosen to describe the variations of duct height with respect to range:

$$z_d(r) = \xi r + z_{d_0} \quad \textbf{(18)}$$

The duct height is parameterized using ξ, which is the rate of duct height change in range, and z_{d_0}, which is the duct height at r = 0 km. The duct height with respect to range

(Equation 18) is used in conjunction with a vertically layered set of functions to describe refractivity gradients over altitude and range:

$$\frac{dM}{dz}(r,z) = \begin{cases} m_1\,(1 - e^{-\kappa_2 z}), & z > z_d \\ 0, & z = z_d \\ \left.\frac{dM}{dz}\right|_{z=0} e^{\kappa_1 z} + \left.\frac{dM}{dz}\right|_{z=z_d - dz}, & 0 < z < z_d \\ a_1\ cos(2\pi(0.0158)r + \varphi) + a_2\ cos(2\pi(0.0316)r + \varphi) + a_3\ cos(2\pi(0.0474)r + \varphi) + \mu_{\frac{dM}{dz}}, & z = 0 \end{cases} \quad \textbf{(19)}$$

where a_1, a_2, and a_3 represent amplitudes of surface refractivity gradient oscillations for their respective wavenumber; $\mu_{\frac{dM}{dz}}$ is the mean refractivity gradient about which the gradients oscillate at the surface; φ is the initial phase of surface refractivity gradient variations; κ_1 and κ_2 are decay rates of refractivity gradients with height below and above the duct height, respectively; $\left.\frac{dM}{dz}\right|_{z = z_d - dz}$ describes the refractivity gradient just below the duct height; m_1 represents the mixed layer slope. The $\left.\frac{dM}{dz}\right|_{z = z_d - dz}$ term ensures that this function doesn't approach zero too quickly causing an underestimation of the duct height. Parameters $\left.\frac{dM}{dz}\right|_{z = z_d - dz}$,$\kappa_1$, κ_2, and m_1 are assumed to be homogeneous over range. These 11 parameters (ξ, z_{d_0}, a_1, a_2, a_3, $\mu_{\frac{dM}{dz}}$, φ, κ_1, $\left.\frac{dM}{dz}\right|_{z = z_d - dz}$, m_1, and κ_2) constitute the HRGM.

The lowest level of refractivity gradients (Equation 19, z=0 layer) are modeled based upon characterization result (ii) as well as other results outlined in Section 5.1.3. The function accounts for variable amplitude, phase, and mean surface refractivity gradients. The wavenumbers (0.0158 km^{-1}, 0.0316 km^{-1}, and 0.0474 km^{-1}) used to describe the surface refractivity gradients are based-on results from peak wavenumbers of surface refractive gradients for unstable conditions. The next level of the model (Equation 19, $0 < z < z_d$)

which consists of a decay function, is based on characterization result (iii). Refractivity gradients are set to zero at the duct height predicted from Equation 18. Based on characterization result (iv), a separate decay function (Equation 19, $z > z_d$ layer) is used to describe refractivity gradients above the duct height. A discrete representation of the HRGM (Equations 18 and 19), can be used to produce a discrete range-dependent modified refractivity environment using a surface measurement of modified refractivity over range ($M(r_i, z_0)$); akin to integrating Equation 19 over altitude:

$$M(r_i, z_{j+1}) = M(r_i, z_j) + \frac{dM}{dz}(r_i, z_j)\Delta z \qquad \textbf{(20)}$$

where *i=0,1,2,....* n_{x_r} is an index of discrete ranges where n_x is the total number of discrete ranges, and *j=0,1,2,....* $n_{x_z} - 1$ is an index of discrete altitudes, where n_{x_z} is the total number of discrete altitudes, and $\Delta z = z_{j+1} - z_j$. Equation 20 will be referred to as the integral form of the HRGM.

Since the HRGM is composed of multiple functions which describe separate layers of altitudes, each layer is scrutinized by comparing the data to that layer's model using parameters estimated from least-squares regressions. This analysis allows understanding of which functions within the HRGM could be improved to produce more accurate measurements.

Linear-least-squares regression using Equation 18 to estimate duct heights is applied for all forecasts, including those which exhibited non-linear behavior. Duct heights from fits of these regressions are compared to duct heights in the forecasts via RMSE or α_{z_d} (Equation 11 for duct height). Figure 33 illustrates that α_{z_d} is frequently less than 0.5 meter indicating that, in some cases, forecasts that exhibited sinusoidal or step-like

behavior could be accurately estimated by a linear function that describes duct height in range.

In the development of the function representing the z=0 layer of the HRGM (Equation 19), two oscillatory functions were evaluated. The first was a basic cosine model:

$$\frac{dM}{dz}(r) = a\ cos(2\pi k_{\frac{dM}{dz}} r + \varphi) + \mu_{\frac{dM}{dz}} \qquad \textbf{(21)}$$

where a is the amplitude of the refractivity gradient variation, and $k_{\frac{dM}{dz}}$ is the wavenumber of the refractivity gradient variations. These variables are fit in non-linear least squares regressions. The second function evaluated is that shown in Equation 19 for the z=0 layer. The primary distinction between the two models is that Equation 21 allows for the dominant wavenumber to be fit while the other model in Equation 19 fixes the wavenumbers but incorporates more than one wavenumber. RMSEs ($\alpha_{\frac{dM}{dz}|_{z=0}}$) between surface refractivity gradient models, and the refractivity gradient from the data are calculated and shown in Figure 34. The basic cosine function (Equation 21, Figure 34a) has an RMSE standard deviation of 13.87 M-units/m, an average RMSE of 9.39 M-units/m, a maximum RMSE of 109.74 M-units/m, and a minimum RMSE of 0.53 M-units/m; while the model used in the z=0 layer of the HRGM (Equation 19, Figure 34b) has an RMSE standard deviation of 7.09 M-units/m, an average RMSE of 8.41 M-units/m, a maximum RMSE of 55.12 M-units/m, and a minimum RMSE of 0.77 M-units/m. Although the cosine model RMSEs (Equation 21) have a slightly increased frequency of the most accurate refractivity gradients (Figure 34), it has larger RMSE standard deviation, RMSE average, and RMSE maximum and minimum. These facts suggest that the function used in the

HRGM (Equation 19) is more accurate in representing variations of surface refractive gradients with respect to range. Furthermore, Equation 19 seems to produce more stable and accurate estimations than the basic cosine function (Equation 21). The primary shortcoming of the basic cosine model appears to be related to inaccuracies in predicting the wavenumber ($k_{\frac{dM}{dz}}$). However, the basic cosine function did show some merit in many situations, suggesting that other sinusoidal functions besides the one used in the HRGM could be used to predict surface refractivity gradients.

Nonlinear least squares regression is applied to all refractive gradient profiles with respect to height below the duct height at each range for all COAMPS®-NAVSLaM blended data to estimate the vertical decay rate (κ_1) and the refractivity gradient just below the duct height ($\frac{dM}{dz}\Big|z = z_d - dz$) at each range over all datasets (see Equation 19). RMSEs ($\alpha_{\frac{dM}{dz}\Big|_{z<z_d}}$) between estimates of refractivity gradient produced by the HRGM in model layer $0<z<z_d$ and refractivity gradients in the blended data set are calculated for all forecasts. Since refractivity gradients vary by as much as 2 orders of magnitude, RMSEs are normalized by the mean refractive gradient over range, referred to as percent error or *E* (see Equation 12), which is shown in Figure 35. These results show that the RMSEs are most frequently between 40-50% of the mean refractivity gradients with RMSEs ranging from less than 10% up to 70% of the mean refractivity gradient. This fact suggests that this layer of the HRGM may not be well-suited for all environmental cases but could be useful in some. Future research could investigate ways to improve this layer of the HRGM.

Nonlinear least squares regression is applied to all refractive gradient profiles with respect to height at each range in all COAMPS®-NAVSLaM blended data above the duct

height to estimate the vertical decay rate (κ_2) and the mixed layer slope (m_1) for evaluating the $z>z_d$ layer of the HRGM. Figure 36 shows RMSEs between refractivity gradient ($\alpha_{\frac{dM}{dz}\Big|_{z>z_d}}$) of each forecast and those estimated using the HRGM model layer $z>z_d$ (Equation 19) over range. These results suggest that the HRGM model is an accurate representation of refractivity gradients above the duct height with E < 10% for the vast majority of the datasets, implying that errors are typically less than 10% of the mean refractivity gradients above the duct height.

5.3 Range-Dependent Parametric Refractivity Gradient Model Evaluation and Discussion

To test the HRGM (Equations 18 and 19) for accuracy in terms of modified refractivity as well as propagation predictions, it is used to estimate refractivity gradients using the least squares fit of each parameter for each COAMPS®-NAVSLaM blended forecast. Each estimated refractivity gradient domain is transitioned to modified refractivity using the integral form of the HRGM (Equation 20), and the surface modified refractivity estimations from the corresponding COAMPS®-NAVSLaM blended forecasts as the boundary condition at $M(r_i, z_0)$. Figure 37 illustrates an example $M(r,z)$ environment produced using the integral form of the HRGM and the corresponding COAMPS®-NAVSLaM blended forecast. It should be noted that M profiles produced by the HRGM have a "kink" or "elbow" shape at the duct height which could cause discrepancies in PL estimates. Estimates of $M(r,z)$ are used to simulate propagation via VTRPE. Both the resulting modified refractivity ($M(r,z)$) and the resulting propagation patterns are compared to those from COAMPS®-NAVSLaM blended data using methods outlined in section 4.5.

RMSEs of modified refractivity (see section 4.5) are calculated for the entire domain (i.e., over range and altitude) for each forecast and are illustrated in Figure 38. The mean and median of these RMSEs are 3.01 and 2.42 M-units respectively, which illustrates that on average the HRGM is able to accurately model modified refractivity of the COAMPS®-NAVSLaM blended data. The minimum RMSE is 0.32 M-units, while the maximum is 18.66 M-units, which suggests that this model performs better in some environmental cases than in others. Although no correlation seems to be evident between RMSEs of modified refractivity and stability ($\overline{Ri}$), it should be noted that Figure 38 illustrates time periods where RMSEs increase as compared to the overall trend (e.g., between forecasts 200 and 300), and decrease compared to the overall trend (e.g., between forecast 350 and 450). Wang et. al (2018) reported that synoptic fronts passed through the study area on October 18th, 19th, 23rd, 26th, and 28th, which coincide with forecasts 200 – 300 on Figure 38, indicating that the HRGM has greater error during these times of the synoptic frontal events. Also, after inspection of visual and infrared satellite imagery maintained by the Mesoscale and Microscale Meteorology Division of the National Center of Atmospheric Research (NCAR; Ahijevych, 2020) during the times of the CASPER-East field experiment, it is shown that the region was rather cloudy between November 1st and November 4th, which coincides with forecasts 350-450. This fact may suggest that the integral form of the HRGM has less error when conditions are cloudy; but of course, this result could also be related to other environmental effects. Histograms of all residuals and RMSEs calculated for this data set are shown in Figure 39. Residuals most frequently occur between ±5 M-units with more positive residuals than negative residuals while RMSEs are typically 1-3 M-units. These results further suggest that the model performs well in a

majority of cases, but not in all, and more frequently overestimates modified refractivity than underestimates it.

In order to identify where in altitude and range the modified refractivity estimates using the parametric model perform best, the mean residual ($\beta_M(r,z)$), which is the forecast-averaged residual between each HRGM-estimated forecast and its corresponding COAMPS®-NAVSLaM blended forecast, is shown in Figure 40. These results show that the mean residual is typically between ±3 M-units, which is on par with the average RMSEs mentioned previously. Also, these results illustrate that the modified refractivity is typically underestimated beneath the average duct height (~9.5 m), and overestimated above the mean duct height. Although the changes in mean residual are larger over altitude, there are also variations over range. *M(r,z)* is estimated more accurately by the integral form of the HRGM above the average duct height in the short range (0-30 km) than in the long range (30-60 km), while estimates below the average duct height are more accurate in the long range (30-60 km), and less accurate in the short range (0-30 km). There are also discontinuities of $\beta_M(r,z)$ between r = 0 km and r = 2.04 km, which could be related to the location of the maximum amplitude of surface *dM/dz* illustrated previously in Figure 32 that frequently occurs near Duck pier most likely due to the land/ocean interface.

There are many cases such as those illustrated in Figure 41, where modified refractivity is estimated accurately (~1 M-unit) (Figure 41(a-b)) throughout the domain and some cases where modified refractivity is estimated poorly (Figure 41(c-d)). The well-estimated modified refractivity environments (Figure 41(a-b)) show similar distributions of $\beta_M(r,z)$, where estimations below the duct height seem to be the most accurate region in the entire domain (~0 M-units), while just above the duct height seems to show the most

discrepancies throughout the entire domain (~2 M-units). The poorly-estimated modified refractivity environments (Figure 41 (c-d)) show a basic similar shape of distributions of $\beta_M(r,z)$, with Figure 41d showing greater residual magnitudes. In both subfigures (Figure 41c-d), there is an overestimation of modified refractivity at low-to-mid-altitudes (10-40 m) and close ranges (0-30 km), where the estimation within those altitudes improves at the long ranges (40-60 km). This region of overestimation is likely associated with the HRGM's parameters: $\frac{dM}{dz}\Big|_{z = z_d - dz}$, κ_1, and/or κ_2, which are all assumed to be constant with range. These results may suggest that COAMPS®-NAVSLaM blended environments show many examples where these parameters vary in range, and in some cases, this causes a breakdown of estimating modified refractivity using the HRGM. Further research should investigate the effects of range-varying $\frac{dM}{dz}\Big|_{z = z_d - dz}$, κ_1, and κ_2 on modified refractivity and propagation. Along with areas of overestimation, there seem to be areas of underestimation in both subfigures (Figure 41c-d) at high altitudes (50-100 m) and all ranges. These regions of underestimation could be related to the assumption made in the HRGM that m_1 is constant with respect to range, indicating that the COAMPS®-NAVSLaM blended environments sometimes show a shifting mixed layer slope with range, which the HRGM cannot accurately reproduce.

To understand why the HRGM estimates refractivity poorly in some cases and accurately in others, RMSEs of refractivity gradients and duct heights are correlated to RMSEs of modified refractivity (α_M) throughout the entire domain. Table 2 illustrates correlation coefficients (Equation 10) for each layer that comprises the HRGM along with their associated significance values (p-values). Correlated estimated model parameters

include RMSEs of duct height with respect to range (α_{z_d}), and RMSEs of refractivity gradients at the surface ($\alpha_{\frac{dM}{dz}|_{z=0}}$), below the duct height ($\alpha_{\frac{dM}{dz}|_{z<z_d}}$), and above the duct height ($\alpha_{\frac{dM}{dz}|_{z>z_d}}$). Significance is determined by p-values that are less than 0.05. Each correlated variable illustrated in Table 2 significantly correlates with α_M, although strongest correlations, by far, are with $\alpha_{\frac{dM}{dz}|_{z=0}}$, indicating that $\alpha_{\frac{dM}{dz}|_{z=0}}$ has the strongest direct relationship to the error of modified refractivity in the entire domain (α_M); thus, in some cases, the sinusoidal model used to describe the surface refractive gradient is sub-optimal. Figure 34b illustrates that there are occurrences where the functional form that describes surface refractivity gradients within the HRGM performs poorly. Additionally, Figure 34a illustrates that other sinusoidal functions besides the one used in the HRGM show promise at predicting surface refractivity gradients. Further research could investigate other functional forms which could improve the estimates of surface refractive gradients or determine if certain sinusoidal functions perform better under specific atmospheric conditions. Table 2 also illustrates a weak direct correlation between modified refractivity α_M and α_{z_d}, indicating that inaccuracies in the linear model used to estimate duct heights in the HRGM can relate to uncertainties in modified refractivity. The lower correlation coefficient suggests that it is less likely for errors in modified refractivity to occur based on duct height estimation, than within the sinusoidal model used to estimate surface refractive gradients (Figure 34b). Furthermore, correlation coefficients in Table 2 illustrate weak inverse relationships between α_M and $\alpha_{\frac{dM}{dz}|_{z<z_d}}$ as well as α_M and $\alpha_{\frac{dM}{dz}|_{z<z_d}}$. These inverse relationships suggest that, on occasion, when the decay functions within the HRGM that are used to estimate refractivity gradients above or below the duct height

perform poorly (Figures 35 and 36), the modified refractivity throughout the entire domain can still be accurately estimated. One interpretation of this result would be that when the decay functions produce inaccurate results, other layers within the HRGM are frequently more accurate than average enabling modified refractivity throughout the entire domain to be estimated more accurately.

In order to evaluate the HRGM's accuracy at predicting propagation, PL RMSE (α_{PL}), and residuals (β_{PL}) (see Section 4.5) are calculated for each forecast. The mean and median α_{PL} are 10.64 dB and 9.46 dB, respectfully. The minimum α_{PL} is 3.45 dB, while the maximum is as high as 100 dB. Similar to the results for modified refractivity, these statistics suggest that the HRGM results in propagation estimates that are better in some environments than others. Figure 42 shows histograms of the residuals and RMSEs of estimated propagation loss. The residuals show a near Gaussian distribution about 0 dB, which indicates that on-average residuals are small and there is no bias. The RMSEs show that typically the model predicts propagation within 5-10 dB of the associated propagation simulated using the COAMPS®-NAVSLaM blended forecast. It should be noted, however, that RMSEs are more frequently above 5 dB than below. This higher RMSE may be due to inaccurate placement of the multipath nulls, which could cause large variances of the PL. Figure 43 shows RMSEs calculated (see Section 4.5) throughout the entire domain for each forecast. The RMSEs shown are filtered using a 5 forecast running average filter in order to reduce small scale variability in the time series. Although no correlation between α_{PL} and stability ($\overline{Ri}$) is evident, there are time periods where PL RMSEs seem to increase relative to the mean (e.g. forecasts 320-420) and time periods where PL RMSE variability is small (e.g. forecasts 200-300). The time periods where PL RMSEs are large coincide

with previously discussed cloudy conditions identified via visible satellite imagery (Ahijevych, 2020). This fact could suggest that cloudy conditions, although they may make it easier to predict the modified refractivity, the improved modified refractivity does not result in improved PL predictions. However, time periods where the variability of the PL RMSEs are small are associated with the previously discussed synoptic frontal events identified by Wang et al. (2018). This result suggests that the synoptic front events result in smaller variation of estimations of propagation when using the HRGM even though the refractivity comparisons were worse during this period. This result may suggest decreased sensitivity of PL to the refractivity variations that are not captured by the HRGM during these times.

In order to identify where in altitude and range the propagation estimates using the parametric model perform best, the mean residual ($\beta_{PL}(r,z)$), which is the forecast-averaged residual between PL based-on each HRGM-estimated forecast and PL based-on the corresponding COAMPS®-NAVSLaM blended forecast, is illustrated in Figure 44. These results suggest that discrepancies within the propagation often occur at the locations of the multipath nulls, and above typical duct heights at long range (r = 30-60 km). A sensitivity study by Lentini and Hackett (2015) shows that the duct height is the most influential parameter close to the transmitter (within a range of 10 km), while propagation at long range is more sensitive to duct shape. Applying these results suggest that since the region of inaccurate estimation of multipath nulls is near the transmitter and within 10 km, it is likely that discrepancies in the duct heights are leading to differences in the location of the multipath nulls. Furthermore, since propagation at long range is more sensitive to duct shape, it is likely that differences in the shape of the duct are leading to discrepancies

at the long range, mid altitude region. Although discrepancies between model-predicted propagation and that using COAMPS®-NAVSLaM blended data exist, the magnitude of the mean residuals are rather small, especially outside of the location of the multipath nulls. It should be noted, however, that these results are averages and there are many cases that the model performs better and worse than the average.

Figure 45 illustrates some cases where propagation is estimated accurately (< ~9 dB) throughout the entire domain (Figure 45(a-b)) and some cases where propagation is estimated poorly (Figure 45(c-d)). The well-estimated PL environments (Figure 45(a-b)) show similar distributions of $\beta_{PL}(r,z)$, where the most dramatic changes seen within the domain lie at the location of the multipath nulls. On the other hand, the poorly-estimated PL environments (Figure 45(c-d)) also show similar distributions of $\beta_{PL}(r,z)$ to each other. In these cases, the locations of the multipath nulls show higher $\beta_{PL}(r,z)$ relative to those cases illustrated in Figure 45(a-b). Also, in contrast to Figure 45(a-b), residuals of PL are greater at low altitudes and long ranges. Although the low altitude long range region illustrated inaccurate predictions from the HRGM in these cases, there were other cases where the HRGM accurately predicted propagation in this region in order to produce the average results shown in Figure 44.

To understand why the parametric model estimates propagation poorly in some cases and accurately in others, RMSEs of refractivity gradients and duct heights are correlated to RMSEs of propagation loss over the entire domain. Table 3 illustrates correlation coefficients calculated between α_{PL}, and α_M or the RMSEs (α_x) of duct height and refractivity gradients of each layer that comprises the HRGM (i.e., α_{z_d}, $\alpha_{\frac{dM}{dz}\Big|_{z>z_d}}$,

$\alpha_{\frac{dM}{dz}\Big|_{z<z_d}}$, $\alpha_{\frac{dM}{dz}\Big|_{z=0}}$). Two variables show significant relationships to α_{PL}, namely $\alpha_{\frac{dM}{dz}\Big|_{z>z_d}}$ and α_{z_d}. The most direct relationship shown is between α_{PL} and α_{z_d} suggesting that the duct height variations are the dominant component which is linearly linked to variations in propagation. These results align with many past studies (Kerr, 1951; Turton et al., 1988; Anderson, 1989; Hitney and Hitney, 1990; Paulus, 1990; Lentini and Hackett, 2015), which show that propagation loss is sensitive to duct height. In section 5.1, it is shown that duct heights vary linearly, oscillatory, and step-wise over the range of data investigated in this study. Although most cases fit a linear trend, it was also shown that sinusoidal variances of duct height in range produce rather different propagation patterns than linear variances. Thus, in some situations, it may be necessary to model duct height with respect to range using a sinusoidal function similar to that used to model surface refractivity gradients with respect to range in Equation 19 to further improve duct height estimates and consequently propagation predictions. Future *in-situ* studies should investigate the presence of step function distributions of duct height in range to evaluate whether it is a COAMPS® artifact or a natural phenomenon. Table 3 also shows a significant weak direct relationship between $\alpha_{\frac{dM}{dz}\Big|_{z>z_d}}$ and α_{PL}, which is likely related to the majority of the domain being above the duct height and the α_{PL} metric being evaluated over the entire domain. Large α_{PL} could be associated with slight shifts in locations of multipath nulls, so in order to eliminate this effect, α_{PL} is calculated only within the long range (<45 km) region and the same correlation coefficients calculated in Table 3 are illustrated in Table 4. The correlation coefficients between α_M and α_{PL} in both Tables 3 and 4 indicate a lack of a linear relationship between these two variables. This result suggests that errors in modified

refractivity estimation can't be used to directly infer errors on propagation. Instead, errors in duct height and refractive gradients should be used to directly infer errors in PL. Table 4 shows differing results than those shown in Table 3 where $\alpha_{\frac{dM}{dz}\Big|_{z>z_d}}$ shows a stronger correlation to α_{PL} in the long range region than does α_{z_d}, and $\alpha_{\frac{dM}{dz}\Big|_{z<z_d}}$ is shown to have a significant correlation to α_{PL}. This result is consistent with the aforementioned results presented by Lentini and Hackett (2015), which stated that duct height is more influential on PL in the short range while duct shape is more influential in the long range. This result confirms previous remarks that errors in the estimation of PL in the long range region are driven by HRGM errors in the refractivity gradients above the surface more so than the estimate of the duct height itself. The inaccuracies are likely due to underlying assumptions made by the HRGM that $\frac{dM}{dz}\Big|_{z = z_d - dz}$, κ_1, κ_2, and m_1 are constant. Thus, future studies of heterogeneous refractive models should consider a range-varying $\frac{dM}{dz}\Big|_{z = z_d - dz}$, κ_1, κ_2, and m_1 in order to more accurately predict PL at long ranges. The previously described correlation between $\alpha_{PL}$and α_{z_d}along with the lack of correlation between duct height RMSE and PL RMSE at long range suggests that inaccurate duct heights mainly impact the location of multipath nulls and short range low altitude propagation.

In summary, on-average, the range-dependent parametric refractivity gradient model proposed in this study produces accurate estimations of modified refractivity and propagation loss. RMSEs of modified refractivity are greater during synoptic fronts and lower during cloudy conditions. When modified refractivity RMSEs are large, the HRGM tends to underestimate modified refractivity beneath the duct height, and overestimates it

above the duct height. The leading cause of discrepancies in the modified refractivity estimation is the sinusoidal function used to describe the surface refractive gradients. RMSEs of PL using the HRGM become greater in cloudy environments and decrease in variability (relative to the mean PL RMSE) during synoptic front events. When discrepancies in PL occur, they are typically located at the locations of multipath nulls and above typical duct heights in the long range region. Foremost, the leading cause of error in the propagation estimation by the HRGM in the entire domain is the model's predictive accuracy regarding duct height variations with respect to range, which also have a significant effect on the location of multipath nulls. PL discrepancies in the long range region appear to be mostly associated with errors in the refractivity gradients above the surface. Thus, in order to accurately predict propagation in horizontally heterogeneous environments throughout a large domain, the behavior of the duct height and refractivity gradients over range need to be modeled accurately in order to obtain accurate propagation in the short and long ranges, respectively, and should be the foremost concern of future heterogeneous parametric models used to solve radar inversion problems.

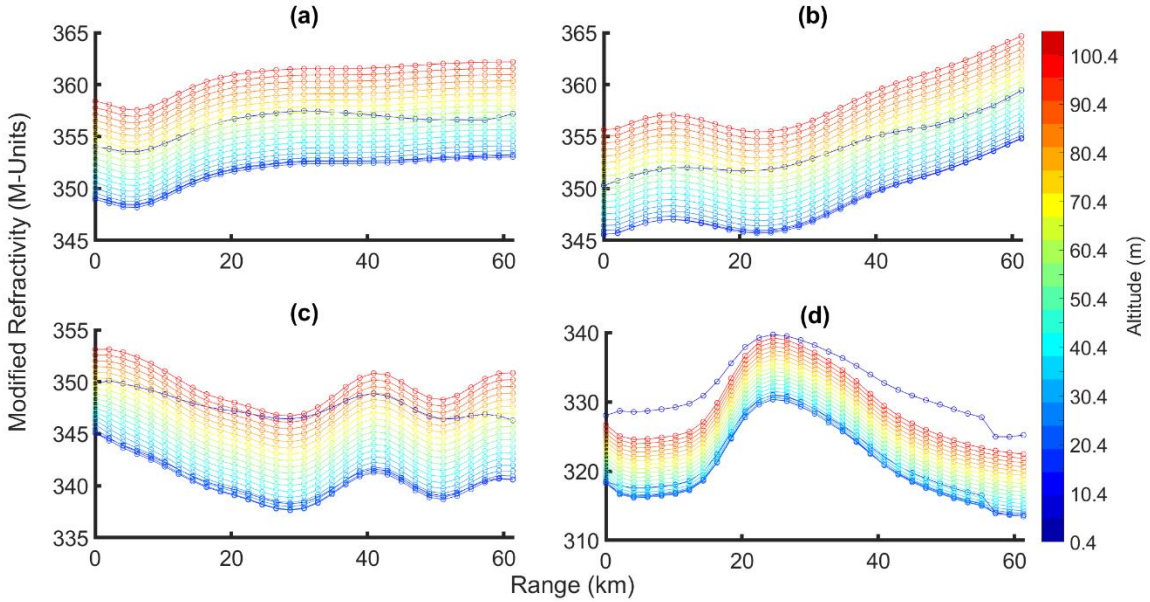

Figure 13. Modified refractivity with respect to range from four arbitrarily chosen environments taken from COAMPS®-NAVSLaM blended profiles. (a) shows COAMPS®-NAVSLaM data from forecast for October 11, 2015 model run 12:00Z forecast hour 9, (b) shows COAMPS®-NAVSLaM data from forecast for October 12, 2015 model run 00:00Z forecast hour 10, (c) shows COAMPS®-NAVSLaM blended data from forecast for October 14, 2015 model run 12:00Z forecast hour 11, and (d) shows COAMPS®-NAVSLaM blended data from forecast for October 19, 2015 model run 00:00Z forecast hour 6. Most variations of modified refractivity in range have an oscillatory distribution.

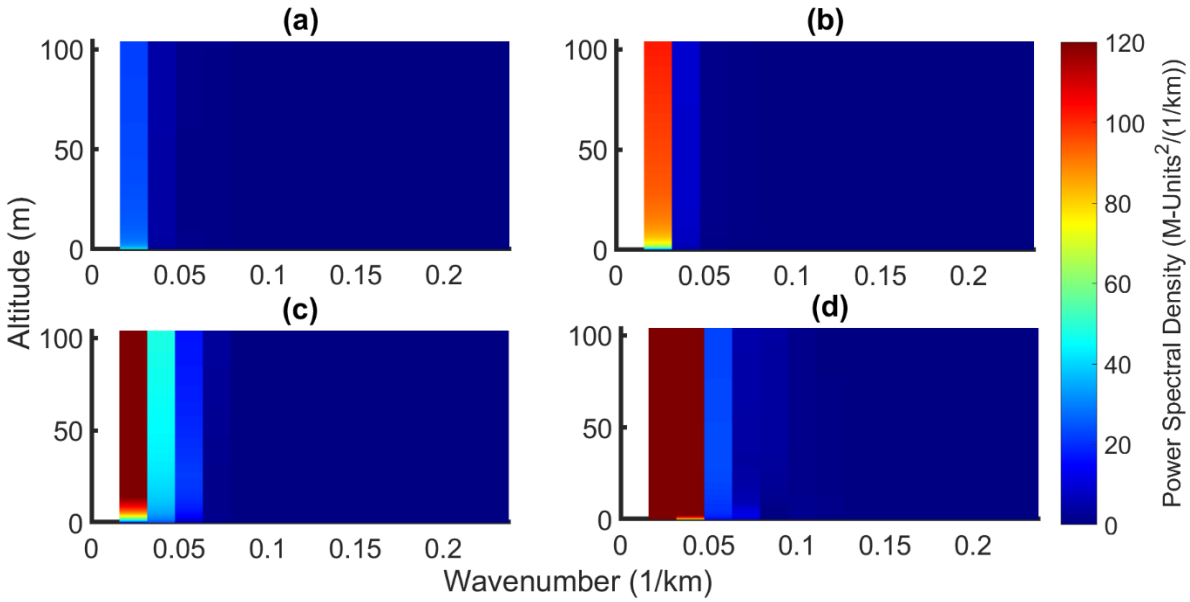

Figure 14. Spectrograms showing power spectral densities (PSDs) of modified refractivity over range for each altitude shown in Figure 13, respectively.

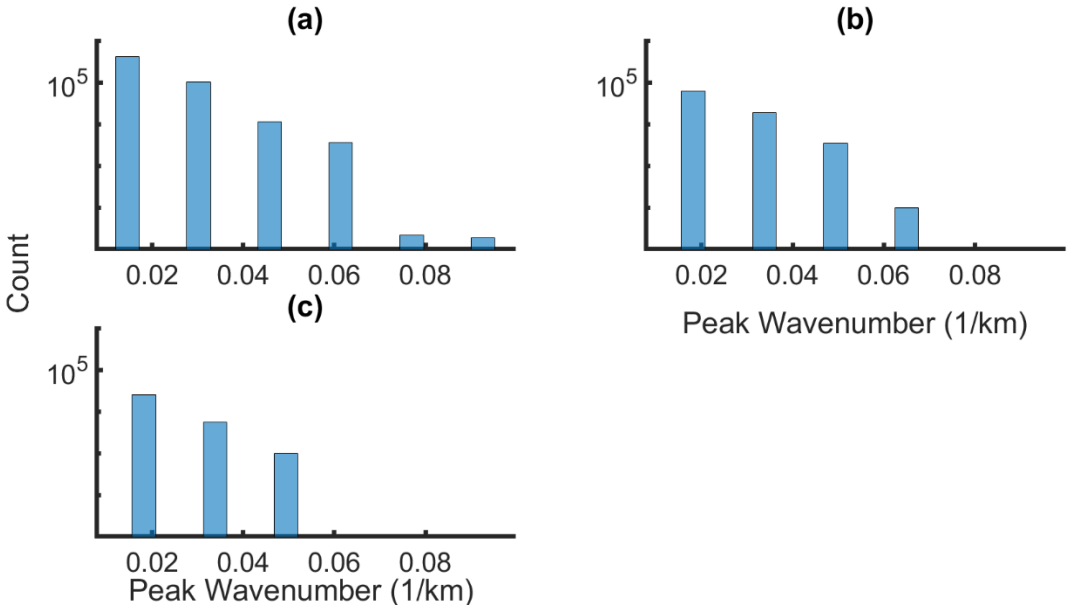

Figure 15. Histograms of peak wavenumbers (e.g., Figure 14) for various atmospheric stability conditions: a) unstable, b) stable, and c) free convective conditions (see Section 4.3 for descriptions of stability classifications).

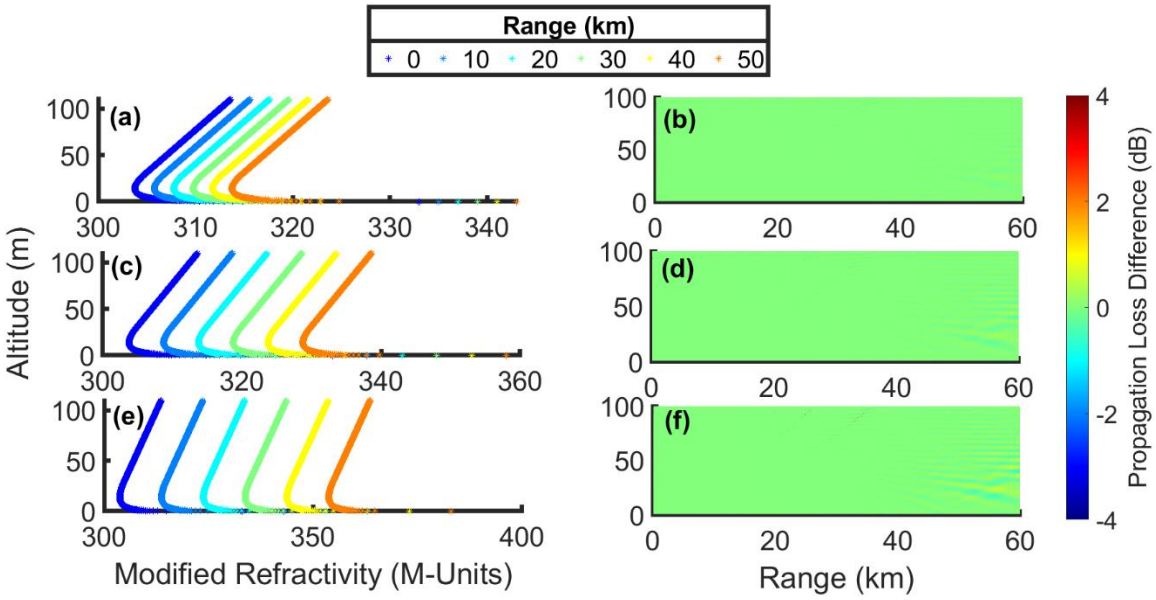

Figure 16. Modified refractivity profiles of environments whose surface modified refractivity increases in range (left) and the differences between propagation loss produced using the varying environments shown and those propagation loss patterns produced by using the modified refractivity profile at the first range (range = 0km) and assuming horizontal homogeneity (right). (a) shows an environment where surface modified refractivity increases by 2 M-units every 10 kilometers over a range of 60 kilometers, and (b) shows the resulting propagation loss difference. (c) shows an environment where surface modified refractivity increases by 5 M-units every 10 kilometers over a range of 60 kilometers, and (d) shows the resulting propagation difference. (e) shows an environment where surface modified refractivity increases by 10 M-units every 10 kilometers over a range of 60 kilometers, and (f) shows the resulting propagation difference.

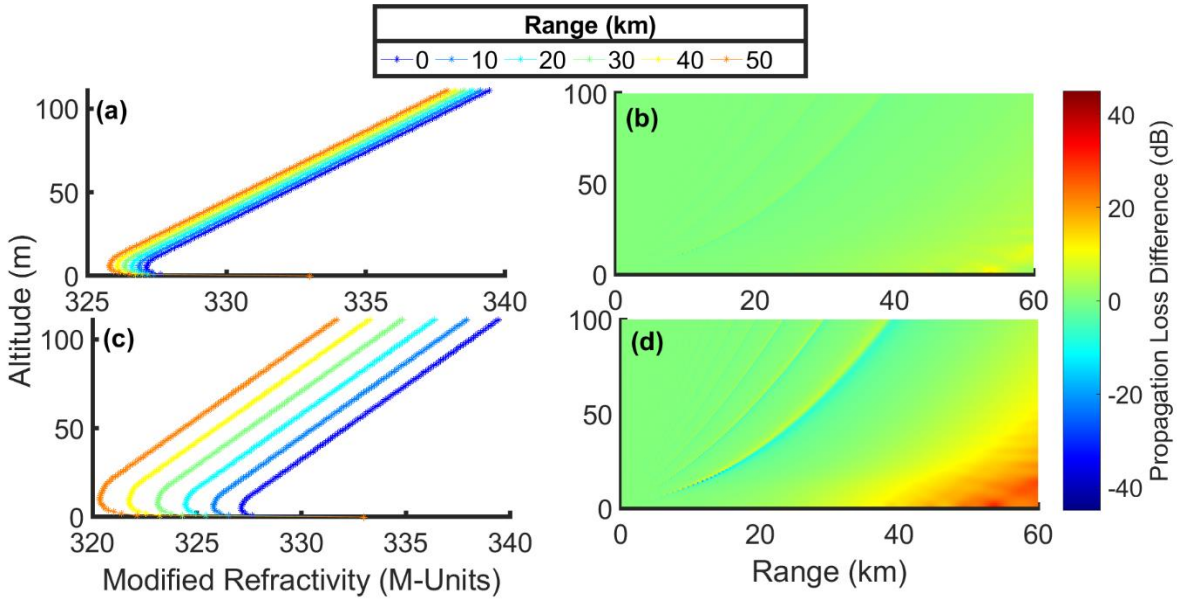

Figure 17. Modified refractivity profiles of environments whose duct heights vary linearly in range (left) and the differences between propagation loss produced using the environments shown, and those propagation loss patterns using the modified refractivity profile at the closest range (range = 0 km) and assuming horizontal homogeneity (right). (a) shows an environment where duct height linearly varies by 1 m over 60 km range, and (b) shows the resulting propagation loss difference. (c) shows an environment where duct height linearly varies by 5 m over 60 km range, and (d) shows the resulting propagation loss difference.

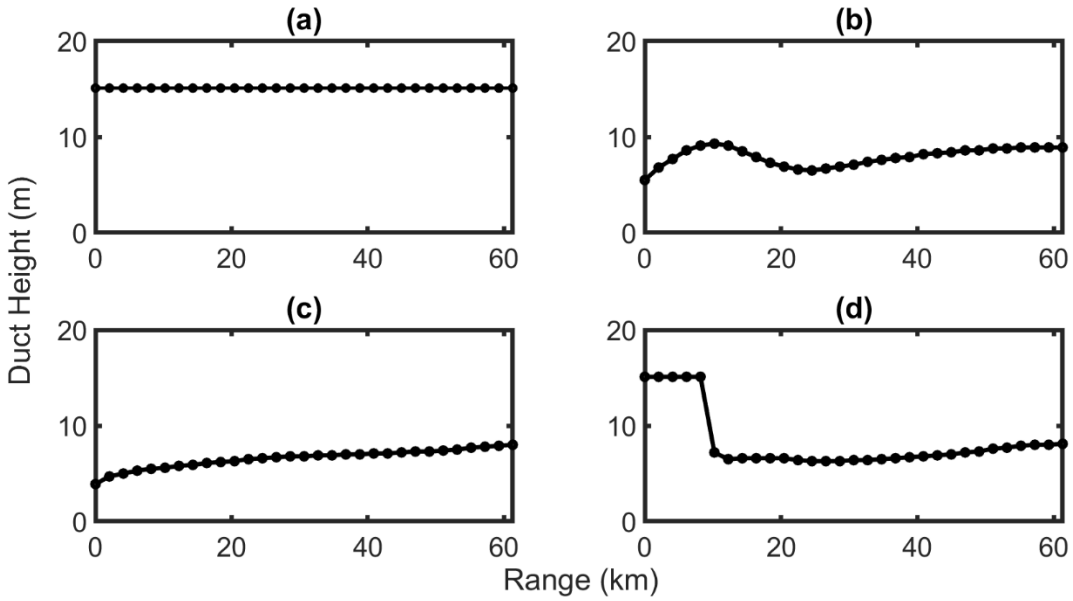

Figure 18. Examples of different functional forms of variations of duct height with respect to range. All data are from COAMPS®-NAVSLaM blended forecasts. (a) Exemplifies a constant distribution and comes from a forecast taken for October 18, 2015 using model run 00:00Z forecast hour 5. (b) Exemplifies an oscillatory distribution and comes from a forecast taken for October 10, 2015 using model run 00:00Z forecast hour 6. (c) Exemplifies a linear distribution and comes from a forecast taken October 23, 2015 using model run 00:00Z forecast hour 9. (d) Exemplifies a step distribution and comes from a forecast taken for October 23, 2015 using model run 12:00Z forecast hour 10.

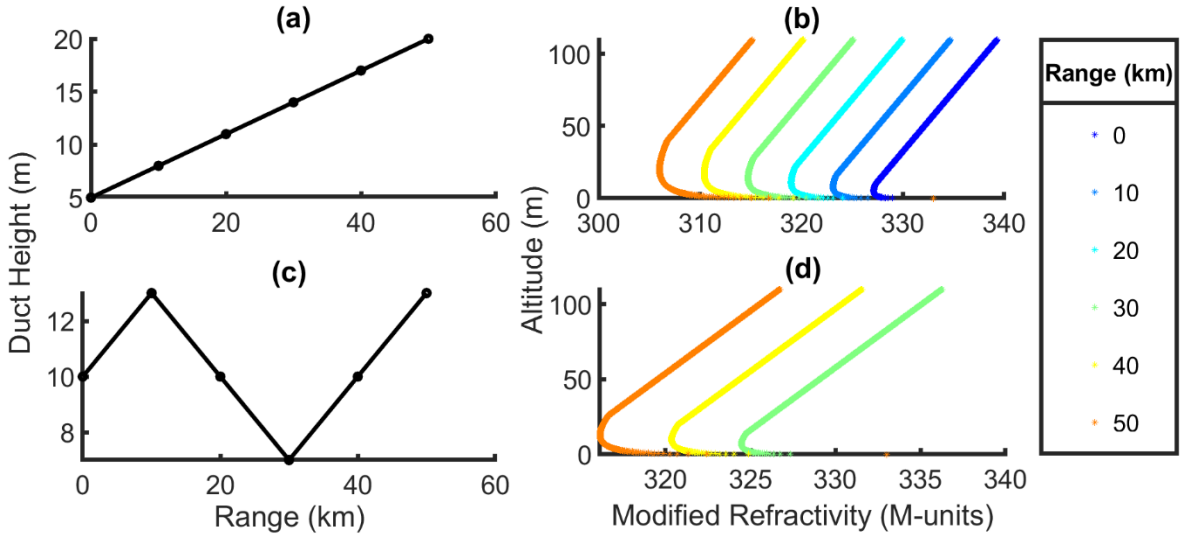

Figure 19. Duct height distributions with respect to range (left) and the corresponding modified refractivity profiles over range (see legend) (right).

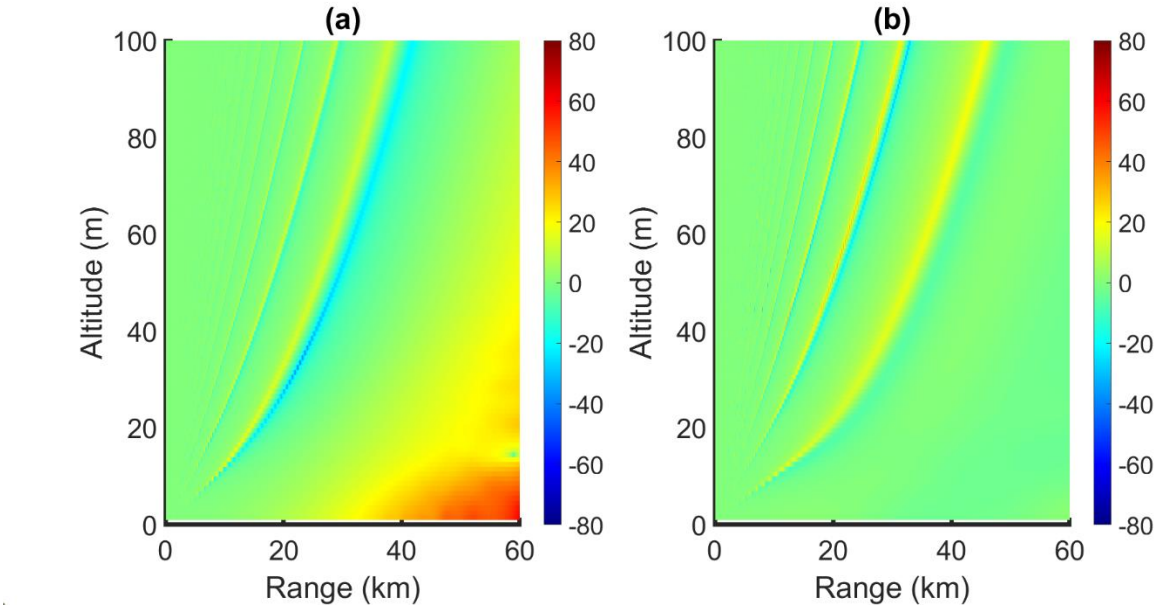

Figure 20. Differences between propagation loss produced using environments shown in Figure 19a and 19b for (a), and Figure 19c and 19d for (b) and those propagation loss patterns produced by using the corresponding modified refractivity profile at the first range (range = 0 km) and assuming horizontal homogeneity.

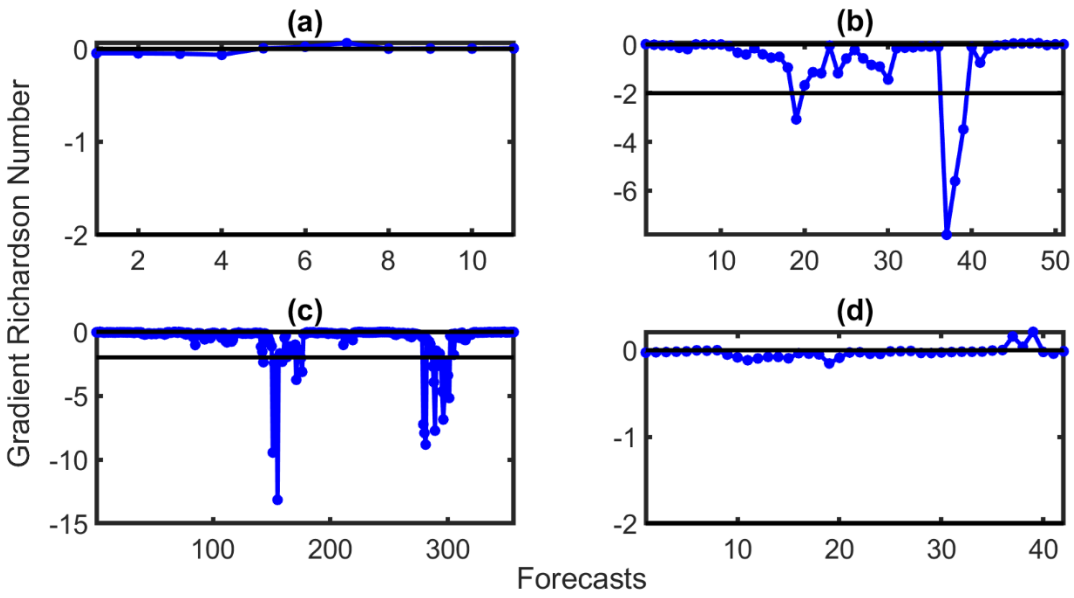

Figure 21. Gradient Richardson number ($\overline{Ri}$) for each forecast classified by functional form of duct height variations in range: flat (a), sinusoidal (b), linear (c), and step (d) functional forms. The horizontal black lines in each subplot show important stability categorization cutoffs. The horizontal black line in (a) and (d) show where $\overline{Ri}$ = 0 which illustrates where forecasts go from stable to unstable, while the horizontal black lines in (b) and (c) show where $\overline{Ri}$ = -2 which illustrates where forecasts go from unstable to free convective.

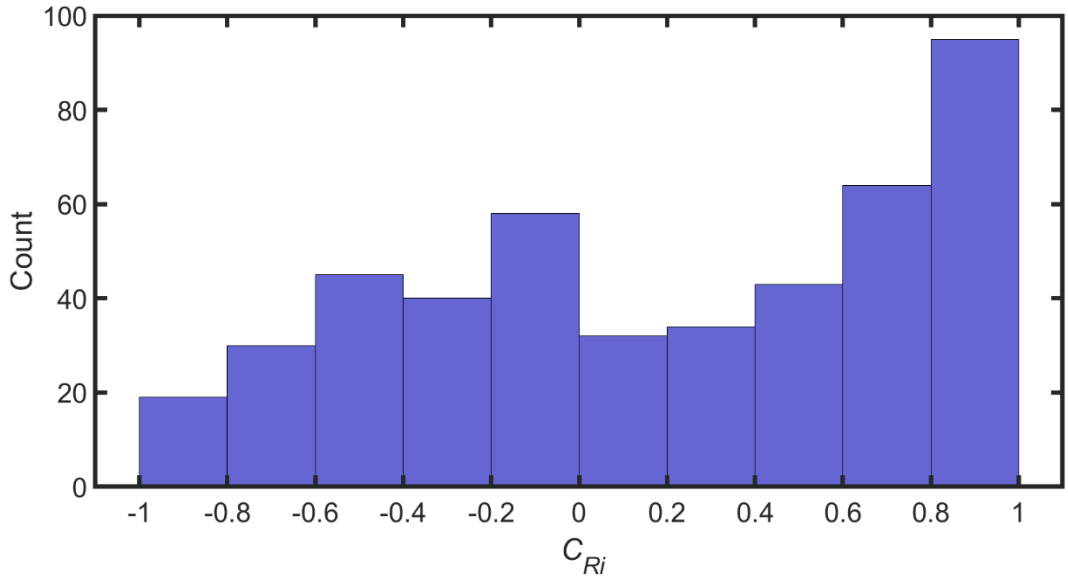

Figure 22. Histogram of the correlation coefficients between the gradient Richardson number ($\overline{Ri}(r)$) and duct height as a function of range.

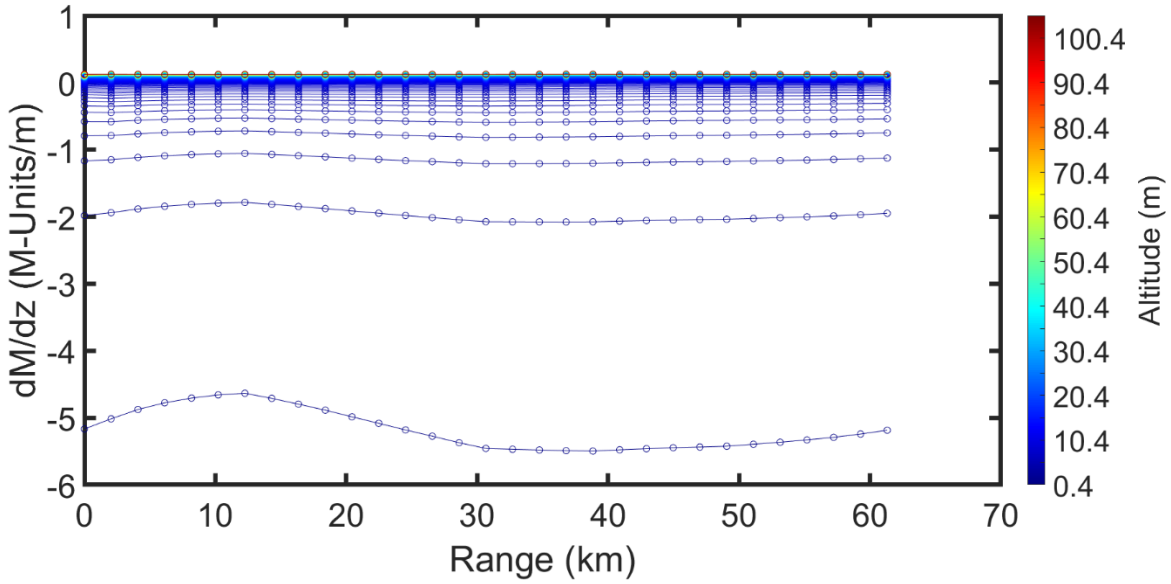

Figure 23. *dM/dz* with respect to range and height of a COAMPS®-NAVSLaM blended forecast for October 10, 2015 model run 00:00Z forecast hour 11. Although the blended data have decimeter vertical resolution, for visualization purposes, only estimations every 0.5 meter are shown starting at 0.4 meters in altitude.

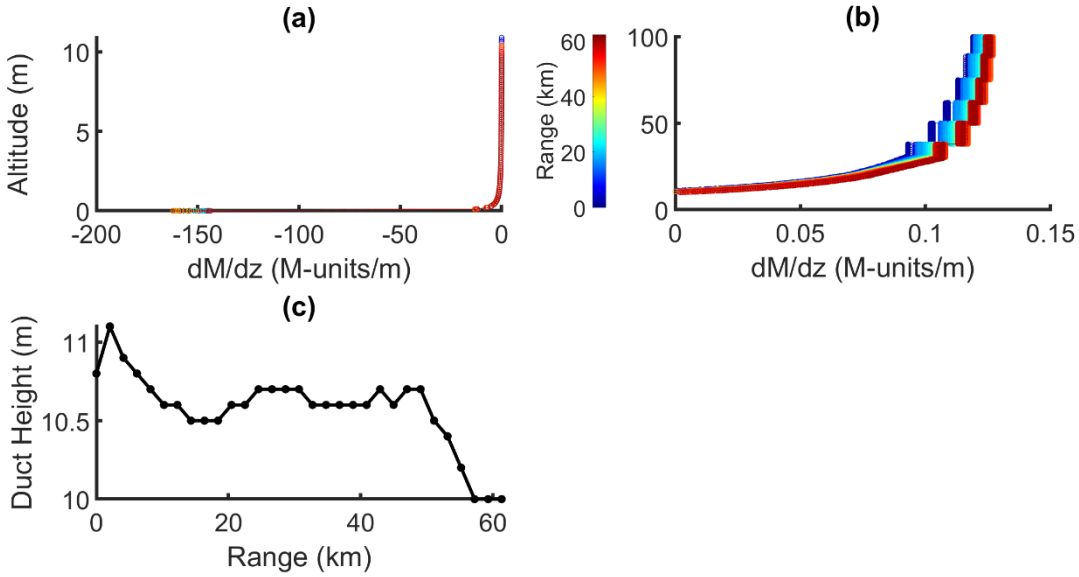

Figure 24. Examples of refractivity gradients with respect to altitude at each range below the duct height (a), and above duct height (b), where duct height varies with range as shown in (c). Data shown is from an October 26, 2015 00:00Z model run at forecast hour 6.

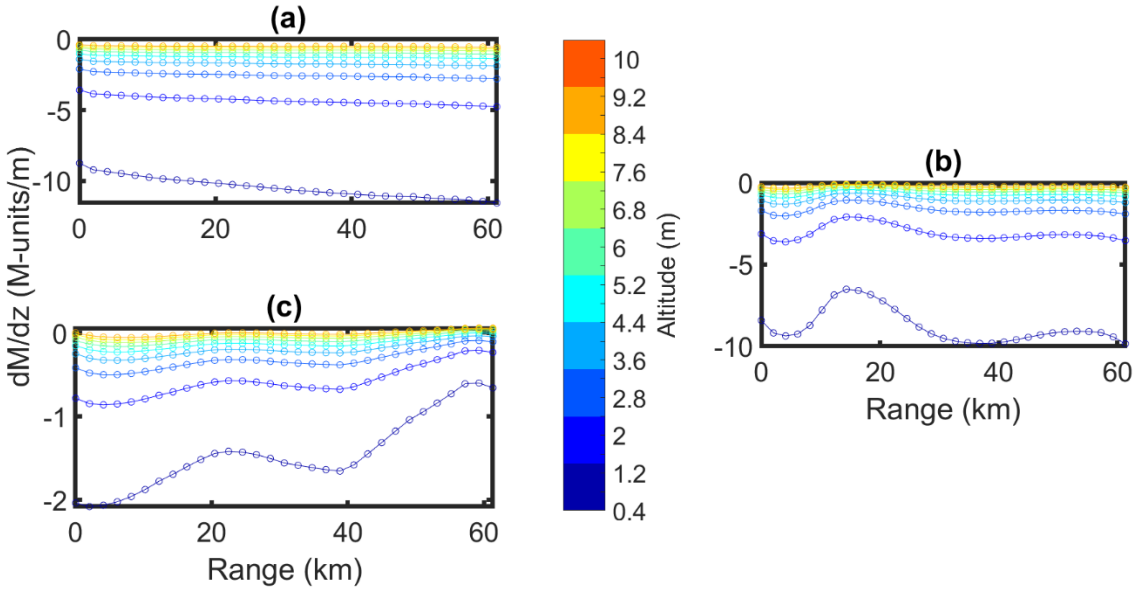

Figure 25. Examples of different categories of variations of *dM/dz* with respect to range within the lowest 10 m of altitude. All data are from COAMPS®-NAVSLaM blended forecasts. (a) Exemplifies a linear environment using a forecast for October 24, 2015 using model run 12:00Z forecast hour 7. (b) Exemplifies an oscillatory environment using a forecast for October 15, 2015 using model run 12:00Z forecast hour 10. (c) Shows an environment with both linear and sinusoidal variations from a forecast for October 30, 2015 using model run 00:00Z forecast hour 1.

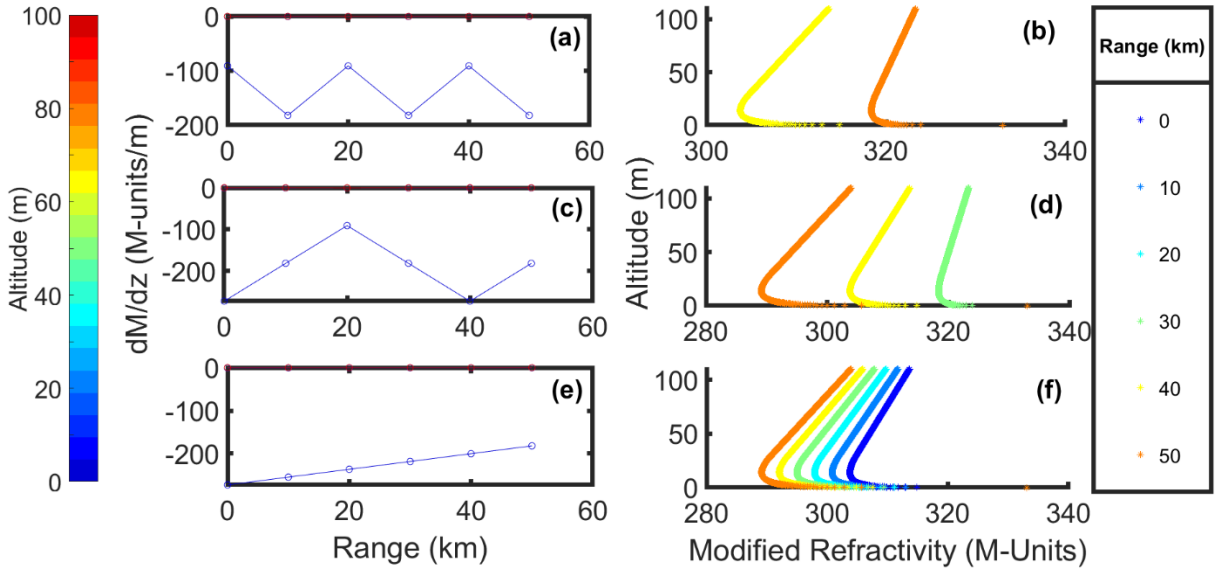

Figure 26. *dM/dz* profiles with respect to range (left; a, c, and e) and the corresponding modified refractivity profiles over range (see legend) (right; b, d, and f).

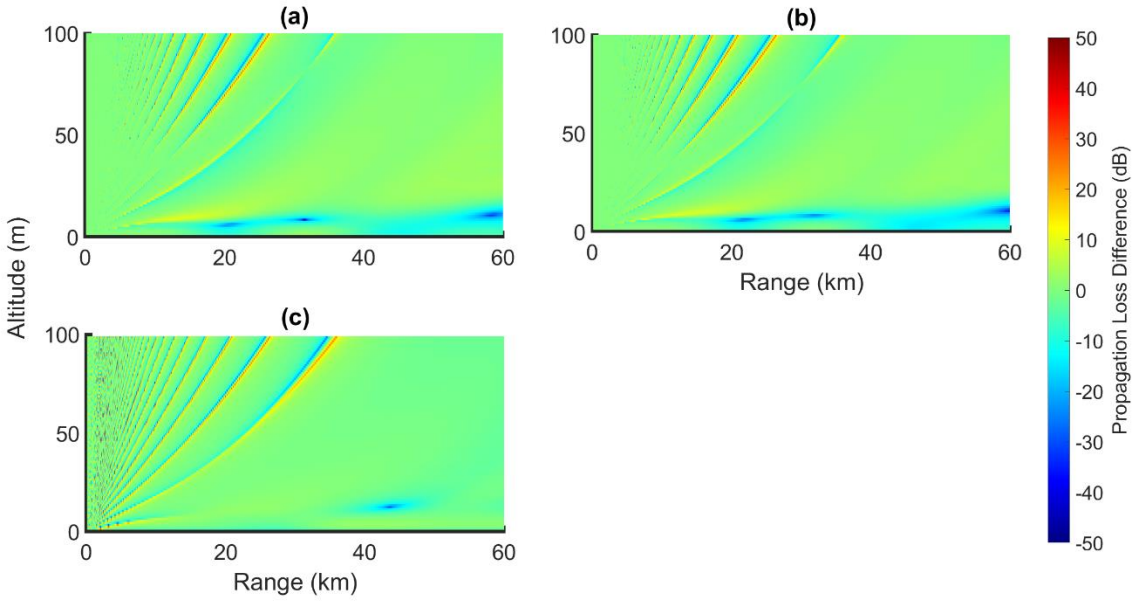

Figure 27. Differences between propagation loss produced using environments shown in Figure 26a and 26b for (a), Figure 26c and 26d for (b) and Figure 26e and Figure 26f for (c), and those propagation loss patterns produced by using the corresponding modified refractivity profile at the first range (range = 0 km) and assuming horizontal homogeneity.

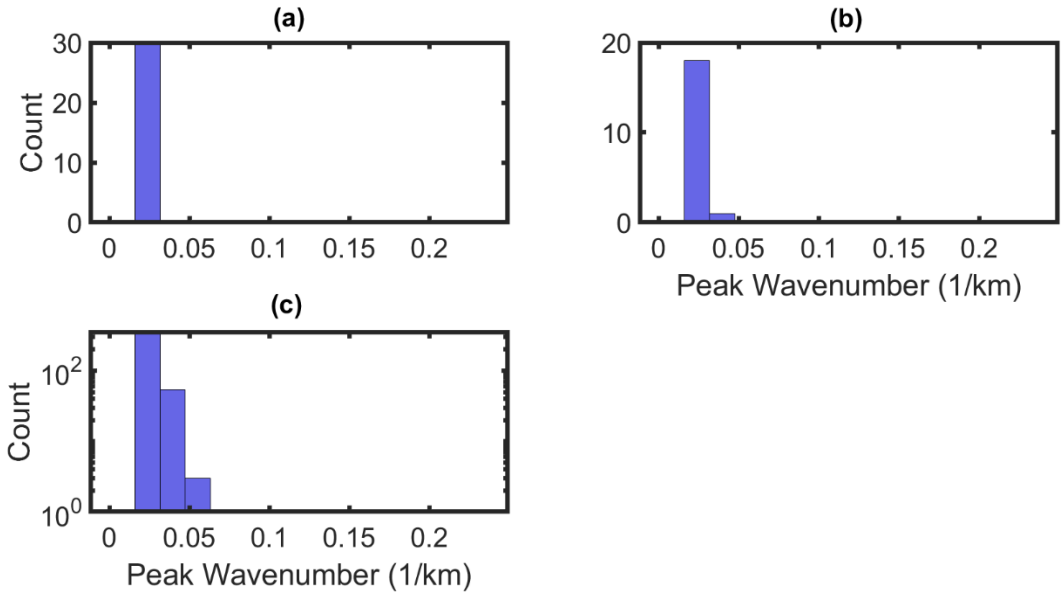

Figure 28. Histograms of peak wavenumbers of spectra of surface level *dM/dz* profiles in range classified by stability. (a) shows peak wavenumbers in free convective environments, (b) shows peak wavenumbers in stable environments, and (c) shows peak wavenumbers in unstable environments. It should be noted that a majority of the environments investigated in this study are unstable environments.

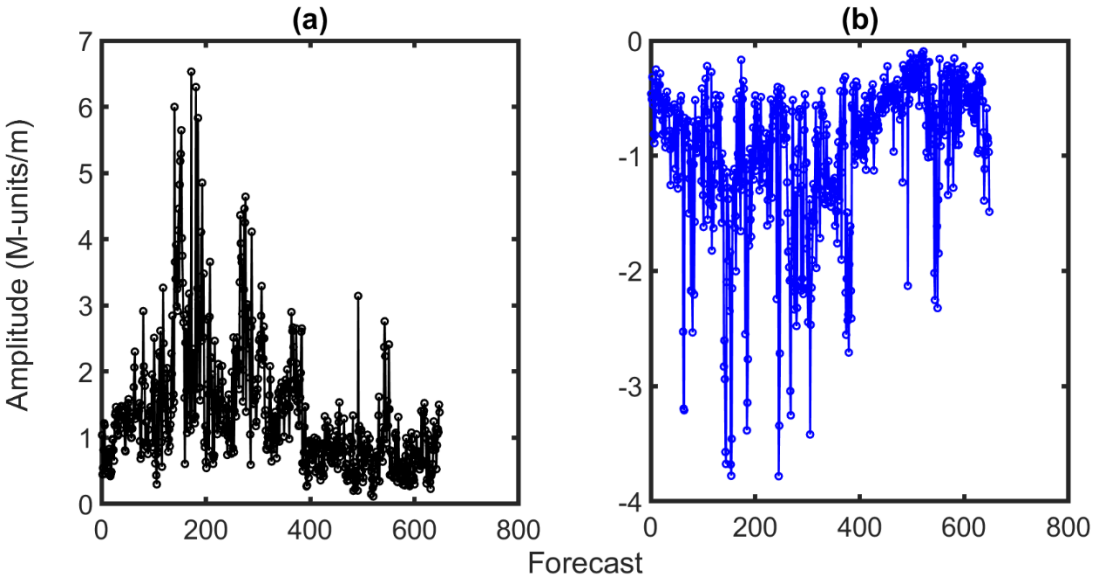

Figure 29. Estimation of the amplitude of sinusoidal range variations of *dM/dz* for each COAMPS®-NAVSLaM blended profile taken during the CASPER-East field experiment. (a) shows the maximum difference between refractive gradients and the mean refractive gradient over all ranges and altitudes while (b) shows the minimum difference.

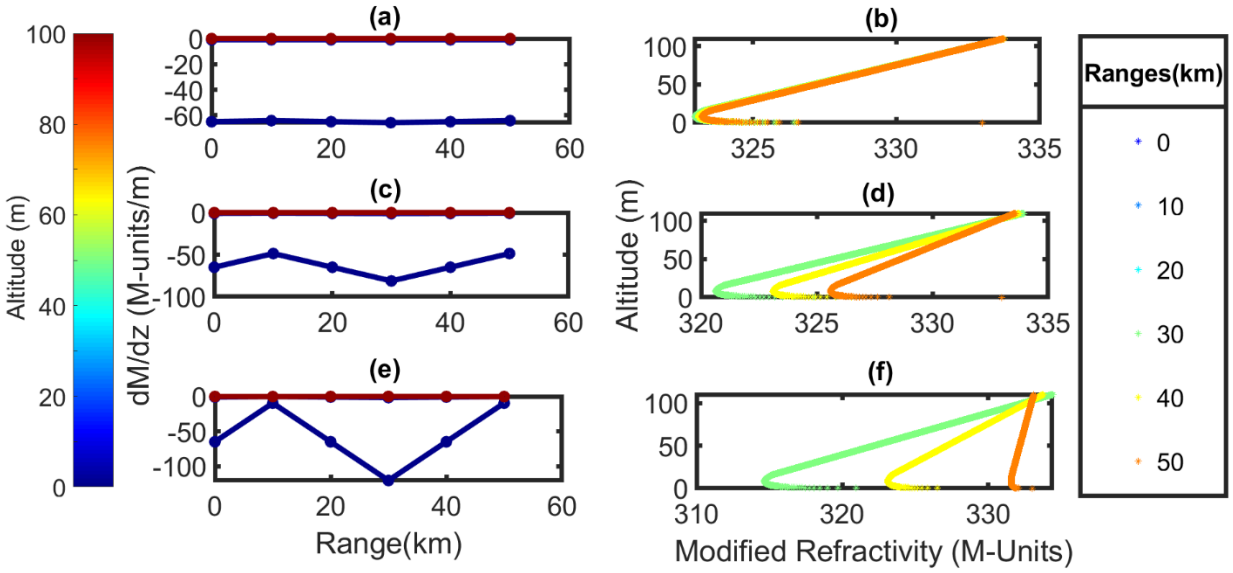

Figure 30. *dM/dz* profiles with respect to range (left) and the modified refractivity profiles created by the respective refractive gradients (right). (a, c, e) Show refractive gradients where amplitudes of sinusoidal refractive gradients with respect to range are (a) 1.23%, (b) 23.5%, or (c) 85.6% larger or smaller than the mean refractive gradient over range at each altitude while (b, d, f) shows the corresponding modified refractivity profile generated by those changes in refractive gradients shown in (a, c, e) respectively. The colorbar on the left goes with panels (a), (c), and (e), and the legend on the right goes with panels (b), (d), and (f).

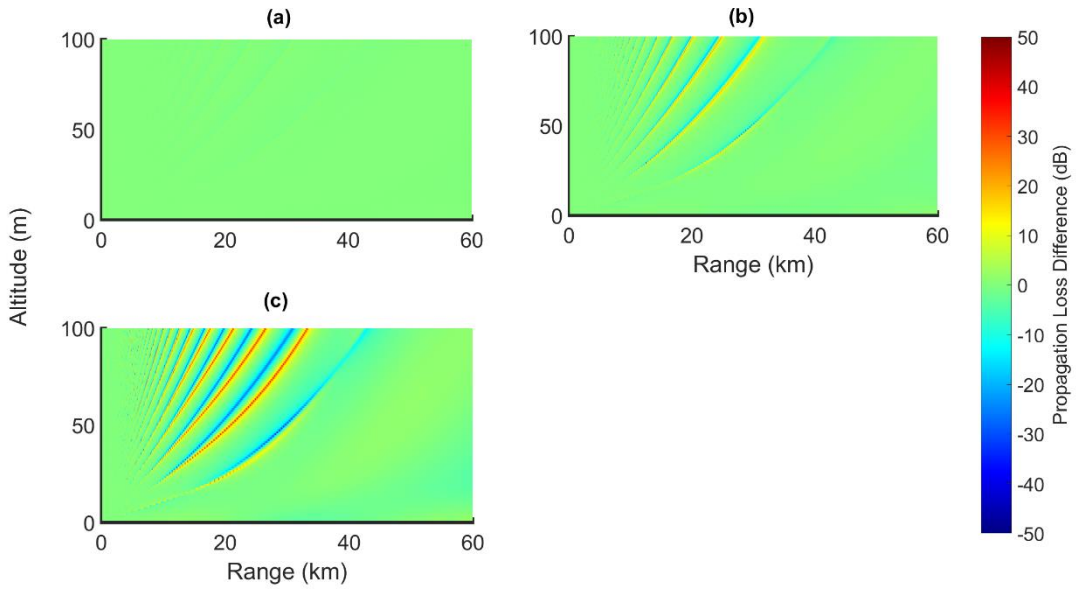

Figure 31. Differences between propagation loss produced using environments shown in Figure 30a and 30b for (a), Figure 30c and 30d for (b) and Figure 30e and Figure 30f for (c), and those propagation loss patterns produced by using the modified refractivity profile at the first range (range = 0 km) and assuming horizontal homogeneity.

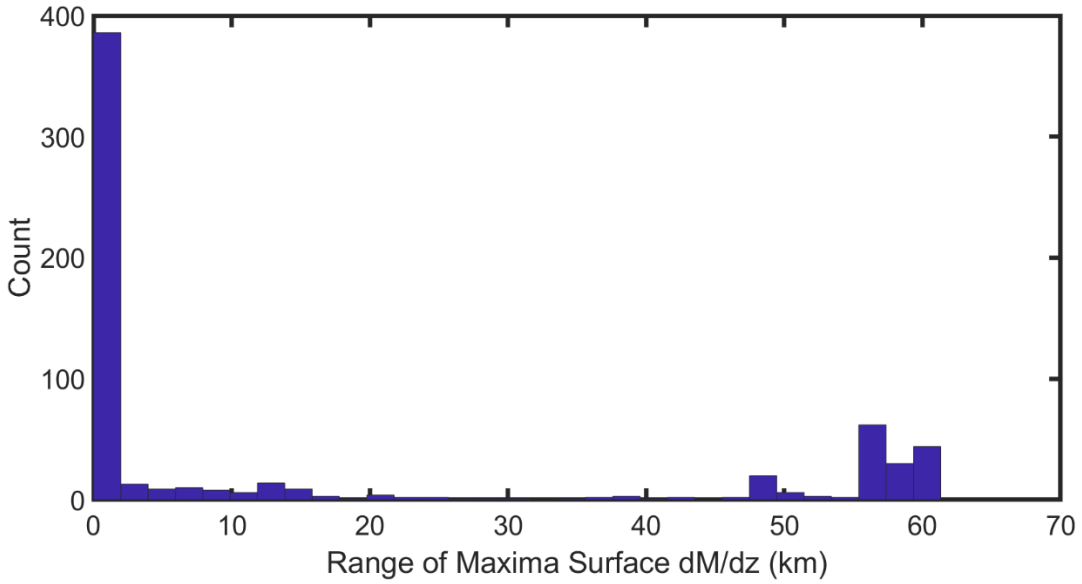

Figure 32. Histogram of the range at which the (maximum) amplitude of *dM/dz* in range occurs for all COAMPS®-NAVSLaM blended profiles.

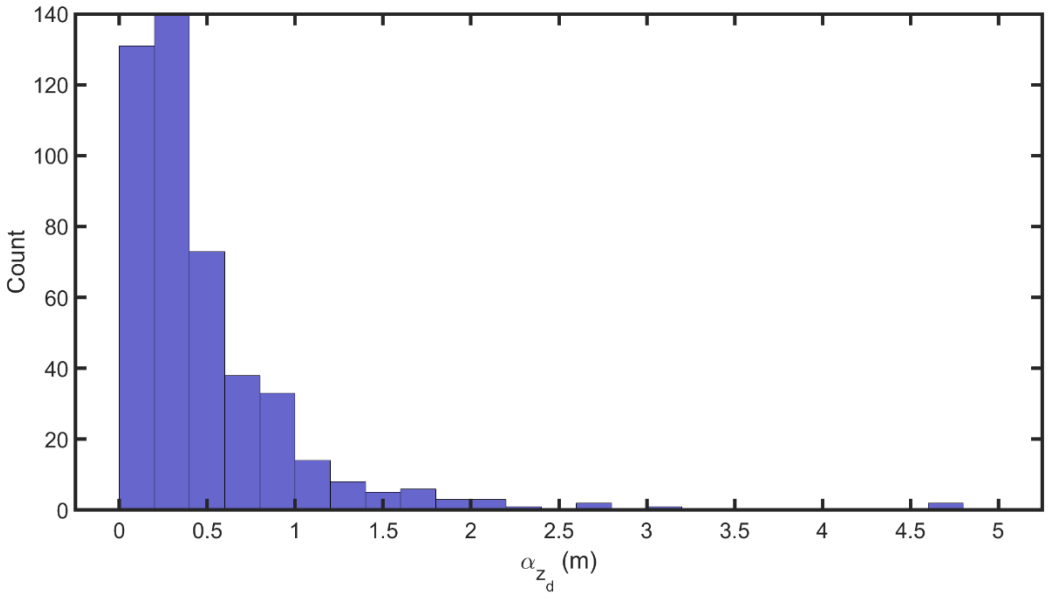

Figure 33. Histogram of the root-mean-square-error between duct height in range estimated using a linear model (Equation 18), and duct height in range for COAMPS®-NAVSLaM blended profiles.

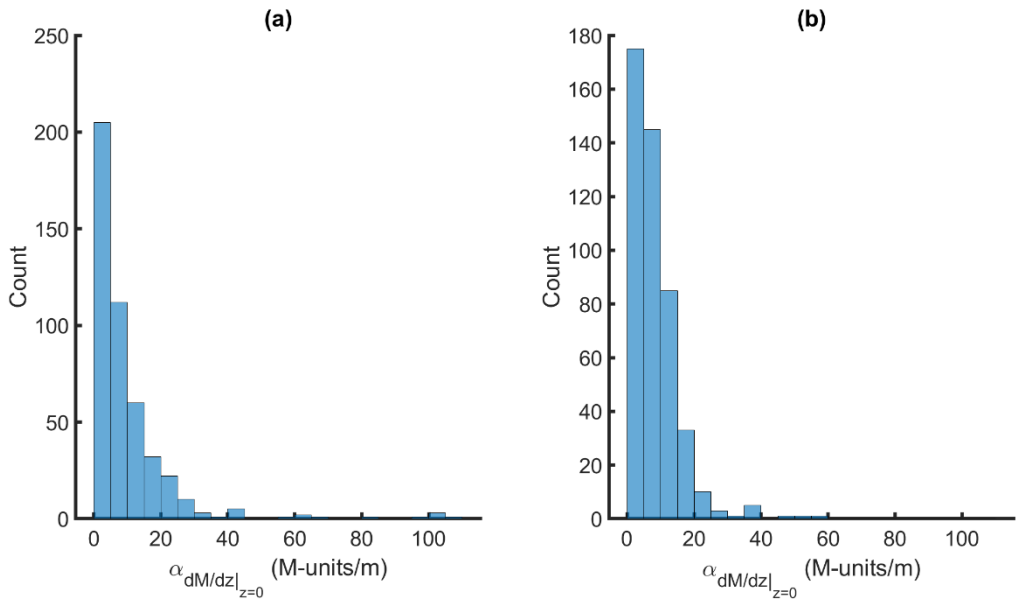

Figure 34. Histograms of the root-mean-squared-errors between the surface refractivity gradients and the non-linear regression fits to those surface refractivity gradients. (a) shows the root-mean-squared errors calculated using non-linear regression fits to Equation 21 and (b) shows the root-mean-squared errors calculated using non-linear regression fits to Equation 19 for the z=0 layer.

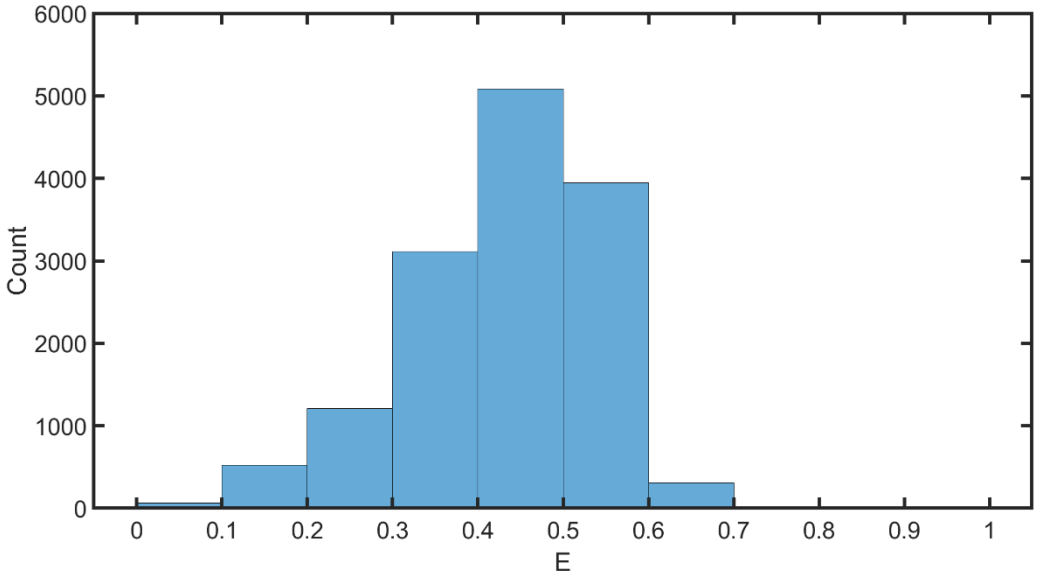

Figure 35. Histogram of percent error, *E* (Equation 12) of refractivity gradients estimated over range by the HRGM layer $0<z<z_d$ (Equation 19) and COAMPS®-NAVSLaM blended data.

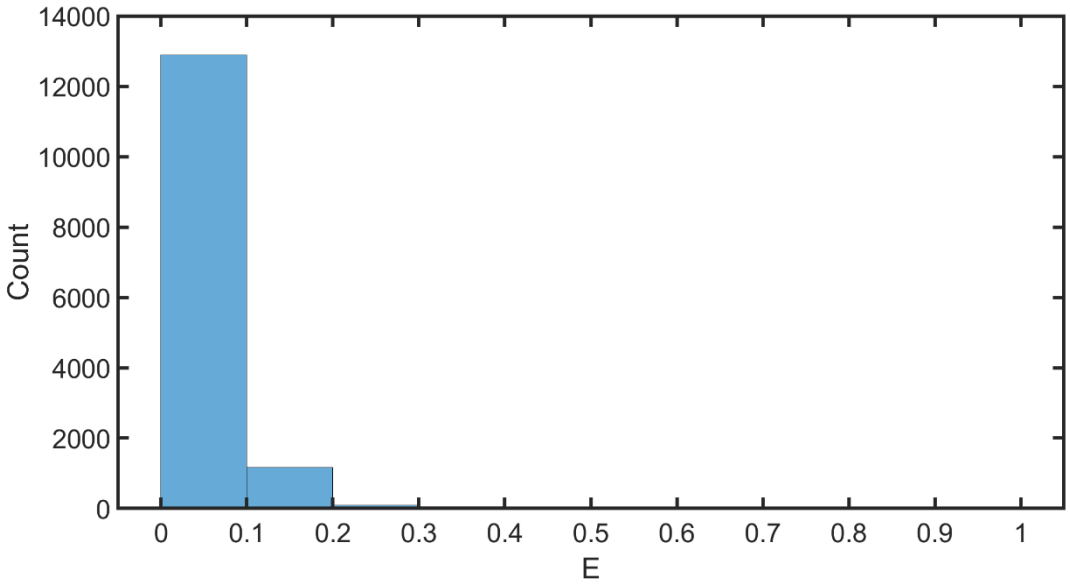

Figure 36. Histogram of percent error, *E* (Equation 12) of refractivity gradients estimated over range by the HRGM layer $z>z_d$ (Equation 19) and COAMPS®-NAVSLaM blended data.

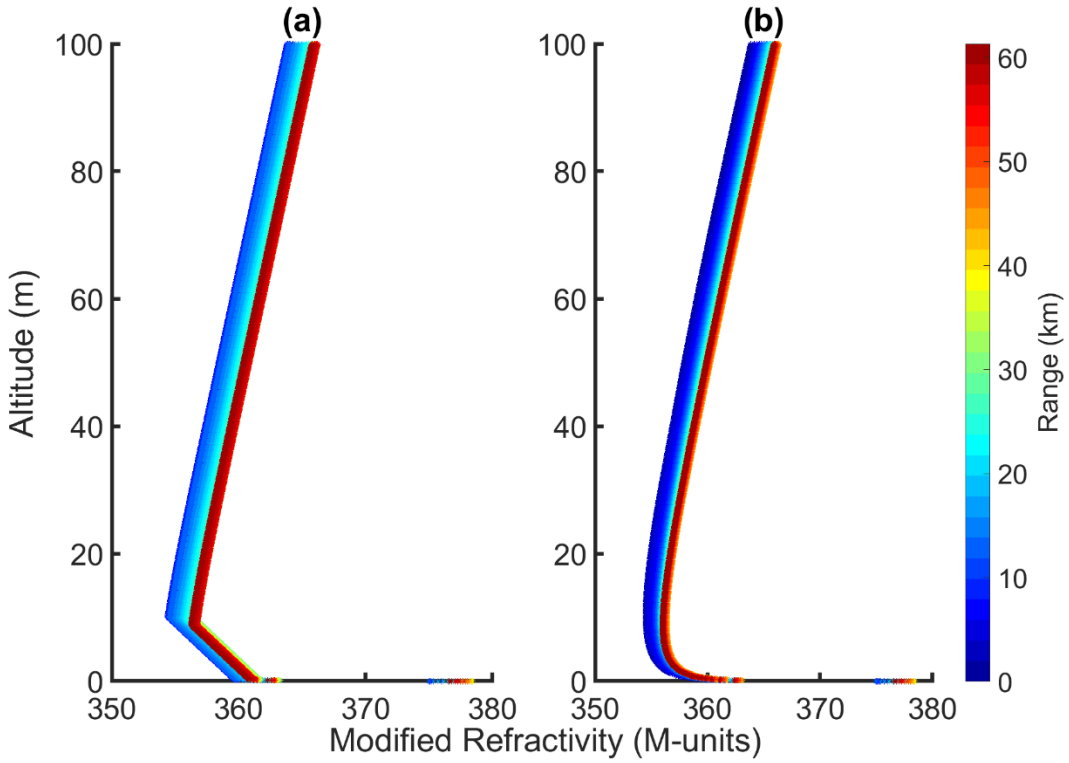

Figure 37. Range-dependent *M* profiles produced by the HRGM (a) and the COAMPS-NAVSLaM blended data (b) for October 10, 2015 at 1100Z.

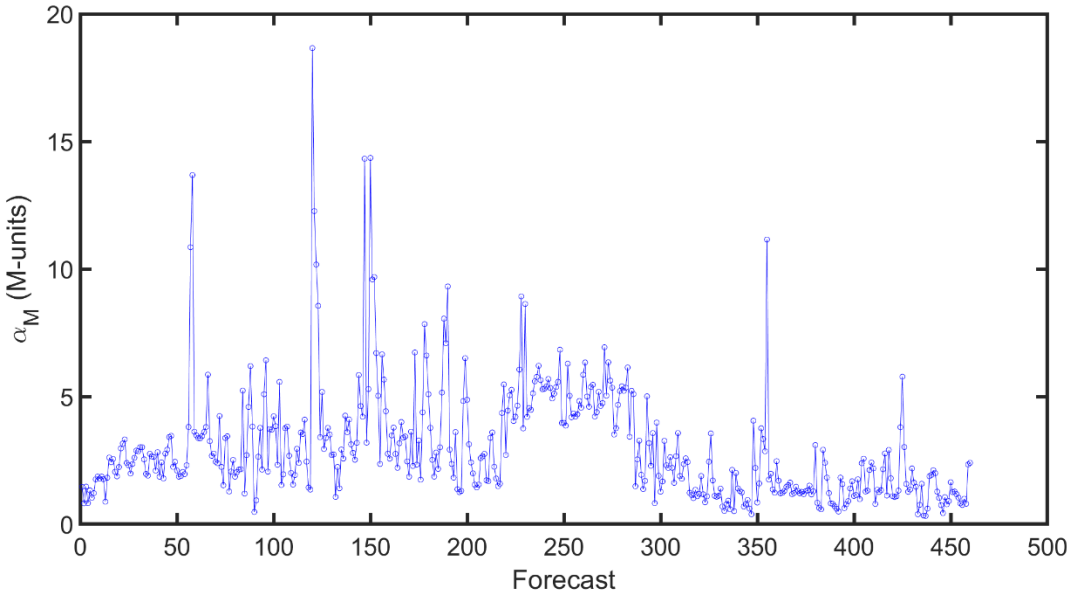

Figure 38. RMSEs between modified refractivity generated via integral form of the HRGM (Equation 20) and that of the COAMPS®-NAVSLaM blended data.

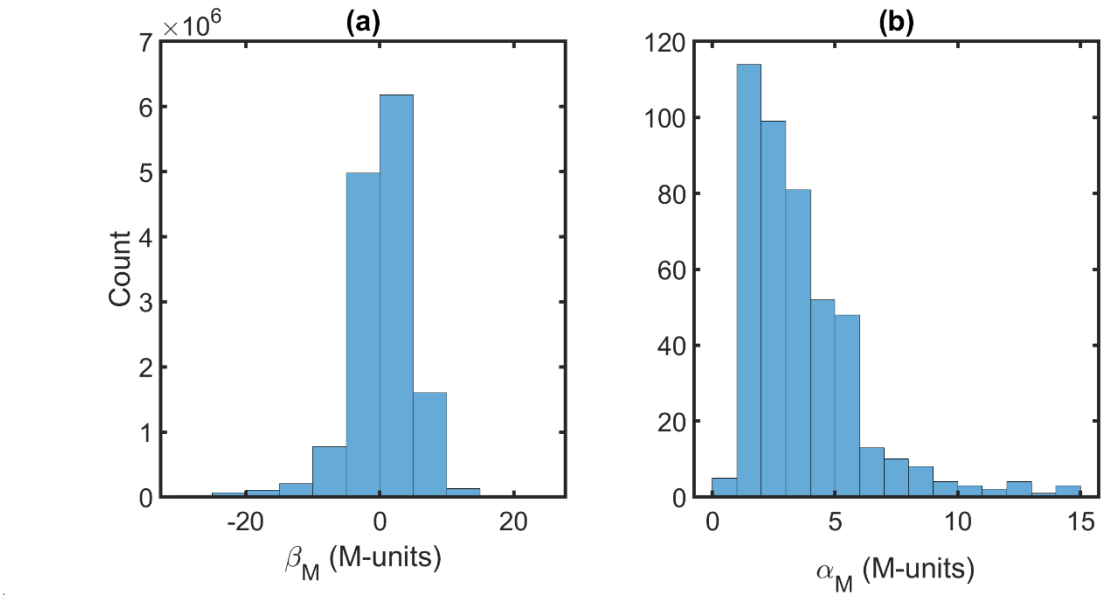

Figure 39. Histograms of residuals (a) and RMSEs (b) between modified refractivity calculated using the integral form of the HRGM (Equation 20) and COAMPS®-NAVSLaM blended data.

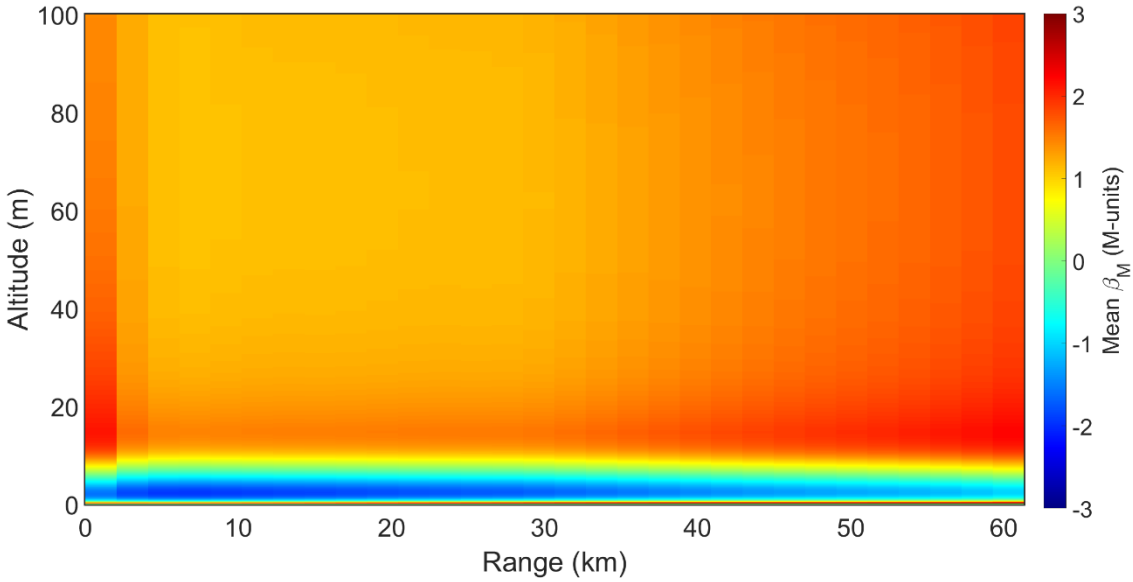

Figure 40. Forecast-averaged residuals (Equation 13) of modified refractivity between all HRGM-estimated (Equations 19 and 20) forecasts and COAMPS®-NAVSLaM blended forecasts.

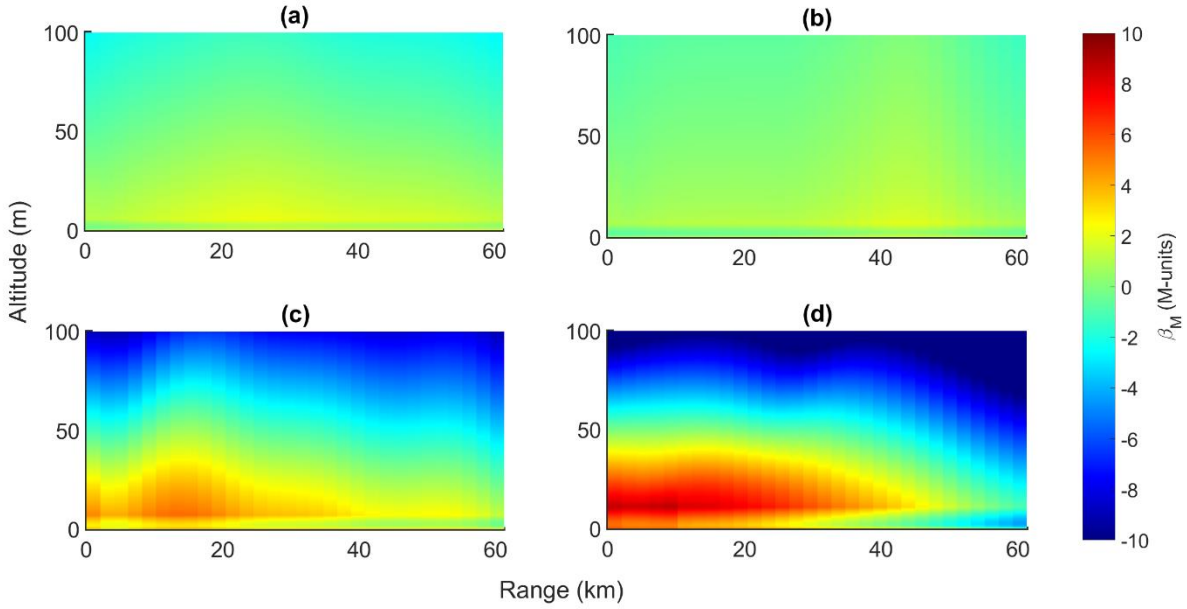

Figure 41. Examples of modified refractivity residuals between modified refractivity estimated using the HRGM and that of the COAMPS®-NAVSLaM blended data. (a) and (b) illustrate instances where modified refractivity estimations are rather good with residuals <3 M-units in the entire domain while (c) and (d) illustrate instances with higher residuals >3 M-units in the entire domain. Residuals shown are calculated using COAMPS-NAVSLaM blended forecasts from: (a) November 3rd model run 00:00Z at forecast hour 3, (b) November 3rd model run 00:00Z at forecast hour 9, (c) October 25th model run 12:00Z at forecast hour 6, and (d) October 25th model run 12:00Z at forecast hour 10.

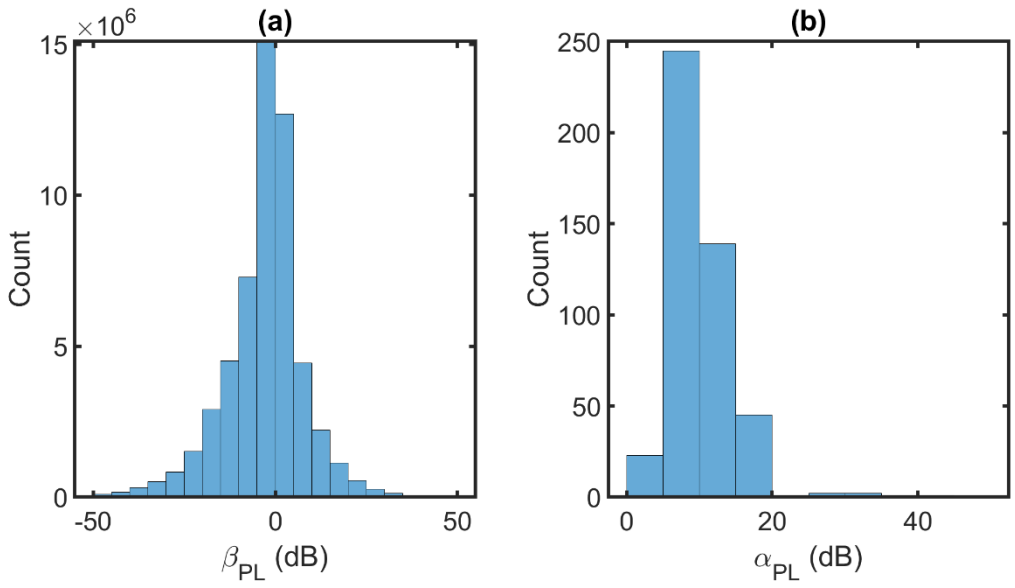

Figure 42. Histograms of residuals (a) and RMSEs (b) between propagation loss using the integral form of the HRGM (Equation 20) and that using the COAMPS®-NAVSLaM blended data.

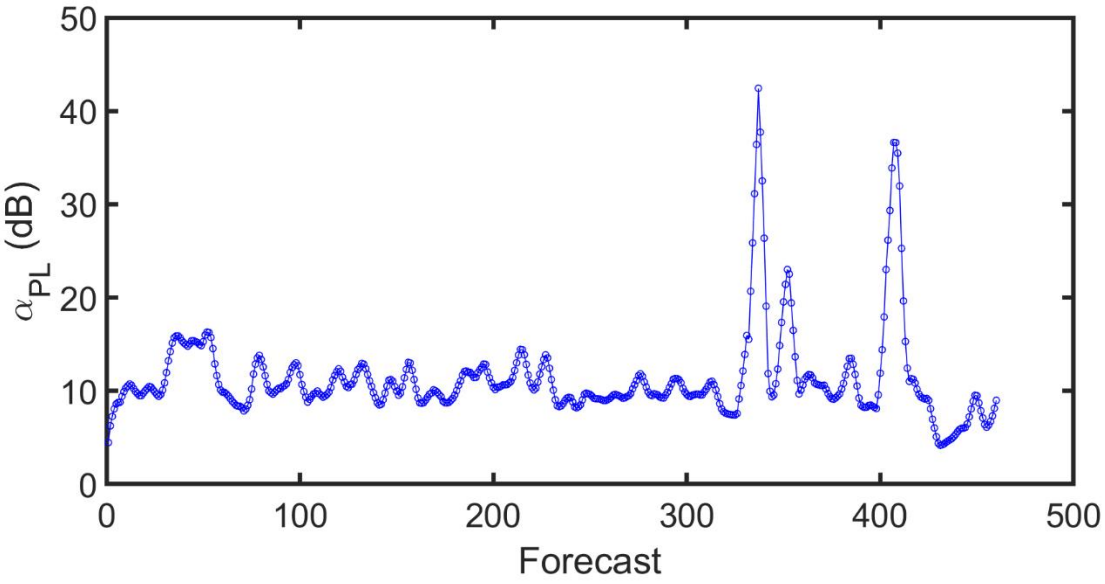

Figure 43. RMSEs between PL estimated based-on refractivity from the integral form of the HGRM and that of the COAMPS®-NAVSLaM blended data after smoothing the time series with a 5 point/forecast running average filter.

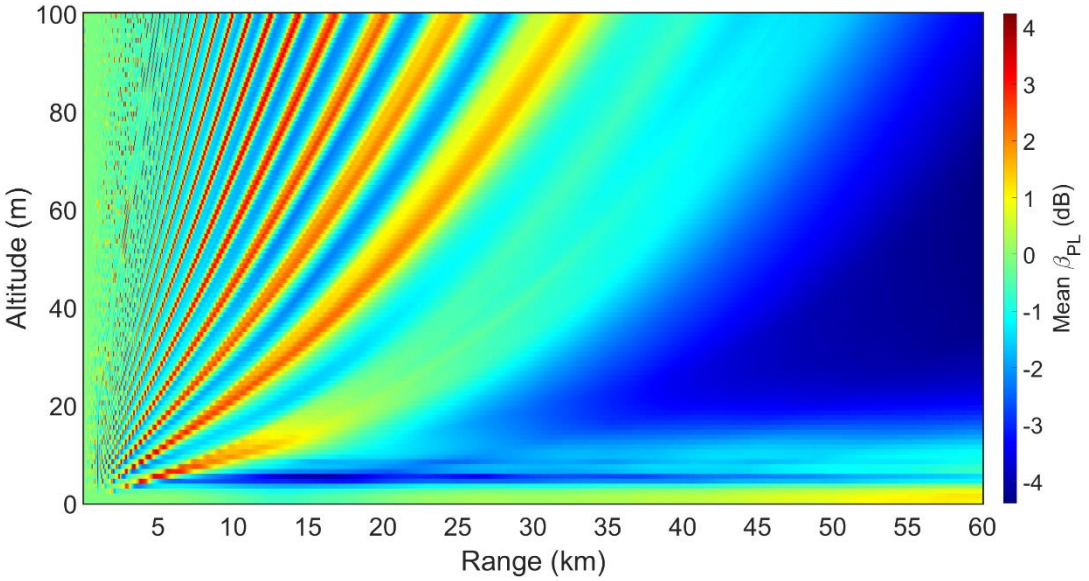

Figure 44. Forecast-averaged residuals between propagation loss based-on the integral form of HRGM (Equation 20) forecasts and that corresponding with COAMPS®-NAVSLaM blended forecasts.

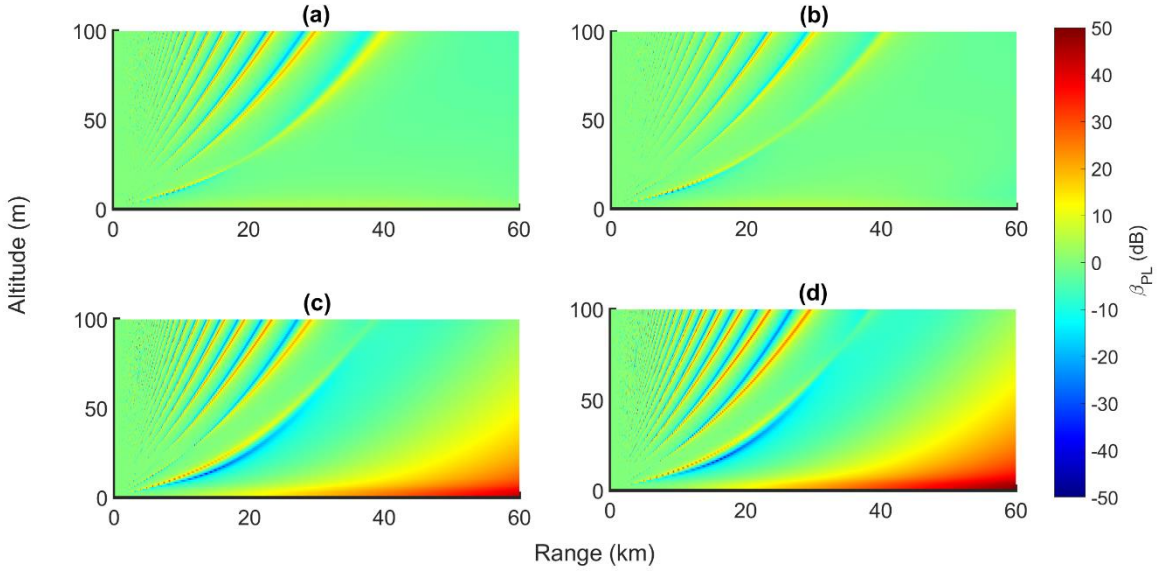

Figure 45. Examples of residuals between propagation loss estimated using the integral form of the HRGM (Equation 20) and that using COAMPS®-NAVSLaM blended data. (a) and (b) illustrate instances where PL predictions are rather good with residuals <9 dB throughout the entire domain while (c) and (d) illustrate instances with large residuals (>9 dB) throughout the entire domain. Residuals shown are calculated using PL based-on COAMPS-NAVSLaM blended forecasts from: (a) November 3rd model run 00:00Z at forecast hour 4, (b) November 3rd model run 00:00Z at forecast hour 5, (c) October 20th model run 00:00Z at forecast hour 1, and (d) October 20th model run 00:00Z at forecast hour 2.

Table 2. Correlation coefficients between RMSEs of M (α_M) throughout the entire domain and RMSEs of duct height (α_{z_d}) and refractivity gradients estimated using each function which comprises the HRGM ($\alpha_{\frac{dM}{dz}\big|_{z>z_d}}$, $\alpha_{\frac{dM}{dz}\big|_{z<z_d}}$, and $\alpha_{\frac{dM}{dz}\big|_{z=0}}$).

Model Parameter	**Correlation Coefficient with RMSE of Modified Refractivity**	**Significance (P-Value)**
$\alpha_{\frac{dM}{dz}\big\|_{z>z_d}}$	-0.12	0.01
α_{z_d}	0.15	0.00
$\alpha_{\frac{dM}{dz}\big\|_{z<z_d}}$	-0.16	0.00
$\alpha_{\frac{dM}{dz}\big\|_{z=0}}$	0.71	0.00

Table 3. Correlation coefficients between RMSEs of PL (α_{PL}**)** throughout the entire domain and RMSEs of duct height (α_{z_d}), RMSEs of refractivity gradients estimated using each function which comprises the HRGM ($\alpha_{\frac{dM}{dz}|_{z>z_d}}$, $\alpha_{\frac{dM}{dz}|_{z<z_d}}$, and $\alpha_{\frac{dM}{dz}|_{z=0}}$), or the RMSE of modified refractivity (α_M)**.**

Model Parameter	**Correlation Coefficient with RMSE of Propagation Loss**	**Significance (P-Value)**
$\alpha_{\frac{dM}{dz}\|_{z>z_d}}$	0.10	0.03
α_{z_d}	0.41	0.00
$\alpha_{\frac{dM}{dz}\|_{z<z_d}}$	0.00	0.87
$\alpha_{\frac{dM}{dz}\|_{z=0}}$	0.01	0.85
α_M	0.04	0.38

Table 4. Correlation coefficients between RMSEs of PL (α_{PL}**)** in the long range (>45 km) and RMSEs of duct height (α_{z_d}), RMSEs of refractivity gradients estimated using each function which comprises the HRGM ($\alpha_{\frac{dM}{dz}|_{z>z_d}}$, $\alpha_{\frac{dM}{dz}|_{z<z_d}}$, and $\alpha_{\frac{dM}{dz}|_{z=0}}$), or the RMSE of modified refractivity (α_M)**.**

Model Parameter	**Correlation Coefficient with RMSE of Propagation Loss in Long Ranges (>45 km)**	**Significance (P-value)**
$\alpha_{\frac{dM}{dz}\|_{z>z_d}}$	0.47	0.00
α_{z_d}	0.14	0.00
$\alpha_{\frac{dM}{dz}\|_{z<z_d}}$	0.33	0.00
$\alpha_{\frac{dM}{dz}\|_{z=0}}$	-0.07	0.13
α_M	-0.02	0.59

6.0 Summary and Conclusions

Radar is commonly used in remote sensing applications through its use of EM waves to detect a variety of targets over a wide range of distances. A radar system's performance is affected by the environment of its operation and many radars operate in the MABL, which is the environment of focus for this study. Refraction can cause EM waves to change their direction of propagation resulting in uncertainties in radar measurements. In severe cases of refraction, known as ducting, the EM waves' propagation path is bent towards the surface and can cause holes in radar detection at high altitudes and/or extension of detection ranges at low altitudes. Thus, methods to predict the occurrences of these environments are important to improving technologies such as radar. Inversion methods are one way of predicting such environments whereby the environment is reverse engineered from the radar measurement itself, but they rely on parametric models to describe the refractive environment. Typically, these parametric models only account for a single refractivity profile, which is assumed to be homogeneous in range. Although the homogeneous assumption has merit, prior research has also shown that horizontal variations in atmospheric conditions can cause significant effects on radar wave propagation (Bean and Cahoon, 1959; Goldhirsh and Dockery, 1998; Brooks et al., 1999). Thus, there is a need to develop a parametric range-dependent model for potential use in inversion methods aimed at recovering modified refractivity in horizontally heterogeneous environments.

In this study, a parametric model is developed, referred to as the HRGM, by analyzing blended data from a numerical weather prediction model (COAMPS®; Hodur, 1997) and a semi-empirical bulk estimation model (NAVSLaM; Frederickson, 2016) to evaluate heterogeneous refractivity environments during evaporative ducting conditions. The accuracy of environments created using the blended data are scrutinized by comparing modified refractivity estimates of other semi-empirical bulk estimation models (COARE 3.0; Fairall et al., 1996; Fairall et al., 2003) and measured environmental data from the CASPER-East field experiment (Wang et al., 2018). These comparisons reveal that a majority of cases (>80%) show similar modified refractivity variations with height; thus, verifying the use of COAMPS®-NAVSLaM blended estimates to analyze refractive characteristics in range for this study. Further comparisons between estimation methods are outlined in Pastore et al. (2020).

A scale characterization study on evaporation ducts estimated via COAMPS®-NAVSLaM blended data is conducted on variations of modified refractivity, duct height, and refractive gradients with respect to range. Typical distributions of modified refractivity, duct height, and refractivity gradients over range and their relation to atmospheric stability via gradient Richardson number are investigated. A radar wave propagation simulation (VTRPE; Ryan, 1991) is used to determine which range-varying variables and their resulting distributions have the greatest impact on propagation.

Modified refractivity variations in range throughout the study period are typically characterized as oscillatory and suggest that the peak wavenumbers of the sinusoidal variations are related to atmospheric stability. It is shown, however, that shifting values of surface modified refractivity by different constants over range relative to an assumed

homogeneous environment changes propagation loss by less than 1 dB, indicating minimal effects on propagation are caused by shifting modified refractivity profiles over range. Thus, the parametric model developed for this study foregoes directly modeling refractivity in favor of parametrically describing refractivity via relationships of duct heights with respect to range and refractive gradients with respect to range and height.

A majority (77%) of duct height variations in range are found to be linear, and variations illustrate a dependence on atmospheric stability. The mean standard deviation of duct height over range for all examined forecasts is 0.94 m and 20% of the forecasts show a standard deviation greater than 1 m. On the contrary to surface values of modified refractivity, duct heights which vary by amounts as small as 1 m over 60 km are shown to have non-negligible effects on propagation. This fact suggests that most environments from this blended data set present an effect on propagation, which is caused by the variance of duct height over range. Furthermore, linearly distributed duct heights with respect to range typically exhibit stronger effects on propagation than other observed distribution types such as oscillatory or step-like variations.

Refractive gradients with respect to range are found to follow sinusoidal distributions with the phase of the sinusoidal distribution differing depending on the forecast but is relatively similar with height for the same forecast. Sinusoidal variations typically are dominated by three peak wavenumbers in unstable conditions: 0.0158 km^{-1}, 0.0316 km^{-1}, and 0.0474 km^{-1}, indicating that longer length scales cause the most variation of refractivity gradients in range. Similar to variations of modified refractivity, peak wavenumbers of the sinusoidal variations of refractivity gradients suggest a dependence on atmospheric stability. Also, refractive gradients which are sinusoidal over range are

shown to result in larger variations in propagation over larger areas than linear variations. Sinusoidal amplitudes of refractivity gradients in range have non-negligible effects on propagation and refractive gradients with respect to height all show similar trends above the surface.

The results found from these characterization studies are used to create a heterogeneous parametric refractivity gradient model (HRGM), which consists of a one-way coupled set of equations (Equations 18 and 19). Using distributions which were shown to cause greater impact on propagation, a linear function is used to estimate the duct height with respect to range (Equation 18), a sinusoidal refractivity gradient function is used to describe surface refractive gradients with respect to range (Equation 19, z=0 layer), and separate exponential decay functions, which describe amplitude decay of refractivity gradient variations with respect to height above (Equation 19, $z>z_d$ layer) and below the duct height (Equation 19, $0<z<z_d$ layer) are used to model their respective altitude layers. These functions which comprise the HRGM allow an estimation of a refractive gradient environment that varies in both height and range.

The HRGM contains 11 parameters which can be solved in a radar inversion problem. The 11 parameters are as follows: the rate of duct height change in range (ξ), the duct height at r = 0 km (z_{d_0}), amplitudes of sinusoidal variances of refractive gradients at the surface with respect to each predetermined wavenumber (a_1, a_2, a_3), the initial phase of the surface refractive gradient (φ), the mean surface refractivity gradient about which the surface refractive gradient oscillates ($\mu_{\frac{dM}{dZ}}$), the decay rate of refractivity gradients with respect to height below the duct height (κ_1), the refractivity gradient at a discrete interval

below the duct height ($\frac{dM}{dz}\Big|_{z = z_d - dz}$), the decay rate of refractivity gradients with respect to height above the duct height (κ_2), and the mixed layer slope (m_1). The refractivity gradients estimated with the HRGM can be integrated to obtain a set of range-dependent modified refractivity profiles in range given surface measurements of modified refractivity over range, used as a lower boundary condition.

Each layer of the HRGM is tested via RMSE between COAMPS®-NAVSLaM blended environments and the HRGM predictions for each layer. The developed linear function for duct height (Equation 18) typically illustrated an RMSE (α_{z_d}) of less than 0.5 m, which suggests a linear function could describe most of the duct heights with respect to range, even those that didn't show a linear trend. The developed sinusoidal function which described refractive gradients at the surface (Equation 19, $z = 0$ layer) showed a majority of RMSEs ($\alpha_{\frac{dM}{dz}|_{z=0}}$) between 0 and 15 M-units/m, suggesting that surface refractive gradients can be accurately modeled using a sinusoidal function such as Equation 19 for the $z = 0$ layer. The developed decay function that describes refractive gradients with respect to height below the duct height (Equation 19, $0 < z < z_d$ layer), which further assumes horizontal homogeneity of the decay rate (κ_1) and the refractivity gradient a discrete interval below the duct height ($\frac{dM}{dz}\Big|_{z = z_d - dz}$), did not accurately capture the decay in all cases. Lastly, the developed decay function for refractive gradients with respect to height above the duct height (Equation 19, $z > z_d$ layer) where m_1 and κ_2 are assumed constant in range, produced accurate representations of refractive gradients above the duct height.

The HRGM is tested for accuracy by analyzing its estimated modified refractivity as well as its associated propagation loss to modified refractivity of COAMPS®-NAVSLaM blended data and their resulting propagation loss. On average, the HRGM was able to accurately produce estimations of modified refractivity and propagation loss. For this data, RMSEs of the modified refractivity may be greater during synoptic fronts and lower during cloudy conditions. The HRGM is shown to underestimate modified refractivity beneath the duct height, and overestimate it above the duct height, but often these are small biases. The leading cause of discrepancies in the modified refractivity estimation is the sinusoidal function used to describe the surface refractive gradients.

In contrast, for this data, RMSEs of PL produced using the HRGM may become greater in cloudy environments and decrease during synoptic front events. Discrepancies in PL typically occur in the multipath nulls and above typical duct heights in the long range region, but often the latter are relatively small discrepancies. Foremost, the leading cause of error in the propagation estimation by the HRGM in the entire domain is the model's prediction of duct heights with respect to range, while the leading cause of error at long ranges is estimation of refractivity gradients above the surface. Thus, in order to accurately predict propagation in horizontally heterogeneous environments most accurately throughout the entire domain, the behavior of the duct height over range needs to be modeled accurately and should be of the foremost concern of future heterogeneous parametric models used to solve inversion problems.

Although, on average, the HRGM seems to accurately estimate modified refractivity and PL, there are still quite a few limitations to this model that could be addressed with future research. First and foremost, propagation loss discrepancies seem to

rely on the behavior of duct height with respect to range. Currently, the HRGM assumes only linear distributions, future work should consider more complex functions for estimating duct height variations in range. Another limitation of the HRGM is that it requires surface estimates of modified refractivity over range, which is currently a difficult measurement to make *in-situ* as it would require running a transect of SST measurements over the range of the radar. However, it is possible that a single surface measurement of modified refractivity could be used, and thus, future research could investigate whether using a single measurement of surface modified refractivity could suffice. On the same note, future research could also investigate novel ways to estimate surface refractivity over extended ranges. Another large limitation of this study is that the HRGM has only been examined for one location, off the coast of Duck, NC. To further verify the model, multiple locations should be examined to determine if the variations illustrated by the COAMPS®-NAVSLaM blended data used for this study are broadly applicable. Also, although this study investigates typical variations of refractivity parameters in range, a more thorough sensitivity analysis of the propagation to refractivity parameters could be done on variations of several refractivity parameters over range using a global sensitivity method like that performed in Lentini and Hackett (2015). Lastly, M profiles produced by the HRGM have a "kink" like feature in the profiles at $z \sim z_d$, which may impact PL predictions. Further research should consider applying a smoothing function to the M profile before using it to estimate PL to determine if the PL discrepancies observed in this study are reduced.

Although containing a few shortcomings, this study provides a novel parametric refractivity model which can be used to solve radar inversion problems in horizontally

heterogeneous refractive environments commonly seen in coastal zones, at air mass boundaries associated with synoptic fronts, areas effected by clouds, thunderstorm anvil shadows, or heavy rainfall. Future radar inversion studies should consider using the HRGM to parameterize such refractive environments where heterogeneity is likely to occur.

7.0 Works Cited

Ahijevych, D. (2020). Image Archive of Satellite, Radar, Surface, and Upper-air Model Output. *Mesoscale and Microscale Meteorology Division of NCAR*. https://www2.mmm.ucar.edu/imagearchive/.

Anderson, K.D. (1989). Radar Measurements at 16.5 GHz in the Oceanic Evaporation Duct. *IEEE Trans. Antennas Propag.* 37(1). 100-106.

Atkinson, B.W., and Li, J.G. (2000). Numerical Modeling of the Propagation Environment in the Boundary Layer over the Persian Gulf. *Journal of Applied Meteorology*. 40. 586-603. doi: 10.1017/S1350482705001970.

Babin S.M. (1996). Surface Duct Height Distributions for Wallops Island, Virginia, 1984 – 1994. *Journal of Applied Meteorology*. 36. 193-204. doi: 10.1175/1520-0450(1996)035<0086:SDHDFW>2.0.CO;2.

Babin, S.M., Young, G.S., and Carton, J.A. (1997). A New Model of the Oceanic Evaporation Duct. *Journal of Applied Meteorology*. 36. 193–204. doi: 10.1175/1520-0450.

Bean, B.B., and Dutton, E.J. (1968). *Radio Meteorology*. Mineola, N.Y: Dover Publications.

Bean, B.R., and Cahoon B.A. (1959). Effect of Atmospheric Horizontal Inhomogeneity Upon Ray Tracing. *Journal of Research of the National Bureau of Standards: D. Radio Propagation.* 63D. 3.

Brooks I.M. (2001). Air-Sea Interaction and Spatial Variability of the Surface Evaporation Duct in a Coastal Environment. *Geophysical Research Letters*. 28(10). 2009-2012. doi: https://doi.org/10.1029/2000GL012751.

Brooks, I.M., Goroch A.K., and Rogers, D.P. (1999). Observations of Strong Surface Radar Ducts over the Persian Gulf. *Journal of Applied Meteorology*. 35. 86-93. doi: https://doi.org/10.1175/1520-0450(1999)038<1293:OOSSRD>2.0.CO;2.

Buck, A. L. (1981). New Equations for Computing Vapor Pressure and Enhancement Factor. *Journal of Applied Meteorology*. 20(12). 1527-1532.

Craig, K.H., and Levy, M. F. (1991). Parabolic Equation Modelling of the Effects of Multipath and Ducting on Radar Systems. In *IEEE Proceedings F (Radar and Signal Processing).* 138(2). 153-162.

Doggett, M. K. (1997). An Atmospheric Sensitivity and Validation Study of the Variable Terrain Radio Parabolic Equation Model (VTRPE). AIR FORCE INST. OF TECH. WRIGHT-PATTERSON AFB OH.

Fairall, C.W., Bradley, E.F, Rogers, D.P., Edson, J.B., and Young, G.S. (1996). Bulk Parameterization of Air-sea Fluxes for Tropical Ocean-Global Atmosphere Coupled-Ocean Atmosphere Response Experiment. *Journal of Geophysical Research: Oceans*. 101.C2. 3747-3764. doi:https://doi.org/10.1029/95JC03205.

Fairall, C.W., Bradley, E.F., Hare, J.E., Grachev, A.A., and Edson, J.B. (2003). Bulk Parameterization of Air-sea Fluxes: Updates and Verification for the COARE algorithm. *J. Clim.* 16 (4). 571-591. doi: https://doi.org/10.1175/1520-0442(2003)016<0571:BPOASF>2.0.CO;2.

Frederickson, P. (2016). Navy Atmospheric Measurements for EM Propagation Modeling. [Executive Summary]. *Naval Postgraduate School.*

Foken, T. (2006). 50 Years of the Monin-Obukhov Similarity Theory. *Boundary-Layer Meteorology*. 119-431. https://doi.org/10.1007/s10546-006-9048-6.

Garrat J.R. (1992). *The Atmospheric Boundary Layer*. New York, N.Y: Cambridge University Press.

Gerstoft, P., Gingras D.F., Rogers L.T., and Hodgkiss W.S. (2000). Estimation of Radio Refractivity Structure using Matched-Field Array Processing. *IEEE Transactions on Antennas and Propagation*. 48(3). 345-356. doi: 10.1109/8.841895.

Gerstoft, P., Rogers, L.T., Krolik, J.L., and Hodgkiss, W.S. (2003). Inversion for Refractivity Parameters from Radar Sea Clutter. *Radio Science.* 38. 1-22. doi: https://doi.org/10.1029/2002RS002640.

Goldhirsh J., and Dockery D. (1998). Propagation Factor Errors Due to the Assumption of Lateral Homogeneity. *Radio Science.* 33 (2). 239 – 249. doi: https://doi.org/10.1029/97RS03321.

Haack, T. Wang, C., Garrett, S., Glazer, A., Mailhot, J., and Marshall, R. (2010). Mesoscale Modeling of Boundary Layer Refractivity and Atmospheric Ducting. *Journal of applied meteorology and climatology.* 49(12). 2437-2457.

Hansen, Frank V. (1967) Spatial and Temporal Distribution of the Gradient Richardson Number in the Surface and Planetary Layers. ATMOSPHERIC SCIENCES LAB WHITE SANDS MISSILE RANGE N MEX.

Hill, R. J. (1989). Implications of Monin-Obukhov Similarity Theory for scalar quantities. *Journal of the Atmos. Sciences*. 46.14. 2236-2244. doi: https://doi.org/10.1175/1520-0469.

Hitney, H.V., and Hitney L.R. (1990). Frequency Diversity Effects of Evaporation Duct Propagation. *IEEE Trans. Antennas propag.* 38(10). 1694-1700.

Hodur, R.M. (1997). The Naval Research Laboratory's Coupled Ocean/Atmosphere Mesoscale Prediction System (COAMPS), *Monthly Weather Review.* 125. 1414-1430. doi: https://doi.org/10.1175/1520-0493(1997)125<1414:TNRLSC>2.0.CO;2.

Hogan, T., and Rosmond, T. (1991). The Description of the Navy Operational Global Atmospheric Prediction System's Spectral Forecast Model. *Monthly Weather Review.* 119. 1786-1815. doi: 10.1175/1520-0493(1001)119<1786:TDOTNO>2.0.CO;2.

Kammerer A.J., and Hackett E.E. (2017). Use of Proper Orthogonal Decomposition for Extraction of Ocean Surface Wave Fields from X-Band Radar Measurements of the Sea Surface. *Remote Sensing.* 9(9). 881. doi: https://doi.org/10.3390/rs9090881.

Kang D, Wang Q. (2016). Optimized Estimation of Surface Layer Characteristics from Profiling Measurements. *Atmosphere*. 7(2):14. doi:10.3390/atmos7020014.

Karimian, A., Yardim, C., Gerstoft, P., Hodgkiss W.S., and Barrios, A.E. (2011). Refractivity Estimation from Sea Clutter: An Invited Review. *Radio Science*. 45.06, 1-16.

Karimian, A., Yardim, C., Haack, T., Gerstoft, P., Hodgkiss, W.S., and Rogers T. (2013). Toward the Assimilation of the Atmospheric Surface Layer Using Numerical Weather Prediction and Radar Clutter Observations. *J. Appl. Meteor. Climatol.* 52. 2345-2355. https://doi.org/10.1175/JAMC-D-12-0320.1.

Kerr, D.E. (1951). Tropospheric Refraction, in *Propagation of Short Radio Waves*, edited by D.E. Kerr. New York: McGraw-Hill.

Knight, R.D. (2013). *Physics for Scientists and Engineers: A Strategic Approach.* Glenview, Illinois: Pearson.

Lentini, N.E., and Hackett, E.E. (2015). Global Sensitivity of Parabolic Equation Radar Wave Propagation Simulation to Sea State and Atmospheric Refractivity Structure. *Radio Science*. 50(10), 1027-1049. doi/10.1002/2015RS005742

Markowski, P., and Richardson, Y. (2010). *Mesoscale Meteorology in Mid-latitudes*. Chichester, West Sussex Hoboken, NJ: Wiley-Blackwell.

Matsko, I.J., and Hackett, E.E. (2019). Impact of Radar Data Sampling on the Accuracy of Atmospheric Refractivity Inversions over marine surface. *Radio Science*, 54.7, 704-714 https://doi.org/10.1029/2018RS006757.

Pastore, D.M., Greenway, D.P., Stanek M.J., Wessinger S.E., Haack, T.P., Wang, Q., and Hackett E.E. (2020). Comparison of Atmospheric Refractivity Estimation Methods and their Influence on Radar Propagation Predictions. *2020 IEEE Antennas and Propagation Society and International Union of Radio Science Symposium.* Montreal, Canada, 5-10 July.

Paulus, R.A. (1990). Evaporation Duct Effects on Sea Clutter. *IEEE Trans. Antennas and Propagation*. 38(11). 1765-1771. doi: 10.1109/8.102737.

Paulus, R.A. (1985). Practical Application of an Evaporation Duct Model. *Radio Science.* 20(4). 887-896. doi:10.1029/RS020i004p008877.

Peng, M.S., Ridout, J.A., and Hogan T.F. (2004). Recent Modifications of the Emanuel Convective Scheme in the Navy Operational Global Atmospheric Prediction System. *Monthly Weather Review.* 132. 1254-1268. doi: https://doi.org10.1175/15200493(2004)132<1254:RMOTEC>2.0.CO;2.

Penton, S.E., and Hackett. E.E. (2018). Rough Ocean Surface Effects on Evaporative Duct Atmospheric Refractivity Inversions using Genetic Algorithms. *Radio Science.* 53(6). 804-819. doi: 10.1029/2017RS006440.

Rogers, L.T., Hattan, C.P., and Stapleton, J.K. (2000). Estimating Evaporation Duct Heights from Radar Sea Echo. *Radio Science*. 35(4), 955-966. Doi:10.1029/199RS002275.

Ryan, F. J. (1991). User's Guide for the VTRPE (Variable Terrain Radio Parabolic equation) Computer Model. No. NOSC/TR-1456. NAVAL OCEAN SYSTEMS CENTER SAN DIEGO CA.

Saeger, J.T., Grimes, N.G., Rickard, H. E., and Hackett, E.E. (2015). Evaluation of Simplified Evaporation Duct Refractivity Models for Inversion Problems. *Radio Science.* 50.10. 110-1130. doi: 10.1002/2014RS005642.

Sirkova, I. (2012). Brief Review on PE Method Application to Propagation Channel Modeling in Sea Environment. *Central European Journal of Engineering.* 19-38. doi: 10.2478/s13531-011-00490-y.

Skolnik, M.I. (1990). *Radar Handbook*. New York, NY: McGraw-Hill.

Turton, J.D., Bennetts, D.A., and Farmer, S. F. G. (1988). An Introduction to Radio Ducting. *Meteorological Magazine.* 117(1393), 245-254.

Wagner, M., Gerstoft, P., and Rogers, T. (2016). Estimating Refractivity from Propagation Loss in Turbulent Media. *Radio Science*. 51. 1876-1894. doi: 10.1002/2016RS006061.

Wang, Q., Alappattu, D.P., Billingsley, S., Blomquist, B., Burkholder, R.J., Christman, A.J., Creegan, E.D., de Paolo, T., Eleuterio, D.P., Fernando, H.J., Franklin, K.B., Grachev, A.A., Haack, T., Hanley, T.R., Hocut, C.M., Holt, T.R., Horgan, K., Jonsson, H.H., Hale, R.A., Kalogiros, J.A., Khelif, D., Leo L.S., Lind, R.J., Lozovatsky, I., Planella-Morato, J., Mukherjee, S., Nuss, W.A., Pozderac, J., Rogers, L.T., Savelyev, I., Savidge, D.K., Kipp Shearman, R., Shen, L., Terrill, E. Marcela Ulate, A., Wang, Q., Wendt, R. Travis, Wiss, R., Woods, R.K., Xu, L., Yamaguchi, R.T., and Yardim, C. (2018). CASPER: Coupled Air–Sea Processes and Electromagnetic Ducting Research. *Bull. Amer. Meteor. Soc.* 99. 1449–1471. https://doi.org/10.1175/BAMS-D-16-0046.1.

Yang, S., Yank K.D., Yang Y.X., and Ma, X.L. (2015). Experimental Verification of Effect of Horizontal Inhomogeneity of Evaporation Duct on Electromagnetic Wave

Propagation. *Chinese Physics B.* 24(4). 044102. doi:10.1088/1674-1056/24/4/044102.

Yano, Jun-Ichi. (2018). Scientific Challenges of Convective-Scale Numerical Weather Prediction. *Bulletin of the American Meteorological Society*. 99.4. 669-710. doi: https://doi.org/10.1175/BAMS-D-17-0125.1.

Yardim, C., Gerstoft, P., and Hodgkiss, W.S. (2006). Estimation of Radio Refractivity from Radar Clutter using Bayesian Monte Carlo Analysis. *IEEE Trans. Antennas Propagation.* 54(4). 1318-1327. doi:10.1109/TAP.2006.872673.

Yardim, C, Gerstoft, P, and Hodgkiss W.S. (2009). Sensitivity Analysis and Performance Estimation of Refractivity from Clutter Techniques. *Radio Science*. 44.01. 1-16. https://doi.org/10.1029/2008RS003897.

Zhao, X. (2012). Evaporation Duct Height Estimation and Source Localization from Field Measurements at an Array of Radio Receivers. *IEEE Transactions on Antenna Propagation*. 60(2). 1020-1025. doi: 10.1109/TAP.2011.2173115.

Zhao, X., and Huang, S. (2014). Atmospheric Duct Estimation Using Radar Sea Clutter returns by the Adjoint Method with Regularization Technique. *J. Atmos. Oceanic Technol.* 31. 1250–1262. doi: https://doi.org/10.1175/JTECH-D-13-00025.1.

Zhao, X., and Huang, S. (2012). Estimation of Atmospheric Duct Structure Using Radar Sea Clutter. *J. Atmos. Sci.* 69. 2808–2818. doi: https://doi.org/10.1175/JAS-D-12-073.1.

Zhao, X., Huang, S., and Du, H. (2011). Theoretical Analysis and Numerical Experiments of Variational Adjoint Approach for Refractivity Estimation. *Radio Science.* 46. RS1006. doi: https://doi.org/10.1029/2010RS004417.

Zhao, X., Yardim, C., Wang, D., and Howe, B. (2017). Estimating Range-Dependent Evaporation Duct Height. *American Meteorological Society.* 34.5. 1113-1123. doi: https://doi.org/10.1175/JTECH-D-16-0125.1.